Cell

Brain perivascular macrophages regulate endothelial cell function via a cMAF-dependent transcriptional program in mouse and human

Graphical abstract

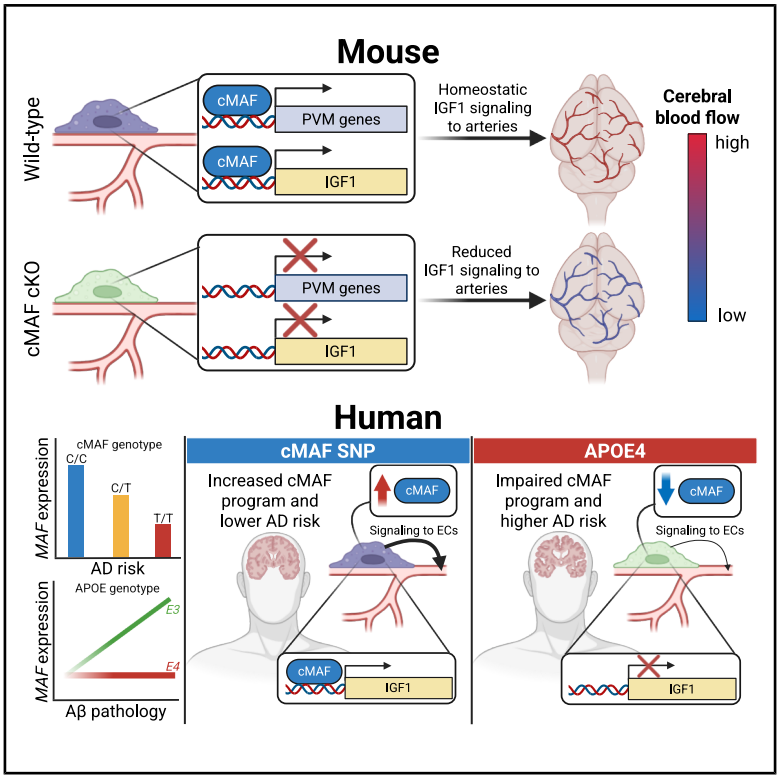

Highlights

- cMAF is essential for the specification of brain perivascular macrophages (PVMs)
- cMAF supports cerebrovascular functions through local IGF1 production
- This cMAF-dependent program is conserved in mice and humans
- A genetic variant that increases cMAF expression correlates with reduced AD risk

Authors

Simone Brioschi, Julia A. Belk, Steffen E. Storck, ..., Song Hu, Jonathan Kipnis, Marco Colonna

Correspondence

simone.brioschi@uth.tmc.edu (S.B.), mcolonna@mgh.harvard.edu (M.C.)

In brief

This study identifies cMAF as a key transcription factor that orchestrates the molecular crosstalk between brain perivascular macrophages and arteries, thereby sustaining cerebrovascular function in health and disease.

Brioschi et al., 2026, Cell *189*, 1–21
October 29, 2026
https://doi.org/10.1016/j.cell.2026.07.043

CellPress

Cell

CellPress
OPEN ACCESS

Article

Brain perivascular macrophages regulate endothelial cell function via a cMAF-dependent transcriptional program in mouse and human

Simone Brioschi,[1,2,23,*] Julia A. Belk,[3,23] Steffen E. Storck,[1,4,23] Yue Wu,[5,23] Zhuoying Wang,[5] Ziang Feng,[5] Lynn van Olst,[6,7,8] Josie L. Emery,[9] Raki Sudan,[1] Junjie Wu,[1] Siling Du,[1] Marco Genua,[10] Federica La Terza,[10] Alex J. Edwards,[6,7] Khai M. Nguyen,[1] Jessie Sanford,[11,12] Daniel D. Lee,[1] Mattia Bugatti,[13] Arnold J. Federico,[14] Yun Chen,[1] Zuoxu Wang,[1] Silvia Penati,[1] Patrick Fernandes Rodrigues,[1,15] Alina Ulezko Antonova,[1] Hui Qi Loo,[1] Igor Smirnov,[1,4] Susan Gilfillan,[1] Carmen M. Halabi,[16] Jennifer Ponce,[17] Jun Yan,[18] Howard Y. Chang,[19] Gwendalyn J. Randolph,[1] William Vermi,[13] Marina Cella,[1] Michael Meers,[14] Renato Ostuni,[10,20] David Gate,[6,7] Aivi T. Nguyen,[9] Carlos Cruchaga,[11,12] Song Hu,[5] Jonathan Kipnis,[1,4] and Marco Colonna[1,4,21,22,24,*]

[1]Department of Pathology and Immunology, Washington University School of Medicine in Saint Louis, St. Louis, MO 63110, USA
[2]Center for Neuroimmunology and Glial Biology, Institute of Molecular Medicine, University of Texas Health Science Center, Houston, TX 77030, USA
[3]Department of Pathology, Stanford University, Stanford, CA 94305, USA
[4]Brain Immunology and Glia (BIG) Center, Washington University School of Medicine in Saint Louis, St. Louis, MO 63110, USA
[5]Department of Biomedical Engineering, James McKelvey School of Engineering Washington University in St. Louis, St. Louis, MO 63130, USA
[6]Abrams Research Center on Neurogenomics, Northwestern University Feinberg School of Medicine, Chicago, IL 60611, USA
[7]The Ken & Ruth Davee Department of Neurology, Northwestern University Feinberg School of Medicine, Chicago, IL 60611, USA
[8]Department of Biomedical Sciences, University of Groningen, University Medical Center Groningen, Groningen 9700AD, the Netherlands
[9]Department of Laboratory Medicine and Pathology, Mayo Clinic, Rochester, MN 55905, USA
[10]San Raffaele Telethon Institute for Gene Therapy (SR-Tiget), IRCCS San Raffaele Scientific Institute, Milan 20132, Italy
[11]Department of Psychiatry, Washington University School of Medicine in Saint Louis, St. Louis, MO 63110, USA
[12]NeuroGenomics and Informatics Center, Washington University School of Medicine in Saint Louis, St. Louis, MO 63110, USA
[13]Department of Molecular and Translational Medicine, University of Brescia, Brescia 25123, Italy
[14]Department of Genetics, Washington University School of Medicine in Saint Louis, St. Louis, MO 63110, USA
[15]Institute of Experimental Immunology, University of Zurich, Zurich 8057, Switzerland
[16]Department of Pediatrics, Washington University School of Medicine in Saint Louis, St. Louis, MO 63110, USA
[17]McDonnell Genome Institute, Washington University School of Medicine in Saint Louis, St. Louis, MO 63110, USA
[18]Division of Immunotherapy, The Hiram C. Polk, Jr., MD Department of Surgery, Immuno-Oncology Program, Brown Cancer Center, University of Louisville School of Medicine, Louisville, KY 40202, USA
[19]Departments of Dermatology and Genetics, Stanford University, Stanford, CA 94305, USA
[20]Vita-Salute San Raffaele University, IRCCS San Raffaele Scientific Institute, Milan 20132, Italy
[21]Center for Computational and Integrative Biology, Massachusetts General Hospital, Boston, MA 02114, USA
[22]Broad Institute of MIT and Harvard, Cambridge, MA 02142, USA
[23]These authors contributed equally
[24]Lead contact
*Correspondence: simone.brioschi@uth.tmc.edu (S.B.), mcolonna@mgh.harvard.edu (M.C.)
https://doi.org/10.1016/j.cell.2026.07.043

SUMMARY

Brain perivascular macrophages maintain brain physiology, yet their transcriptional regulators and functions in health and disease remain unclear. Using single-cell multi-omics and functional experiments, we identify cellular musculoaponeurotic fibrosarcoma oncogene (cMAF) as a key transcription factor for brain perivascular macrophages, and conditional deletion of cMAF disrupts their phenotype *in vivo*. Functionally, cMAF drives insulin-like growth factor-1 (IGF1) expression in perivascular macrophages, enabling communication with endothelial cells. Consistently, cMAF deletion in perivascular macrophages causes transcriptional alterations in cerebral arteries, affecting vascular functions. Notably, cMAF emerges as the main transcription factor for human perivascular macrophages, suggesting conservation of this transcriptional module. During Alzheimer's disease (AD), human perivascular macrophages upregulate cMAF and IGF1 to enhance communication with vascular cells, and this response is abrogated in *APOE4* carriers. Lastly, we explore an uncharacterized polymorphism in cMAF, providing evidence that the cMAF program is protective against AD. Targeting cMAF in perivascular macrophages may offer new therapeutic strategies for neurodegenerative and cerebrovascular diseases.

Please cite this article in press as: Brioschi et al., Brain perivascular macrophages regulate endothelial cell function via a cMAF-dependent transcriptional program in mouse and human, Cell (2026), https://doi.org/10.1016/j.cell.2026.07.043

INTRODUCTION

Brain macrophages are implicated in maintaining CNS homeostasis and immune defense. Microglia (MG) within the CNS parenchyma support brain development, promote consolidation of neuronal circuits, and clear apoptotic cells.[1–10] The brain-border regions harbor a diverse repertoire of macrophages referred to as border-associated macrophages (BAMs) or CNS-associated macrophages (CAMs).[11,12] BAMs regulate neurovascular communications, orchestrate CNS immune responses and tissue repair during neuroinflammation,[13–16] and have been implicated in vascular damage during hypertension,[17,18] β-amyloidosis,[19] and anti-Aβ immunotherapy.[20,21]

BAMs comprise at least two transcriptionally distinct subtypes, defined by major histocompatibility complex class II (MHC class II) or CD163 expression,[22] consistently reported across multiple studies.[11,23–26] Developmentally, MHCII$^+$ BAMs largely derive from definitive hematopoiesis, whereas CD163$^+$ BAMs, like MG, mainly arise from yolk sac hematopoiesis.[22,23,27–29] Spatially, MHCII$^+$ and CD163$^+$ populations occupy distinct niches: MHCII$^+$ BAMs enrich the dura mater and choroid plexus, while CD163$^+$ BAMs predominate in the leptomeninges and perivascular spaces.[11,23,29] BAM depletion studies have shown that the CD163$^+$ BAM profile is strongly shaped by its embryonic ontogeny, as bone-marrow-derived macrophages (BMDMs) are unable to fully recapitulate this phenotype.[30–32] In contrast to MG,[22,33,34] however, the transcriptional and epigenetic programs instructing niche-specific BAM identities remain poorly understood. Comprehensive transcriptomic and epigenetic profiling of BAMs is warranted to uncover their molecular underpinnings in health and disease.[35]

Using single-cell epigenomics and transcriptomics, combined with transcription factor (TF) binding analyses, we identified cMAF (cellular musculoaponeurotic fibrosarcoma oncogene, encoded by *Maf*) as the key regulator of the CD163$^+$ macrophage phenotype. Conditional deletion of cMAF in brain macrophages induced a striking phenotypic conversion of CD163$^+$ BAMs into MHCII$^+$-like cells, which was associated with disrupted fluid circulation within the CNS, leading to reduced cerebrospinal fluid (CSF) flow and impaired cerebral hemodynamic responses to hypercapnia.

Mechanistically, we found that perturbation of the CD163$^+$ phenotype affected gene expression and vasodilation in brain arteries. CD163$^+$ BAMs orchestrated communication with vascular cells via angiogenic molecules, including insulin-like growth factor-1 (IGF1). Consistently, conditional IGF1 deletion in brain macrophages phenocopied the vascular defects observed in cMAF knockout (KO) mice.

Moreover, cMAF emerged as the central TF in human CD163$^+$ BAMs, revealing a conserved transcriptional program. CD163$^+$ BAMs in Alzheimer's disease (AD) patients exhibited enhanced cMAF activity together with increased IGF1/IGF1-receptor (IGF1R) communication with brain arteries. This induction, however, was not observed in patients carrying the *APOE4* allele, the major risk factor for AD.[36,37] We also characterized an AD-protective single-nucleotide polymorphism (SNP) within the *MAF* locus associated with elevated *MAF* and *IGF1* expression in CD163$^+$ BAMs. Taken together, these findings suggest that the cMAF program in CD163$^+$ BAMs plays a protective role in neurodegeneration and may represent a promising target for therapeutic intervention.

RESULTS

Transcriptomic and epigenetic analyses identify cMAF as a key TF in CD163$^+$ BAMs

In this study, we focused on CD163$^+$ BAMs, which express high levels of CD163, CD206, CD38, FOLR2, and LYVE1, but not MHC class II, and are enriched in the brain perivascular spaces (Figure 1A). Both MG and CD163$^+$ BAMs originate from a common YS progenitor but undergo divergent specification programs, likely regulated by distinct TFs and epigenetic mechanisms.[27,29] Although previous studies have identified key TFs shaping the microglial phenotype (e.g., SALL1, SMAD4, MAFB, and IRF8),[22,34,38,39] the essential regulators of CD163$^+$ BAM development remain to be determined.

We sought to identify potential regulators of the CD163$^+$ state by single-cell multi-ome analysis of brain macrophages.[22] Single-cell assay for transposase-accessible chromatin using sequencing (scATAC) analysis of differential open chromatin regions (OCRs) revealed broad differences between CD163$^+$ BAMs and MG or MHCII$^+$ BAMs (Figure 1B). The specific genome-wide OCRs for CD163$^+$ BAMs and MG (Figure 1C) likely reflect the activation of distinct transcriptional programs. Motif enrichment analysis identified binding sites for MAF family TFs (cMAF, MAFG, and MAFA) among the top motifs in CD163$^+$ OCRs compared with either MG or MHCII$^+$ OCRs (Figure S1A). Integration of both motif accessibility and expression level covariates revealed cMAF as the most enriched TF in CD163$^+$ BAMs relative to MG (Figure 1D). It was previously demonstrated that SMAD4 is a key driver of the microglial transcriptional program,[22,34] and its deletion in MG results in the upregulation of CD163$^+$ BAM signature genes (i.e., *Apoe*, *Lyz2*, *Mrc1*, *Ms4a7*, and *Pf4*). Consistently, SMAD4-deficient MG also upregulate *Maf* (encoding cMAF) expression (Figure S1B). These data suggest that cMAF may drive the CD163$^+$ program in BAMs, while SMAD4 suppresses cMAF in MG to promote the microglial program.

To test this hypothesis, we performed chromatin immunoprecipitation sequencing (ChIP-seq) for cMAF in BMDMs, which served as an *in vitro* benchmark to assess cMAF genomic occupancy (Figure 1E). In BMDMs, cMAF strongly bound the CD163$^+$ OCRs identified by scATAC-seq but not the microglial OCRs. Analysis of publicly available SMAD4 ChIP-seq data[34] revealed the opposite pattern (Figure 1F). Peaks for both cMAF and SMAD4 were predominantly located within promoters and transcription start sites (TSSs) and intronic and intergenic regions (Figure 1G). When focusing on coding regions, cMAF peaks were enriched in CD163$^+$ BAM genes, whereas SMAD4 peaks overlapped with MG signature genes (Figure 1H). For example, cMAF binding was detected at the loci of CD163$^+$ genes such as *Apoe*, *Cd163*, *Mrc1*, and *Pf4*. Conversely, no cMAF binding was observed in *H2-Ab1*, *H2-Aa*, and *H2-Eb1* genes that define the MHCII$^+$ signature (Figure S1C). Additionally, we performed footprinting analysis of our scATAC data to assess Tn5 transposase insertions (defining open chromatin) near cMAF motifs

Please cite this article in press as: Brioschi et al., Brain perivascular macrophages regulate endothelial cell function via a cMAF-dependent transcriptional program in mouse and human, Cell (2026), https://doi.org/10.1016/j.cell.2026.07.043

CellPress
OPEN ACCESS

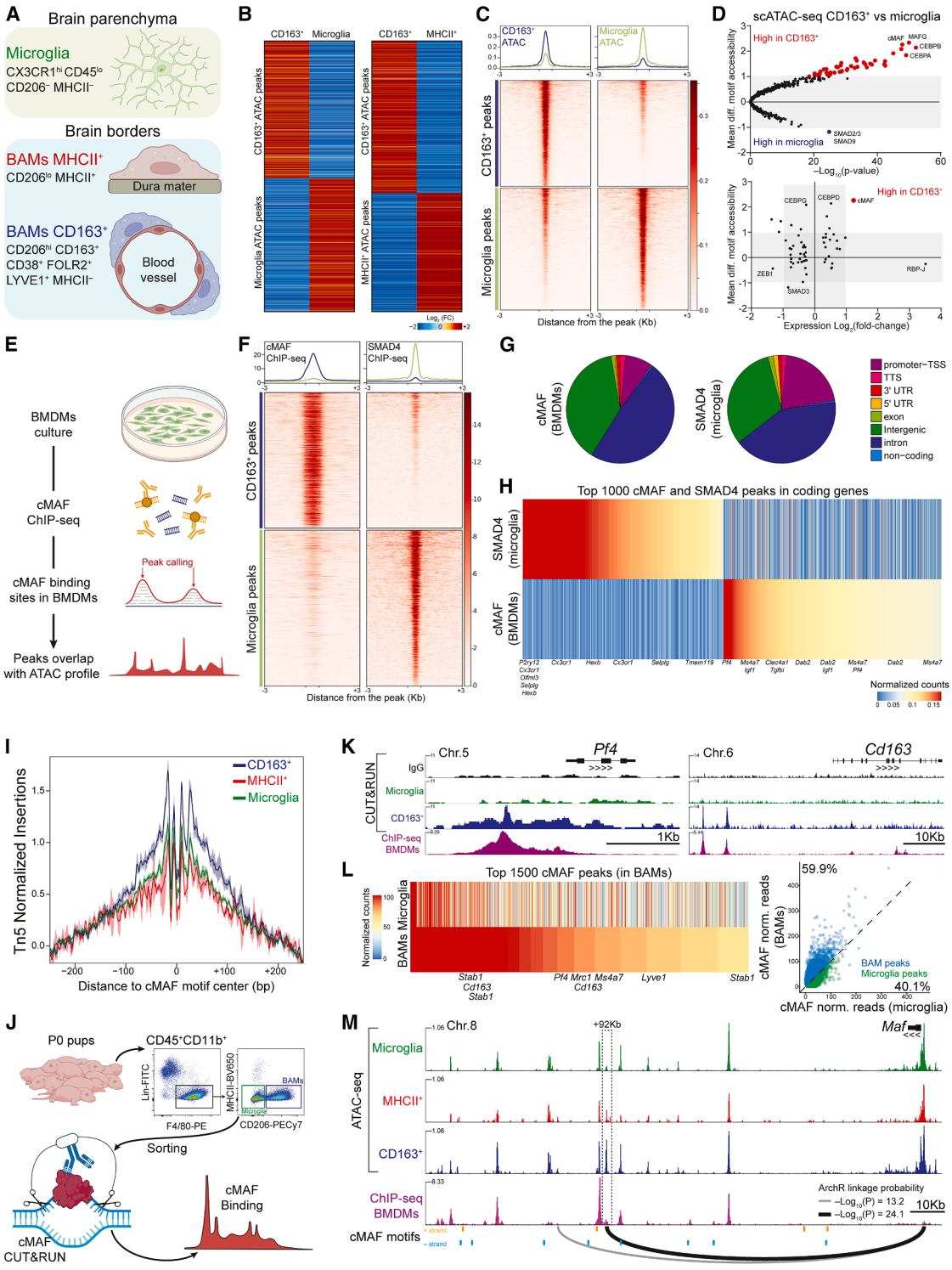

Figure 1. cMAF is the top enriched TF in CD163$^+$ BAMs

(A) Cartoon illustrating the phenotypes of brain macrophages.

(B) Heatmaps of the differential OCRs in scATAC-seq data.

(C) ATAC-seq coverage for differential OCRs between CD163$^+$ BAMs and MG.

(D) Volcano plot depicting the mean chromVAR motif deviation in CD163$^+$ BAMs versus MG (top), and the correlation between chromVAR deviation and expression enrichment in CD163$^+$ BAMs versus MG (bottom).

(legend continued on next page)

Please cite this article in press as: Brioschi et al., Brain perivascular macrophages regulate endothelial cell function via a cMAF-dependent transcriptional program in mouse and human, Cell (2026), https://doi.org/10.1016/j.cell.2026.07.043

in a genome-wide manner. This analysis revealed increased chromatin accessibility at cMAF motifs (indicating greater cMAF binding) in CD163$^+$ BAMs compared with MHCII$^+$ BAMs and MG (Figure 1I). To further test cMAF occupancy at the CD163$^+$ BAM signature genes *in vivo*, we performed CUT&RUN (cleavage under targets and release using nuclease) for cMAF in MG and BAMs sorted from newborn brains (Figure 1J). This analysis confirmed strong cMAF binding at CD163$^+$ BAM genes (such as *Cd163*, *Mrc1*, *Pf4*, *Ms4a7*, *Stab1*, and *Lyve1*) and overall greater DNA binding in BAMs compared with MG (Figures 1K and 1L). These findings suggest that cMAF is directly involved in regulating CD163$^+$ BAM gene expression.

To validate the role of cMAF in promoting this transcriptional program, we performed CRISPR-Cas9-mediated deletion of *Maf* (as well as *Mafb* to prevent compensatory mechanisms) in BMDMs and analyzed gene expression changes using bulk RNA sequencing (RNA-seq) (Figure S1D). Consistently, CD163$^+$ genes (*Stab1*, *Fcrls*, *Apoe*, *Mrc1*, *Clec4a1*, *Pf4*, *F13a1*, and *Cd163*) were downregulated in double KO (dKO) BMDMs, whereas cell-cycle-related genes (*Top2a*, *Stmn1*, and *Mki67*) and stem-cell genes (*Cd34*) were upregulated (Figures S1E and S1F). The downregulation of *Mrc1*, a hallmark CD163$^+$ signature gene, was further confirmed by qPCR (Figure S1G). These data suggest that, in the absence of *Maf*, BMDMs undergo de-differentiation and downregulate BAM signature genes while activating self-renewal mechanisms.[40,41]

Lastly, we investigated whether the *Maf* locus exhibited differential accessibility across our populations of interest. Although no obvious differences were observed at the *Maf* promoter, the non-coding region extending up to 150 kb downstream of the *Maf* TSS contained several ATAC peaks with varying accessibility. Notably, the +92 kb peak was highly specific to CD163$^+$ BAMs and displayed significant linkage to the *Maf* promoter (Figure 1M). These observations suggest that expression of cMAF in CD163$^+$ BAMs is likely regulated by a specific repertoire of active enhancers.

cMAF sustains the CD163$^+$ BAM phenotype *in vivo*

To demonstrate that cMAF is a key TF for CD163$^+$ BAMs *in vivo*, we crossed *Maf-flox* mice[42] with the *Crybb1-Cre* line[22] (hereafter *Maf$^{f/f}$: Cre*) (Figure 2A), which mediates recombination in virtually all MG and CD163$^+$ BAMs during the third embryonic week. Flow cytometry analysis of BAMs (Figure S2A) identified two major populations: CD163$^+$MHCII$^-$ cells (corresponding to CD163$^+$ BAMs) and CD163$^-$MHCII$^+$ cells (corresponding to MHCII$^+$ BAMs). Strikingly, the CD163$^+$MHCII$^-$ population was almost completely absent in *Maf$^{f/f}$: Cre* mice (Figure 2B). Similar results were obtained when gating on CD206^{hi}MHCII$^-$ cells (Figure S2B), confirming the reproducibility of the observed phenotype regardless of the gating strategy. These data indicate that cMAF is essential for the development or maintenance of the CD163$^+$ population enriched in perivascular spaces.

Next, we performed ADAPT-3D (accelerated deep adaptable processing of tissue for three-dimensional fluorescence tissue imaging),[43] a non-shrinking technique that enables high-resolution deep tissue imaging of cleared brains to visualize BAMs in the leptomeninges and perivascular compartments (Figure 2C). Although CD206$^+$ BAMs were abundant in the *Maf$^{f/f}$* brain, MHCII$^+$ BAMs became the main population in *Maf$^{f/f}$: Cre* mice. This phenotypic shift in BAMs was further confirmed by immunofluorescent staining for CD206 and MHC class II or LYVE1 and F4/80 on brain sections from *Maf$^{f/f}$: Cre* mice (Figures 2D and S2C). Compared with *Maf$^{f/f}$* littermate controls, *Maf$^{f/f}$: Cre* mice exhibited a remarkable expansion of MHCII$^+$ perivascular macrophages, while LYVE1$^+$ macrophages were markedly reduced (Figure 2E). No change was noted in the vascular density throughout the brain cortex (Figure S2D), indicating that the phenotype observed in perivascular macrophages is unlikely to result from vascular atrophy or malformation in *Maf$^{f/f}$: Cre* mice. Interestingly, analysis of BAMs in P0 pups revealed negligible differences between genotypes (Figure S2E), suggesting that the transcriptional derailment due to cMAF deficiency emerges postnatally, presumably between birth and 4 weeks of age.

We then assessed the microglial phenotype by flow cytometry, focusing on key surface markers of homeostatic microglia (HM) (CX3CR1, TMEM119, SIGLEC-H, MERTK, and P2RY12). MG from *Maf$^{f/f}$: Cre* mice did not upregulate MHC class II and maintained expression of all assessed markers, with CX3CR1, MERTK, and P2RY12 being slightly downregulated (Figure 2F). This finding was further corroborated by immunofluorescent staining for IBA1 and TMEM119 on brain sections, showing no differences in microglial density or IBA1 and TMEM119 staining between genotypes (Figure 2G). We conclude that cMAF conditional deletion in brain macrophages during embryonic development induces dramatic phenotypic changes in CD163$^+$ BAMs, while MG remain largely unaffected.

Finally, we tested whether cMAF deletion induced replacement of resident CD163$^+$ BAMs by monocyte-derived macrophages through parabiosis of *Maf$^{f/f}$* and *Maf$^{f/f}$: Cre* littermates with transgenic mice expressing green fluorescent protein under the ubiquitin C promoter (UBC-GFP). After 6 weeks of shared circulation, despite substantial blood chimerism being detected in both genotypes (Figure 2H), virtually no GFP$^+$ (parabiont-derived) macrophages could be observed within the brain perivascular compartments (Figure 2I). Conversely, sparse GFP$^+$

(E) Cartoon illustrating the workflow for ChIP-seq of cMAF in BMDMs.
(F) Visualization of the cMAF ChIP-seq (BMDMs) or SMAD4 ChIP-seq (MG) coverage over the differential ATAC-seq OCRs between CD163$^+$ BAMs and microglia.
(G) Genomic annotations for cMAF and SMAD4 ChIP-seq peaks.
(H) Heatmap of the top 1,000 cMAF and SMAD4 ChIP-seq peaks within coding genes.
(I) cMAF motif footprinting in the three populations of brain macrophages in scATAC-seq data.
(J) Cartoon illustrating the workflow and sorting strategy of brain macrophages for cMAF CUT&RUN.
(K) cMAF CUT&RUN and ChIP-seq tracks at the *Pf4* and *Cd163* loci.
(L) Heatmap of the top 1,500 cMAF peaks in BAMs with annotation of key BAM signature genes (left). Correlation of cMAF peaks between BAMs and MG (right).
(M) ATAC-seq and cMAF binding peaks downstream of the *Maf* locus.
See also Figure S1.

Please cite this article in press as: Brioschi et al., Brain perivascular macrophages regulate endothelial cell function via a cMAF-dependent transcriptional program in mouse and human, Cell (2026), https://doi.org/10.1016/j.cell.2026.07.043

CellPress
OPEN ACCESS

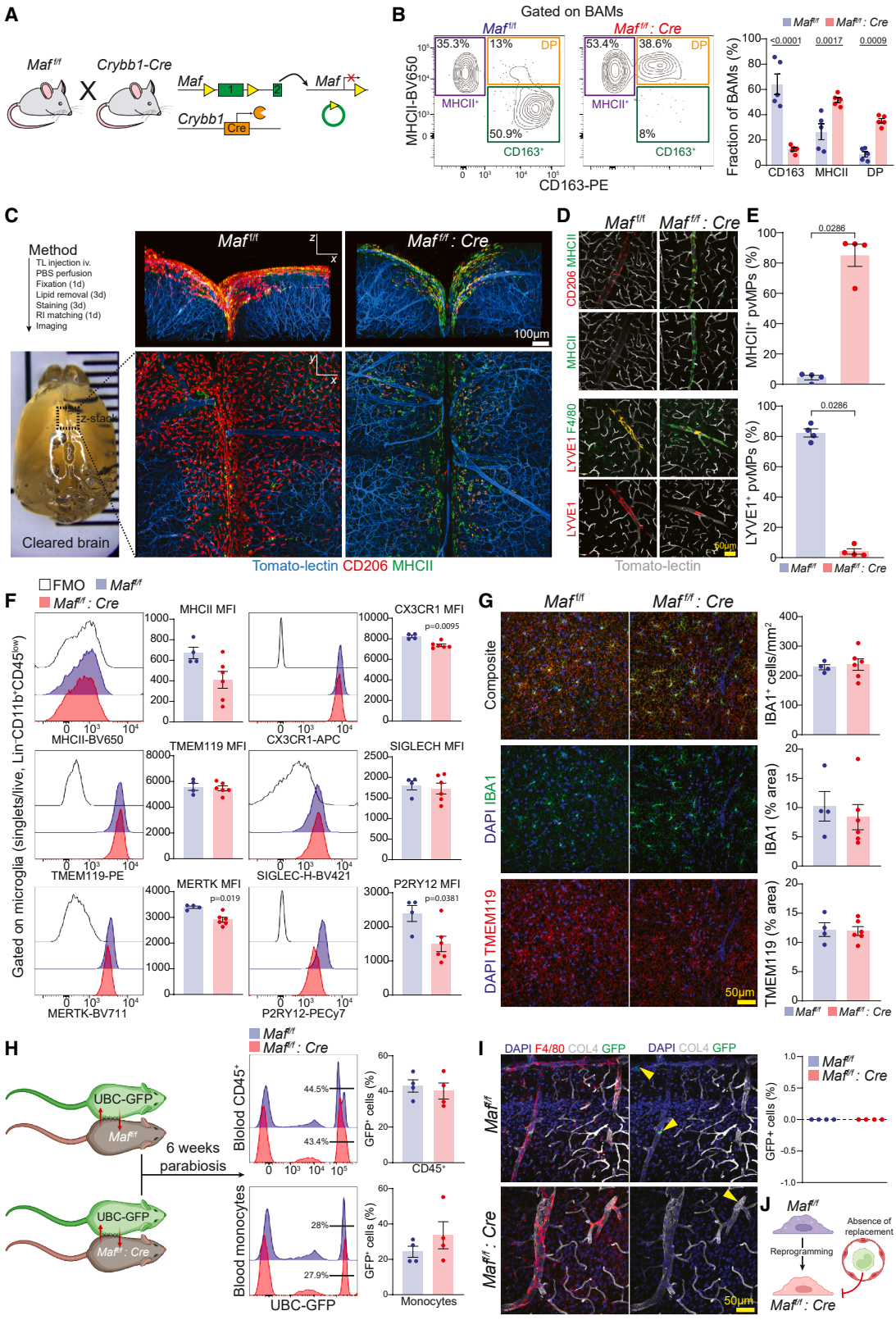

(legend on next page)

Please cite this article in press as: Brioschi et al., Brain perivascular macrophages regulate endothelial cell function via a cMAF-dependent transcriptional program in mouse and human, Cell (2026), https://doi.org/10.1016/j.cell.2026.07.043

macrophages were found in the choroid plexus and leptomeninges (Figure S2F) regardless of the host genotype. These data strongly suggest that cMAF deficiency does not cause depletion of CD163$^+$ BAMs and ensuing replacement by circulating monocytes but rather triggers a broad phenotypic reprogramming of these macrophages without significantly affecting their longevity (Figure 2J).

Single-cell transcriptomics reveals minor impact of cMAF deficiency in MG

To further investigate these phenotypic changes, we performed single-cell RNA sequencing (scRNA-seq) on total macrophages sorted from mouse brains (Figure S3A). After excluding doublets and low-quality cells, unsupervised clustering using uniform manifold approximation and projection (UMAP) identified several clusters with differential distributions between genotypes. These were annotated as follows: HM, KO Mg, two interferon (IFN)-responsive MG clusters (IFN-1 and IFN-2), mitotic MG, and BAMs (Figures S3B and S3C).

We found that KO Mg upregulated genes such as *Apoe*, *Arhgap15*, and *Tmem176a*, while downregulating homeostatic microglial markers such as *Csmd3*, *Nav3*, and *Maf* (Figure S3D). Notably, *Maf* expression was almost completely abolished in *Maf$^{f/f}$: Cre* mice (Figure S3E), confirming efficient deletion. Considering the genotypes present in each cluster, HM and the IFN-1 cluster were almost exclusively derived from *Maf$^{f/f}$* control mice, while KO Mg, IFN-2, and the mitotic cluster predominantly originated from *Maf$^{f/f}$: Cre* mice. In contrast, total BAMs were equally represented in both genotypes (Figure S3F).

Next, we analyzed differentially expressed genes (DEGs; $\log_2$(fold-change) > 1 or < −1) between genotypes and identified 25 DEGs in MG and 20 in BAMs (Figures S3G and S3H). Some DEGs were shared between both populations, including the upregulation of *Apoe* and *Tmem176a* and the downregulation of *Fcrls* and *Maf* (Figure S3I). Overall, we conclude that although cMAF deletion in MG induces some transcriptional changes, its impact appears relatively minor compared with KOs of other TFs such as *SMAD4*, *SALL1*, or *IRF8*.[22,34,38,44]

Phenotypic reprogramming of CD163$^+$ BAMs upon cMAF deletion

To better assess changes in BAM subsets, we re-clustered the BAM population separately, resolving two main populations corresponding to the MHCII$^+$ and CD163$^+$ BAM phenotypes (Figures 3A and 3B). The MHCII$^+$ cluster was enriched for MHC class II-related genes (*H2-Aa* and *Cd74*), the chemokine receptor *Ccr2*, and the immunomodulatory molecule *Cd52* (Figure 3C). Conversely, the CD163$^+$ cluster was enriched for the scavenger receptors *Cd163* and *Mrc1* (CD206), the Fc receptor-like molecule *Fcrls*, and the hyaluronan receptor *Lyve1* (Figure 3D). *Maf* expression was prominent in CD163$^+$ BAMs and positively correlated with CD163$^+$ signature genes (Figures 3E and 3F). However, *Maf* transcript expression was barely detectable in *Maf$^{f/f}$: Cre* mice, confirming successful gene deletion (Figure 3G).

Next, we assessed the relative contribution of each genotype to the two BAM populations. Although the MHCII$^+$ cluster contained a larger fraction of cells from *Maf$^{f/f}$: Cre* mice, the CD163$^+$ cluster was composed almost exclusively of cells from *Maf$^{f/f}$* control mice (Figure 3H). In other words, the CD163$^+$ BAM population was largely ablated in *Maf$^{f/f}$: Cre* mice. Lastly, we analyzed DEGs in MHCII$^+$ BAMs, comparing genotypes. Only a few DEGs were identified, and *Maf* emerged as the most downregulated gene, indicating that MHCII$^+$ BAMs are phenotypically similar in both genotypes (Figures 3I and 3J). Altogether, these findings demonstrate that the CD163$^+$ signature in BAMs critically depends on cMAF, and its deletion leads to the near-complete ablation of this cellular phenotype.

cMAF deletion in CD163$^+$ BAMs impairs CSF flow

Because of their strategic location at the brain borders, including the abluminal surface of CNS the vasculature, BAMs are directly exposed to CSF. Previous studies have shown that complete BAM depletion through genetic deletion (*Lyve1-Cre: Csf1r$^{fl/fl}$*) or injection of clodronate-filled liposomes negatively impacts CSF flow.[45] To assess CSF circulation in *Maf$^{f/f}$: Cre* mice, we performed intra-cisterna magna (icm) injections of fluorophore-conjugated ovalbumin (OVA) and monitored fluorescence

Figure 2. cMAF is required to maintain CD163$^+$ BAMs *in vivo*

(A) Cartoon illustrating the cMAF conditional deletion strategy using *Crybb1-Cre*.

(B) Flow cytometry analysis of the BAM phenotypes in *Maf$^{f/f}$* and *Maf$^{f/f}$: Cre* littermate mice (n = 5 mice per genotype, 5–7 weeks old; two-way ANOVA and Sidak's multiple comparisons test, mean ± SEM; two independent experiments).

(C) Confocal imaging of cortical BAMs in whole-brain tissue clearing comparing *Maf$^{f/f}$* and *Maf$^{f/f}$: Cre* littermate mice (4 weeks old, single experiment).

(D) Confocal imaging of brain perivascular macrophages comparing *Maf$^{f/f}$* and *Maf$^{f/f}$: Cre* littermate mice.

(E) Quantification of MHCII$^+$ or LYVE1$^+$ perivascular macrophages comparing *Maf$^{f/f}$* and *Maf$^{f/f}$: Cre* littermate mice (n = 4 mice per genotype, 4 weeks old, average of three images per mouse; Mann-Whitney U test, mean ± SEM; two independent experiments).

(F) Flow cytometry histograms of microglial markers comparing *Maf$^{f/f}$* and *Maf$^{f/f}$: Cre* littermate mice (n = 4–6 mice per genotype, 8–13 weeks old; Mann-Whitney U test, mean ± SEM; two independent experiments).

(G) Confocal imaging of MG stained for IBA1 and TMEM119 comparing *Maf$^{f/f}$* and *Maf$^{f/f}$: Cre* littermate mice (n = 4–6 mice per genotype, 8–13 weeks old, average of three images per mouse; Mann-Whitney U test, mean ± SEM; two independent experiments).

(H) Flow cytometry analysis of blood chimerism in either CD45$^+$ cells or monocytes (CD11b$^+$Ly6G$^-$CD115$^+$) from *Maf$^{f/f}$* and *Maf$^{f/f}$: Cre* littermates after 6 weeks parabiosis with UBC-GFP mice (n = 4 mice per genotype, 16–18 weeks old at surgery, analysis 6 weeks post-surgery; Mann-Whitney U test, mean ± SEM; three independent experiments).

(I) Confocal imaging of brain perivascular macrophages in *Maf$^{f/f}$* and *Maf$^{f/f}$: Cre* littermates after 6 weeks parabiosis with UBC-GFP mice (n = 4 mice per genotype, average of six images per mouse, Mann-Whitney U test; three independent experiments; yellow arrowheads indicate intravascular GFP$^+$ cells).

(J) Cartoon illustrating the phenotypic conversion, rather than replacement, of brain perivascular macrophages upon cMAF deletion.

See also Figure S2.

Please cite this article in press as: Brioschi et al., Brain perivascular macrophages regulate endothelial cell function via a cMAF-dependent transcriptional program in mouse and human, Cell (2026), https://doi.org/10.1016/j.cell.2026.07.043

CellPress
OPEN ACCESS

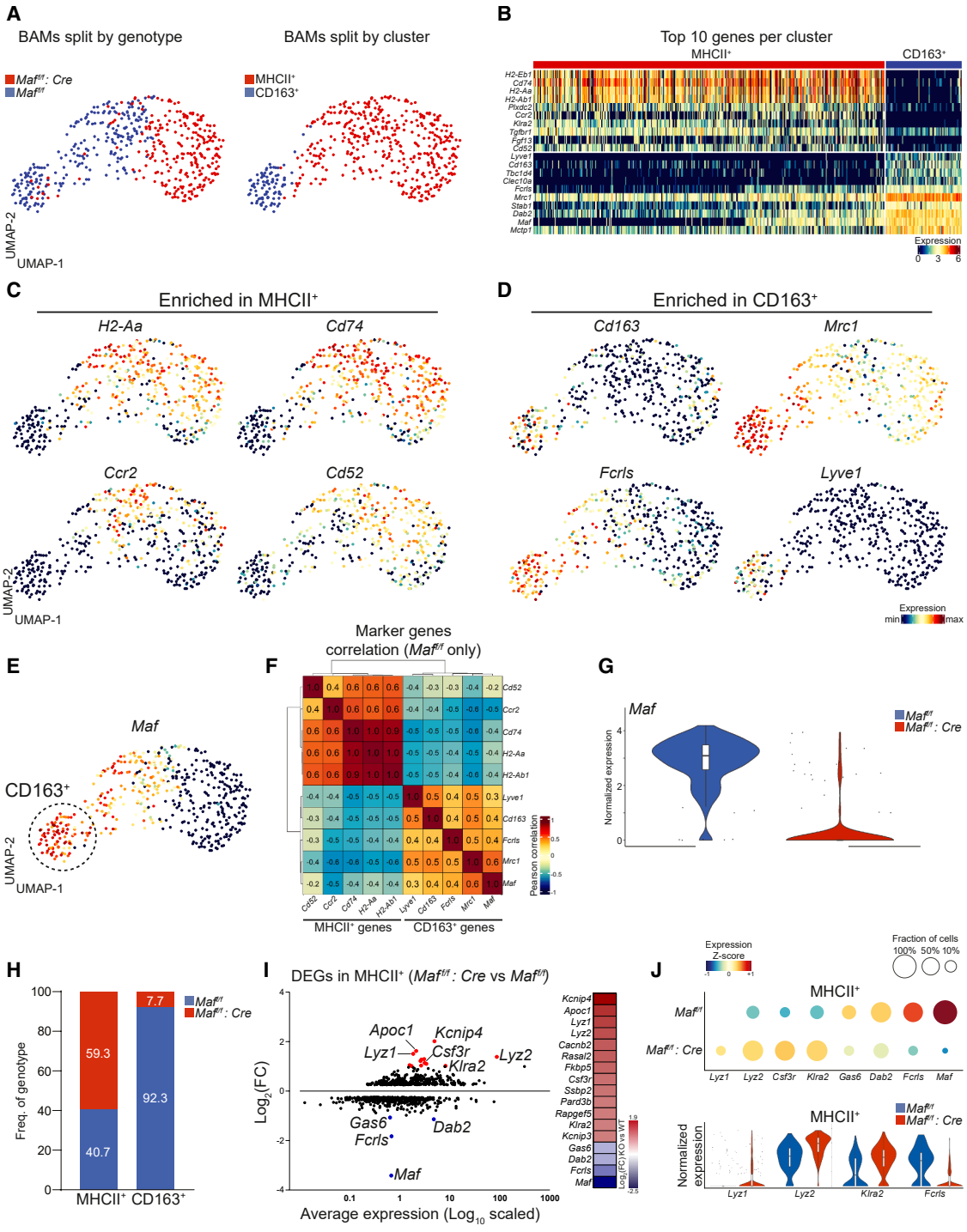

Figure 3. CD163$^+$ BAMs undergo a phenotypic switch in the absence of cMAF

(A) scRNA-seq data of BAMs re-clustered from total brain macrophages (n = 2 mice per genotype, 8 weeks old).

(B) Gene-by-cell heatmap of the top 10 genes per cluster.

(C) Visualization of MHCII$^+$ BAM marker gene expression.

(D) Visualization of CD163$^+$ BAM marker gene expression.

(E) Visualization of *Maf* gene expression.

(F) Pearson correlation of MHCII$^+$ and CD163$^+$ BAM marker genes in *Maf$^{f/f}$* mice.

(G) Violin plot of *Maf* expression comparing *Maf$^{f/f}$* and *Maf$^{f/f}$: Cre* cells.

(legend continued on next page)

Please cite this article in press as: Brioschi et al., Brain perivascular macrophages regulate endothelial cell function via a cMAF-dependent transcriptional program in mouse and human, Cell (2026), https://doi.org/10.1016/j.cell.2026.07.043

accumulation along the perivascular space of the middle cerebral artery (MCA) over a 1-h observation period (Figure 4A). OVA influx along the MCA was significantly impaired in *Maf$^{f/f}$: Cre* mice for the first 28 min post-injection, after which both groups plateaued (Figures 4B–4D). Postmortem analysis of OVA distribution within the brain parenchyma confirmed reduced coverage and intensity of the injected tracer (Figures 4E and 4F). In contrast, intra-striatal injections of OVA (45 kDa) and dextran (10 kDa) revealed no significant differences in diffusion within the brain parenchyma (Figures S4A and S4B). These findings suggest that cMAF deletion in CD163$^+$ BAMs impairs CSF circulation within the CSF-filled subarachnoid space, where BAMs are abundant, while interstitial fluid dynamics in the brain parenchyma remain unaffected.

cMAF deletion in CD163$^+$ BAMs disrupts CBF dynamics

Next, we asked whether cMAF deletion in CD163$^+$ BAMs could impact CNS hemodynamics. To test this, we performed cerebral blood flow (CBF) analysis using multi-parametric photoacoustic microscopy (PAM) of brain blood vessels. Mice underwent a 30-min PAM scan under steady-state conditions while breathing room air, followed by a second 30-min scan under hypercapnic conditions (10% CO_2) to induce brain hyperemia (Figure 4G). Remarkably, while *Maf$^{f/f}$* control mice exhibited a significant increase in CBF and dilation of meningeal arteries in response to hypercapnia, *Maf$^{f/f}$: Cre* mice showed no detectable changes (Figures 4H and 4I). Because *Crybb1-Cre* recombines both MG and CD163$^+$ BAMs, we generated *Maf$^{f/f}$: Pf4-Cre* mice to specifically target BAMs[46] and assessed CBF by comparing *Maf$^{f/f}$: Pf4-Cre* and *Maf$^{f/f}$* control mice using the same experimental paradigm described above (Figure S4C). Consistently, *Maf$^{f/f}$: Pf4-Cre* mice exhibited a marked phenotypic conversion in BAMs and an impaired hemodynamic response to hypercapnia compared with littermate controls (Figures S4D and S4E). These findings indicate that molecular perturbation of CD163$^+$ BAMs disrupts the physiological mechanisms underlying cerebrovascular regulation. Despite the observed phenotype, intravenous injection of NHS-biotin revealed no defects in blood-brain barrier (BBB) integrity in cMAF-deficient mice (Figures S4F and S4G). Collectively, these results indicate that the absence of a physiological CD163$^+$ BAM population disrupts both CSF and CBF dynamics. However, consistent with previous reports,[47] BAM perturbation under steady-state conditions does not affect BBB permeability.

cMAF deletion in CD163$^+$ BAMs impairs molecular crosstalk with brain arteries

Having established that cMAF deletion disrupts the phenotype of CD163$^+$ BAMs and affects CSF flow and cerebrovascular responses to hypercapnia, we assessed potential cell-extrinsic effects on the neurovascular unit. To this end, we performed scRNA-seq on CD45$^-$ cells sorted from the brain cortex of *Maf$^{f/f}$* control and *Maf$^{f/f}$: Cre* mice (Figure S5A). After quality control and unsupervised clustering, we identified distinct clusters corresponding to endothelial cells (*Flt1*, *Cdh5*, *Ly6c1*, and *Pecam1*), neuroblasts (*Nav3*, *Map2*, *Sox11*, and *Dcx*), pericytes (*Vtn*, *Rgs5*, and *Pdgfrb*), vascular smooth muscle cells (vSMCs; *Acta2*, *Myh11*, and *Tagln*), astrocytes (*Slc1a2*, *Slc1a3*, and *Gpc5*), oligodendrocytes (*Plp1*, *Mbp*, and *Mag*), and a small fraction of fibroblasts (*Slc4a10*, *Ptgds*, and *Mgp*) and ependymal cells (*Ttr*, *Enpp2*, and *Ncam1*) (Figure S5B).

We then re-clustered the vascular cells (endothelial cells, pericytes, and vSMCs) to better explore phenotypic changes within this compartment (Figure 5A). This analysis resolved endothelial cell populations corresponding to arteries (*Vegfc*, *Mgp*, *Glul*, *Gkn3*, and *Bmx*), veins (*Vwf*, *Vcam1*, *Il1r1*, *Icam1*, and *Cfh*), and capillaries (*Tfrc*, *Spock2*, *Slc7a5*, *Cxcl12*, and *Car4*), while those corresponding to arterioles and venules exhibited an intermediate phenotype among these endothelial cell types (Figure 5B). The overall frequency of these populations remained unchanged between genotypes (Figure 5C). However, several DEGs were identified, particularly in arterial endothelial cells, which exhibited both upregulated and downregulated transcripts (Figure 5D).

Given that perivascular macrophages are predominantly localized in the arterial perivascular space[29] and that brain arteries regulate both CBF and CSF flow,[48,49] we focused our downstream analysis on this cell population. Differential expression analysis in pseudo-bulk revealed that several key genes involved in vascular functions were downregulated in *Maf$^{f/f}$: Cre* mice, including constituents of the vascular ECM (*Eln*, *Col5a2*, *Mgp*, and *Fbln5*), metalloproteinase inhibitors (*Timp2*), and enzymes regulating vasodilation (*Ptgis*). Conversely, negative regulators of eNOS (*Nostrin*) and plasminogen activators (*Plaur*) were upregulated (Figure 5E). Consistently, differential pathway analysis in arteries using both Gene Ontology (GO) term enrichment analysis and gene set enrichment analysis (GSEA) revealed a significant downregulation of pathways related to ECM production or assembly and elastic fiber formation in *Maf$^{f/f}$: Cre* mice (Figures S5C and S5D).

Next, we analyzed the CellChat ligand-receptor network between BAMs and vascular cells and found that several interactions between CD163$^+$ BAM ligands and arterial receptors were lost in *Maf$^{f/f}$: Cre* mice (Figure 5F). Among these, the GAS6 to MERTK and IGF1 to IGF1R ligand-receptor pairs emerged as the most significantly affected. Further comparison of MHCII$^+$ and CD163$^+$ ligand signaling to arteries confirmed that these networks were enriched in CD163$^+$ BAMs (Figure 5G). Consistently, a population of *Gas6-Igf1* double-positive BAMs was present in *Maf$^{f/f}$* but not in *Maf$^{f/f}$: Cre* mice (Figure 5H). To further validate these findings, we employed NicheNet, an alternative computational framework for analyzing intercellular communication across cell types. Consistently, this analysis confirmed that the GAS6- and IGF1-dependent signaling

(H) Frequency of *Maf$^{f/f}$* and *Maf$^{f/f}$: Cre* cells in each BAM cluster.
(I) Scatterplot and heatmap displaying the DEGs in the MHCII$^+$ BAM cluster between genotypes ($\log_2$(fold-change) > 1 or < −1, $p < 0.01$).
(J) Dot plot and violin plots of selected DEGs in the MHCII$^+$ BAM cluster between genotypes.
See also Figure S3.

Please cite this article in press as: Brioschi et al., Brain perivascular macrophages regulate endothelial cell function via a cMAF-dependent transcriptional program in mouse and human, Cell (2026), https://doi.org/10.1016/j.cell.2026.07.043

CellPress
OPEN ACCESS

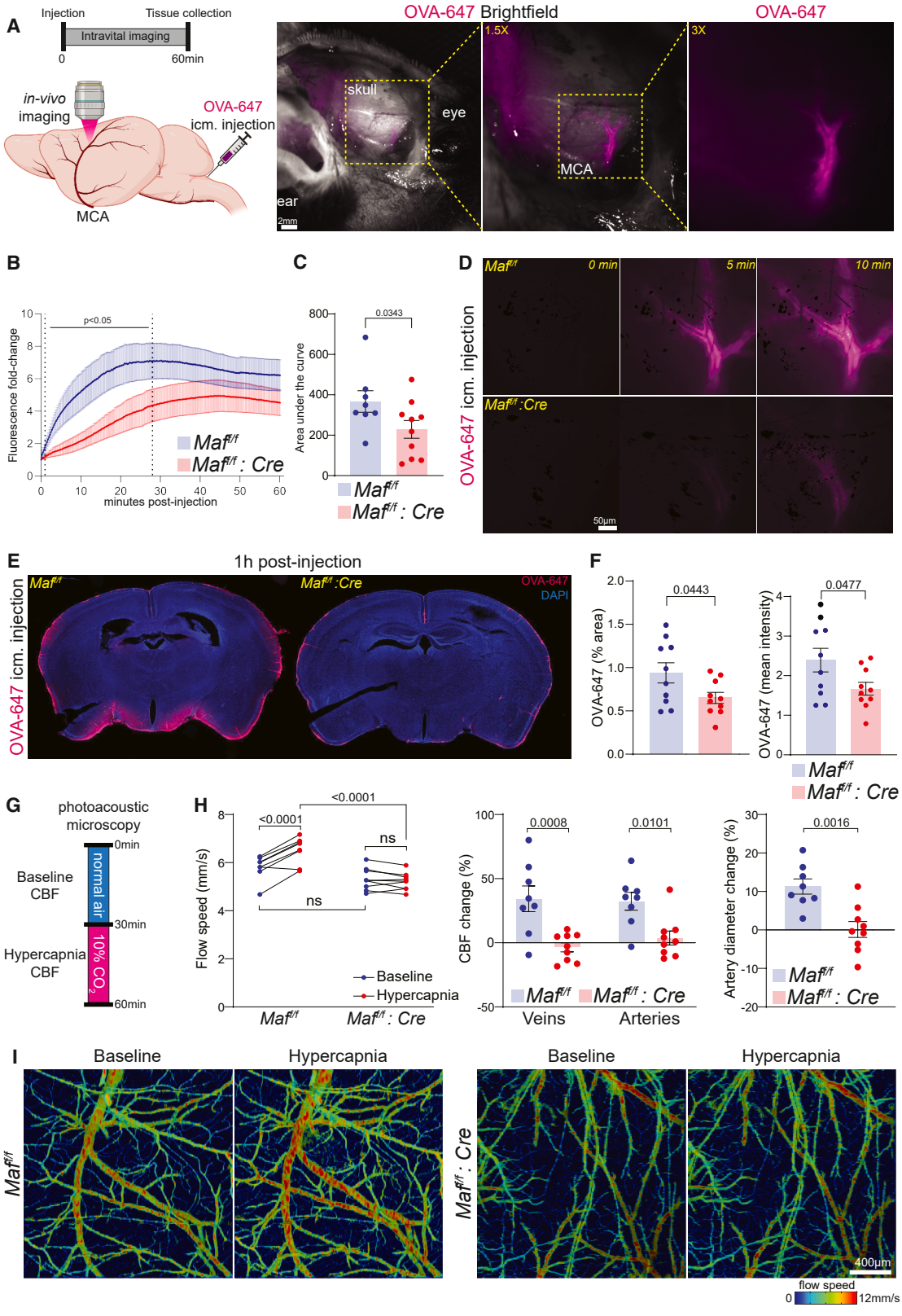

(legend on next page)

Please cite this article in press as: Brioschi et al., Brain perivascular macrophages regulate endothelial cell function via a cMAF-dependent transcriptional program in mouse and human, Cell (2026), https://doi.org/10.1016/j.cell.2026.07.043

pathways were specifically enriched in CD163$^+$ BAMs (Figures S5E and S5F). Presence of *Igf1* RNA in brain perivascular macrophages (corresponding to CD163$^+$ BAMs) was confirmed *in situ* by RNAscope (Figure S5G). Furthermore, evidence of cMAF binding at both *Gas6* and *Igf1* promoters in CD163$^+$ BAMs and BMDMs (assessed by CUT&RUN and ChIP-seq, respectively) was consistent with a direct role of cMAF in the transcription of these genes (Figure 5I). To confirm the functional relevance of IGF1 and GAS6 in endothelial cells, we cultured primary aortic endothelial cells or sorted brain endothelial cells (BECs) with these factors and performed bulk RNA-seq (Figure S5H). Stimulation with IGF1 and GAS6 induced upregulation of several genes involved in blood pressure regulation, ECM production, and vascular dynamics (Figure S5I). These transcriptional changes resulted in enrichment of pathways related to cholesterol and lipid metabolism, vasculature development, angiogenesis, ECM organization, vSMC cell proliferation, and circulatory system regulation (Figures S5J and S5K).

Finally, we directly demonstrated that IGF1 derived from CD163$^+$ BAMs is required to sustain cerebrovascular function using two independent approaches. First, we sorted BECs from *Maf$^{f/f}$: Cre* and *Maf$^{f/f}$* littermate mice and performed western blot analysis for phospho-IGF1R. Our results showed a reduction in IGF1R phosphorylation at both autophosphorylation and signaling tyrosine residues (Tyr1135 and Tyr980, respectively) in BECs from *Maf$^{f/f}$: Cre* mice (Figure 5J). These data suggest that BECs exhibit reduced IGF1R dimerization (likely due to lower ligand availability) and impaired IGF1R signaling when cMAF is deleted in CD163$^+$ BAMs. Second, we generated *Igf1$^{f/f}$: Crybb1-Cre* (*Igf1$^{f/f}$: Cre*) mice to delete IGF1 in brain macrophages and assessed CBF dynamics using the same experimental paradigm as that used in *Maf$^{f/f}$: Cre* mice (Figure 5K). Our analysis confirmed that IGF1 deletion in CD163$^+$ BAMs is sufficient to impair CBF regulation and arterial dilation during hypercapnia, thereby recapitulating the phenotype observed in *Maf$^{f/f}$: Cre* mice (Figure 5L). These data demonstrate that CD163$^+$ BAMs critically modulate BEC function through a cMAF-dependent transcriptional program encompassing IGF1 production.

cMAF is a key TF in human CD163$^+$ BAMs

To assess the TF repertoire in human brain macrophages, we merged and harmonized multiple publicly available single-nucleus RNA sequencing (snRNA-seq) datasets of the human brain,[50–53] retaining only data from healthy subjects. This approach enabled the identification of all major brain cell populations (Figure S6A), including neurons, oligodendrocytes, astrocytes, endothelial cells, mural cells (pericytes and vSMCs), and macrophages, which were subsequently re-clustered separately. Consistent with our findings in mice, we identified three major brain macrophage populations: MG, HLA-DR$^+$ BAMs, and CD163$^+$ BAMs (Figure 6A). These populations exhibited conserved expression of marker genes (Figure 6B). For instance, human MG were enriched for *NAV3*, *P2RY12*, and *CX3CR1* and HLA-DR$^+$ BAMs for *SPP1*, *HIF1A*, and *CD83*, while CD163$^+$ BAMs expressed high levels of *F13A1*, *MRC1*, and *LYVE1* (Figure 6C). Notably, *MAF* expression was primarily enriched in CD163$^+$ BAMs and positively correlated with the CD163$^+$ signature genes (Figures 6D and 6E). To further investigate transcriptional regulation in these populations, we applied single-cell regulatory network inference and clustering (SCENIC), an algorithm that identifies gene regulatory networks (or regulons) across cell types and states. This analysis revealed several TFs with differential activity between MG, HLA-DR$^+$ BAMs, and CD163$^+$ BAMs. Remarkably, *MAF* emerged as the most enriched TF in CD163$^+$ BAMs, suggesting that the cMAF-dependent transcriptional program in these cells is evolutionarily conserved (Figures 6F and 6G). High expression of cMAF in CD163$^+$ brain perivascular macrophages was validated by immunohistochemistry and immunofluorescent staining (Figures S6B and S6C). Transcriptional network analysis further revealed that cMAF directly or indirectly controls the expression of CD163$^+$ signature genes in human BAMs, such as *MRC1*, *F13A1*, *COLEC12*, and *IGF1* (Figure S6D). Finally, we performed CellChat ligand-receptor network analysis between human BAMs and adult[54] or fetal[55] brain arteries (Figure S6E). In both cases, IGF1 appeared as a putative CD163$^+$ BAM-derived ligand signaling to IGF1R on arteries, suggesting conservation of this intercellular communication pathway. To conclude, CD163$^+$ BAMs exhibit highly similar phenotypes in mouse and human, and the cMAF-dependent program appears conserved across species, suggesting evolutionary selection.

The cMAF program in CD163$^+$ BAMs is protective during AD

Whether BAMs play protective or detrimental roles during neurodegeneration and the relationship between the cMAF program and disease progression remain unknown. To address this

Figure 4. CD163$^+$ BAMs reprogramming impairs CSF and CBF

(A) Cartoon and stereomicroscope images illustrating the experimental design for CSF flow analysis.

(B) icm injected OVA-647 fluorescent signal fold-change over the 1-h imaging period (n = 8–10 mice per genotype, 8–12 weeks old; multiple Mann-Whitney U tests, mean ± SEM; three independent experiments).

(C) Area under the curve of the plot in (B) (n = 8–10 mice per genotype, 8–12 weeks old; Mann-Whitney U test, mean ± SEM; three independent experiments).

(D) Representative images of OVA-647 along the MCA perivascular space during the first 10 min post-injection comparing *Maf$^{f/f}$* and *Maf$^{f/f}$: Cre* littermate mice.

(E) Representative images of OVA-647 influx into the brain parenchyma comparing *Maf$^{f/f}$* and *Maf$^{f/f}$: Cre* littermate mice.

(F) Quantification of OVA-647 influx into the brain parenchyma comparing *Maf$^{f/f}$* and *Maf$^{f/f}$: Cre* littermate mice (n = 10 mice per genotype, 8–12 weeks old, average of eight images per mouse; Mann-Whitney U test, mean ± SEM; three independent experiments).

(G) Cartoon illustrating the PAM experimental paradigm.

(H) Quantification of blood flow speed before and after hypercapnia (two-way ANOVA and Sidak's multiple comparisons test), percentage CBF change (two-way ANOVA and Sidak's multiple comparisons test, mean ± SEM) and artery diameter change (Mann-Whitney U test, mean ± SEM), comparing *Maf$^{f/f}$* and *Maf$^{f/f}$: Cre* littermate mice (n = 8–9 mice per genotype, 8 weeks old; three independent experiments).

(I) Representative PAM images of meningeal blood vessels at baseline and after hypercapnia.

See also Figure S4.

Please cite this article in press as: Brioschi et al., Brain perivascular macrophages regulate endothelial cell function via a cMAF-dependent transcriptional program in mouse and human, Cell (2026), https://doi.org/10.1016/j.cell.2026.07.043

CellPress
OPEN ACCESS

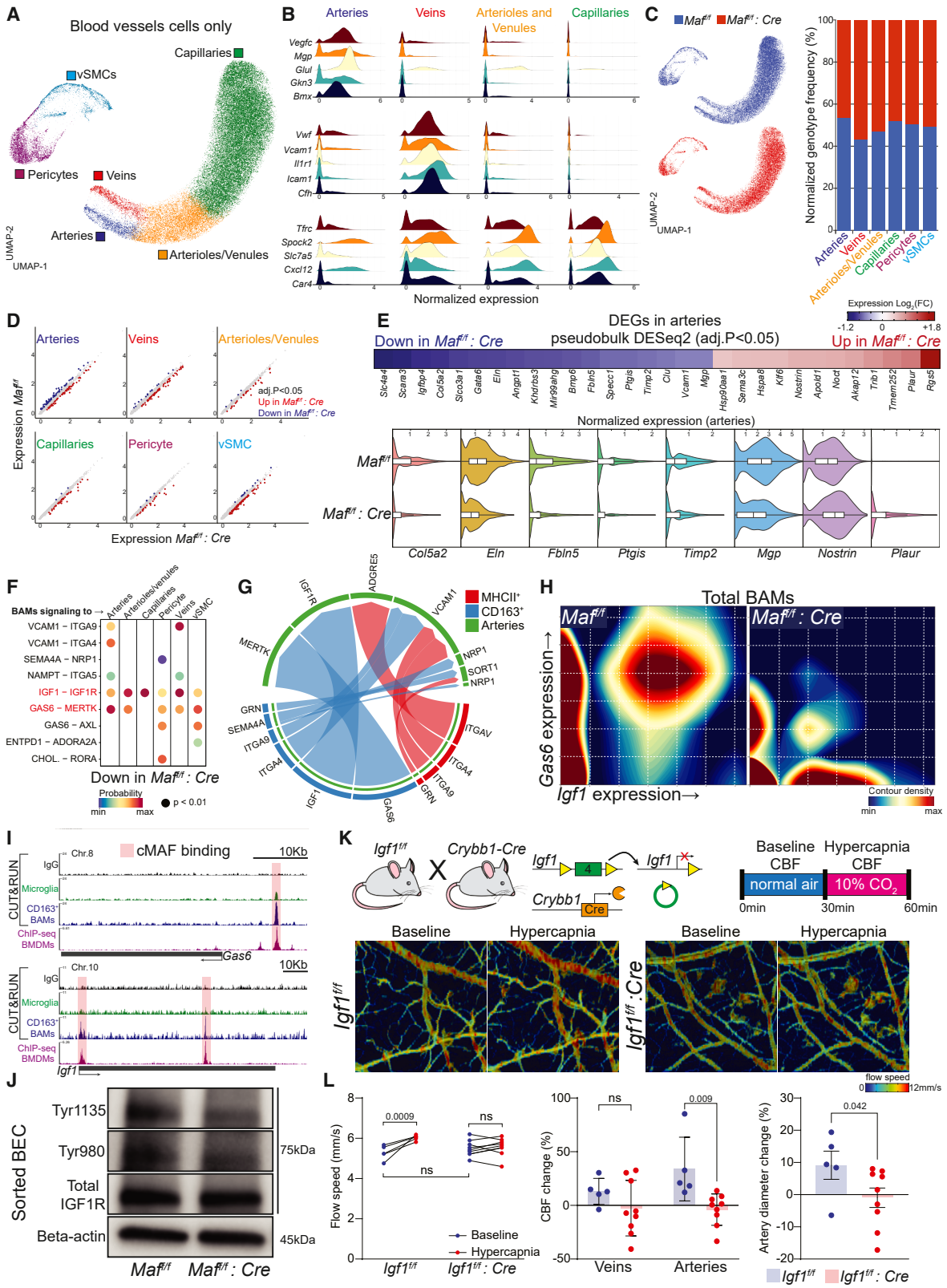

(legend on next page)

Please cite this article in press as: Brioschi et al., Brain perivascular macrophages regulate endothelial cell function via a cMAF-dependent transcriptional program in mouse and human, Cell (2026), https://doi.org/10.1016/j.cell.2026.07.043

knowledge gap, we analyzed brain snRNA-seq data from AD patients and control subjects.[56] After re-clustering macrophages, we resolved MG and CD163$^+$ BAMs (Figure 7A). Focusing on CD163$^+$ BAMs, SCENIC identified cMAF as one of the top enriched regulons in AD patients compared with controls (Figure 7B), with cMAF regulon activity increasing along disease progression (Figure S7A). Alongside *MAF* expression, CD163$^+$ BAMs upregulated angiocrine factors such as platelet-derived growth factor-C (PDGFC) and IGF1 during disease, whereas NAMPT (an angiogenic and pro-inflammatory enzyme also known as visfatin[57]) was downregulated (Figure S7B). The *APOE4* allele is a major genetic risk factor for AD. Interestingly, *MAF* and *IGF1* expression in CD163$^+$ BAMs positively correlated with amyloid-β load in *APOE3* homozygous subjects, but this correlation was lost in *APOE4* carriers. Little or no positive correlation was observed in MG regardless of the *APOE* genotype (Figure 7C).

Moreover, we observed a significant enrichment of pathways regulating angiogenesis and vascular dynamics in arteries from AD patients compared with controls. These pathways largely overlapped with those enriched in arteries from *Maf$^{f/f}$* mice but not those from *Maf$^{f/f}$: Cre* mice lacking the cMAF program (Figure 7D). Consistently, among the top 30 pathways enriched in AD arteries, 13.3% were shared with arteries from *Maf$^{f/f}$* mice but none with *Maf$^{f/f}$: Cre* mice (Figure 7E). In line with this, AD arteries upregulated ECM-regulating genes (such as elastin, FBLN5, MGP, and collagens), many of which were downregulated in arteries from *Maf$^{f/f}$: Cre* mice (Figure 7F). Supporting these findings, CellChat analysis revealed increased vascular endothelial growth factor-B (VEGFB), IGF1, and PDGFC signaling between BAMs and arterial or mural cells in AD patients (Figure 7G). Furthermore, *MAF* expression in CD163$^+$ BAMs and *ELN* expression in arteries were significantly correlated in *APOE3*, but not in *APOE4* patients (Figure S7C), suggesting that cMAF activity in BAMs is linked to increased ECM production in arteries. The presence of CD163$^+$ BAMs expressing cMAF in the perivascular spaces with amyloid-β pathology was confirmed by immunofluorescence (Figure S7D), and the number of these cells was positively correlated with the severity of cerebral amyloid angiopathy (CAA) (Figure S7E). These results indicate that, during AD progression, CD163$^+$ BAMs upregulate the cMAF program and enhance the expression of angiocrine ligands, thereby strengthening communication between BAMs and the vascular compartment. However, this response is blunted in *APOE4* carriers, who are more prone to vascular damage.[58,59]

Finally, we investigated polymorphisms in the *MAF* locus associated with AD and assessed potential causal relationships between *MAF* expression levels and AD risk. Recent genome-wide association studies (GWASs) identified a SNP located ~19 kb downstream of the *MAF* 3′ end (rs450674) that is significantly associated with AD and neuritic plaques.[60,61] Colocalization analysis revealed a significant shared association between genetic regulation of *MAF* expression and AD risk at rs450674 in two independent databases (Bellenguez et al.[60] and MetaBrain EUR) (Figures 7H and S7F). Consistently, the SNP's minor allele (C<T) showed a positive additive effect on *MAF* expression in the total RNA from the cerebral cortex (Figure 7I). Mendelian randomization (MR) analysis revealed a significant negative association between the effect of the SNP on *MAF* expression and AD risk (Figure 7J), suggesting that increased *MAF* expression may confer protection against AD. To determine whether the SNP at rs450674 affects *MAF* expression in brain macrophages, we analyzed human brain snRNA-seq data linked to whole-genome sequencing from 437 individuals[62] (Figure 7K). After resolving MG and CD163$^+$ BAMs, we assessed the relationship between rs450674 genotype and *MAF* RNA levels and found that individuals homozygous for the C/C genotype exhibit approximately 15% higher *MAF* expression in both CD163$^+$ BAMs and MG compared with reference variant individuals (T/T) (Figure 7L). Furthermore, CD163$^+$ BAMs with C/C genotype exhibited more than a 65% increase in *IGF1* expression compared with T/T BAMs (Figure S7G). These data indicate that carriers of the SNP at the *MAF* locus exhibit increased expression of *MAF* as well as cMAF-dependent genes in CD163$^+$ BAMs and are associated with reduced AD risk. Analysis of human scATAC-seq and bulk H3K27Ac ChIP-seq datasets[63,64] further confirmed that this SNP lies immediately adjacent to an ATAC peak in BAMs that is linked to the *MAF* promoter (Figure S7H), within a region showing histone acetylation in brain myeloid cells but not in neurons, oligodendrocytes, or astrocytes (Figure S7I). These data suggest that the SNP

Figure 5. cMAF regulates the crosstalk between CD163$^+$ BAMs and brain arteries

(A) scRNA-seq of the brain vascular compartment (n = 2 mice per genotype, 8 weeks old).
(B) Ridge plots of selected marker genes for each cell cluster.
(C) scRNA-seq dataset split by genotype and frequency of *Maf$^{f/f}$* and *Maf$^{f/f}$: Cre* cells in each cluster.
(D) Scatterplots showing the DEGs between genotypes in each cluster.
(E) Heatmap of the DEGs (DESeq2 adj.p < 0.05) in arteries between genotypes. Expression levels of selected genes are shown by violin plot.
(F) CellChat dot plot of the downregulated ligand-receptor pairs in *Maf$^{f/f}$: Cre* mice (BAMs = sender; vascular cells = receiver).
(G) CellChat chord plot of putative signaling interactions from MHCII$^+$ and CD163$^+$ BAM cells to arteries.
(H) Contour plot of *Igf1* and *Gas6* expression in BAMs comparing genotypes.
(I) cMAF binding peaks at the *Gas6* and *Igf1* promoters in BAMs compared with MG (CUT&RUN) or BMDMs (ChIP-seq).
(J) Western blot for two distinct phospho-IGF1R residues in BECs sorted from *Maf$^{f/f}$* and *Maf$^{f/f}$: Cre* littermate mice (representative of two independent experiments).
(K) Cartoon illustrating the *Igf1* conditional deletion strategy and representative PAM images of meningeal blood vessels at baseline and after hypercapnia.
(L) Quantification of blood flow speed before and after hypercapnia (two-way ANOVA and Sidak's multiple comparisons test), percentage CBF change (two-way ANOVA and Sidak's multiple comparisons test, mean ± SEM) and artery diameter change (Mann-Whitney U test, mean ± SEM), comparing *Igf1$^{f/f}$* and *Igf1$^{f/f}$: Cre* littermate mice (n = 5–9 mice per genotype, 4–5 months old; three independent experiments).
See also Figure S5.

Please cite this article in press as: Brioschi et al., Brain perivascular macrophages regulate endothelial cell function via a cMAF-dependent transcriptional program in mouse and human, Cell (2026), https://doi.org/10.1016/j.cell.2026.07.043

CellPress
OPEN ACCESS

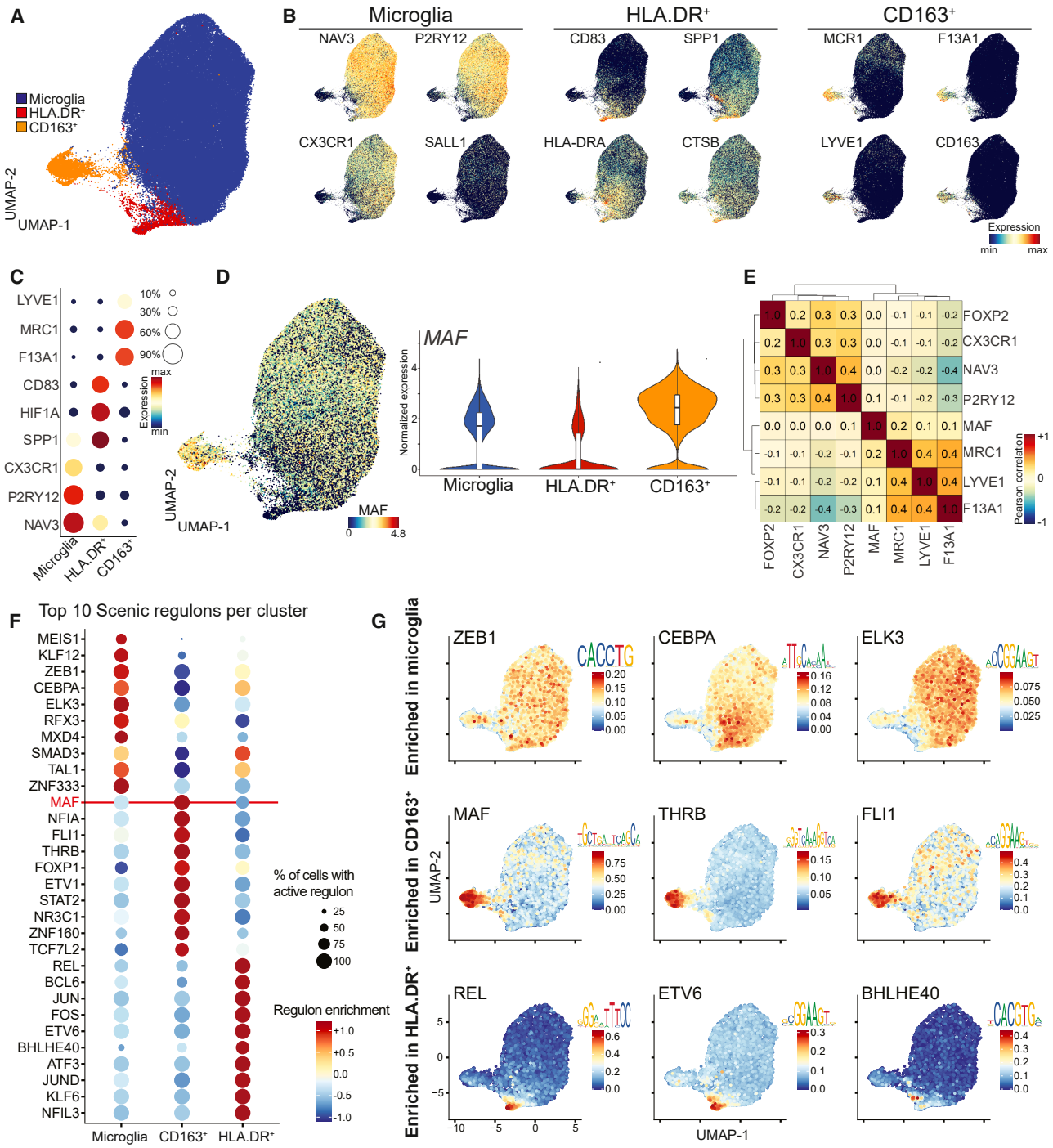

Figure 6. The cMAF transcriptional program is conserved in human CD163⁺ BAMs

(A) Aggregated snRNA-seq data of human brain macrophages colored by cluster assignment.

(B) Visualization of gene expression in single cells for selected signature macrophage genes.

(C) Dot plot of gene expression for three selected marker genes for each macrophage population.

(D) Visualization of *MAF* expression in single cells by feature map (left) and violin plot (right).

(E) Pearson correlation of MG and CD163⁺ BAM marker genes within single cells.

(F) Dot plot of the top 10 SCENIC regulons enriched in each human macrophage cluster.

(G) Visualization of SCENIC regulon enrichment in single cells.

See also Figure S6.

Please cite this article in press as: Brioschi et al., Brain perivascular macrophages regulate endothelial cell function via a cMAF-dependent transcriptional program in mouse and human, Cell (2026), https://doi.org/10.1016/j.cell.2026.07.043

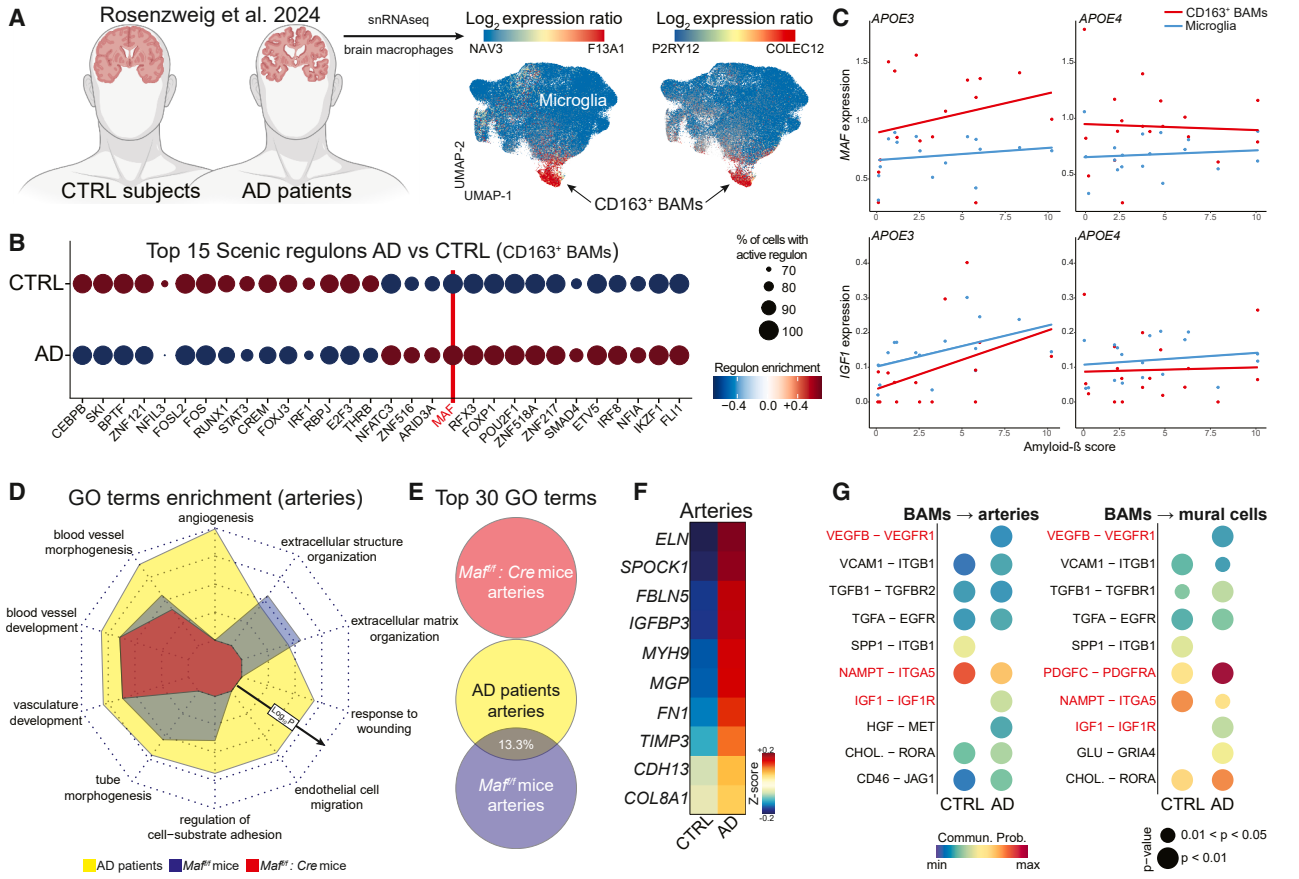

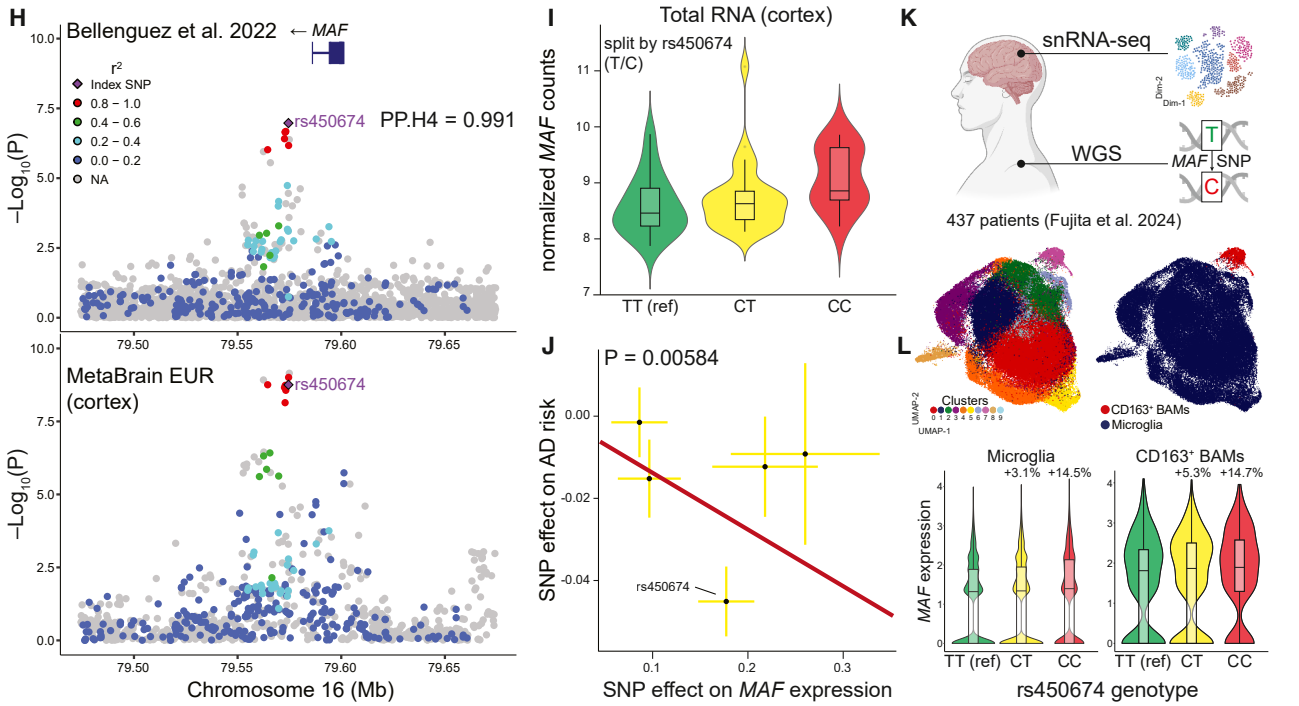

(legend on next page)

Please cite this article in press as: Brioschi et al., Brain perivascular macrophages regulate endothelial cell function via a cMAF-dependent transcriptional program in mouse and human, Cell (2026), https://doi.org/10.1016/j.cell.2026.07.043

resides within a distal *MAF* regulatory element that is predominantly active in BAMs. Furthermore, we found that the SNP maps within a binding motif for the zinc-finger transcriptional activator Zscan29 (encoded by *Zfp690*), and the minor allele increases the predicted binding affinity compared with the reference variant (Figure S7I). Therefore, we propose that the SNP at rs450674 increases *MAF* transcription by augmenting the transcriptional activity of a *cis*-regulatory element at the *MAF* 3′ end.

Lastly, we sought to determine whether the impairment of the cMAF-dependent angiogenic program in the presence of APOE4 is conserved across species. We therefore performed scRNA-seq of brain macrophages from 8-month-old *APOE3* and *APOE4* knockin mice (Figure S7J) and focused on CD163$^+$ BAMs (Figure S7K). Differential expression analysis revealed that several genes linked to communication with endothelial cells are downregulated in the presence of APOE4, including *Igf1*, *Pdgfc*, and *Tfrc* (Figures S7L and S7M). These transcriptomic changes were also associated with the downregulation of multiple biological pathways involved in lipid transport, immune responses, oxidative stress, and regulation of the circulatory system (Figure S7N). Although further studies are required to better understand the underlying mechanisms, our data suggest that APOE4 negatively impacts the ability of CD163$^+$ BAMs to communicate with the brain vasculature. Taken together, these findings suggest that enhancement of cMAF expression in perivascular macrophages confers protection against AD, whereas *APOE4*, a major risk factor for AD, impairs the cMAF transcriptional program in these cells.

DISCUSSION

Recent studies have highlighted the importance of perivascular macrophages (here identified as CD163$^+$ BAMs) in regulating CSF and blood flow dynamics within the CNS.[45,65] However, the transcriptional mechanisms controlling their identity and functions are poorly understood. Our findings show that cMAF drives a transcriptional program that endows perivascular macrophages with vascular-supporting properties, with IGF1 emerging as a central mediator. In the absence of cMAF, perivascular macrophages undergo phenotypic reprogramming and lose IGF1 expression. Although IGF1 promotes angiogenesis in cancer and stroke,[66,67] here we propose that perivascular macrophage-derived IGF1 supports vascular function through direct signaling to endothelial cells[68] and likely other components of the neurovascular unit, including vSMCs.[69] Consistently, mice with cMAF deletion in perivascular macrophages exhibit defective CSF flow and impaired cerebrovascular responses to hypercapnia. This is consistent with a previous report that macrophage-derived IGF1 protects cardiomyocytes in hypertension.[70] A recent study in IL34-deficient mice harboring fewer perivascular macrophages showed increased CBF under steady-state conditions.[65] In our model, cMAF-deficient mice exhibit impaired hemodynamic adaptation to hypercapnia and no CBF changes at baseline. This discrepancy may arise from phenotypic reprogramming rather than depletion of perivascular macrophages. Additionally, *Maf* complete KO embryos are MG-deficient due to impaired differentiation of yolk sac myeloid progenitors,[71] while our conditional KO system, which spares yolk sac progenitors,[22] shows modest changes in MG.

A population of CD206$^+$LYVE1$^+$MHCII$^-$ macrophages associated with blood vessels has been identified across multiple tissues[24,72–75]; however, given the phenotypic heterogeneity of endothelial cells across organs,[76] whether their phenotype and functions are strictly conserved among compartments remains unclear. Indeed, cMAF-deficient macrophages increase vascular branching in adipose tissue,[77] a phenotype not observed in the CNS. Thus, cMAF regulates perivascular macrophage identity, but its downstream effects are likely shaped by the local microenvironment. Beyond IGF1, the cMAF program may protect the brain vasculature through additional mechanisms, such as GAS6, which has been shown to maintain vascular integrity and eNOS expression in endothelial cells,[78] or PDGF-C, which regulates BBB permeability[79] and shapes vSMC development.[80]

The phenotype of perivascular macrophages is highly conserved between mouse and human,[81] and we also demonstrate that the cMAF program is maintained between species.

Figure 7. CD163$^+$ BAMs enhance the cMAF program and vascular crosstalk in AD

(A) snRNA-seq data of human brain macrophages from AD and control subjects colored by Log_2 gene expression ratios of MG and BAM genes.
(B) Dot plot of the top 15 SCENIC regulons enriched in AD versus control subjects within CD163$^+$ BAMs.
(C) Correlation between *MAF* or *IGF1* average gene expression and amyloid pathology score, split by *APOE* genotype and cell type.
(D) Radar chart showing GO terms enriched in arteries from AD patients, and comparative enrichment in arteries from *Maf$^{f/f}$* and *Maf$^{f/f}$: Cre* mice. GO terms computed from DEGs enriched in arteries from AD versus control subjects or enriched in arteries from *Maf$^{f/f}$* versus *Maf$^{f/f}$: Cre* mice.
(E) Venn diagram of the top 30 GO terms in AD arteries compared with GO terms in arteries from *Maf$^{f/f}$* or *Maf$^{f/f}$: Cre* mice.
(F) Heatmap of differential ECM-modulating genes in arteries from AD and control subjects.
(G) CellChat dot plot of the differential ligand-receptor pairs comparing AD and control subjects (BAMs = sender; vascular cells = receiver).
(H) Local plots of the rs450674 locus from two different AD cohorts. Each point represents a variant, with color representing the R^2 to the index SNP rs450674 (purple).
(I) Violin plot showing *MAF* expression in the cerebral cortex from individuals with each genotype: reference variant (TT), heterozygous (CT), and minor allele homozygous (CC).
(J) MR scatterplot for *MAF* expression and AD risk (red line represents the MR estimate). Each point is a variant with significant *MAF* expression quantitative trait locus (eQTL; $p < 5e{-}3$) and not in linkage disequilibrium ($R^2 < 0.001$).
(K) Cartoon describing the human snRNA-seq dataset from Fujita et al.[62] (whole-genome sequencing [WGS]).
(L) snRNA-seq of human brain macrophages colored by cluster assignment (top). Violin plots showing *MAF* expression in MG or CD163$^+$ BAMs from individuals with each genotype. The numbers above the violin plots represent the percent change in mean *MAF* expression compared with the TT genotype.
See also Figure S7.

Please cite this article in press as: Brioschi et al., Brain perivascular macrophages regulate endothelial cell function via a cMAF-dependent transcriptional program in mouse and human, Cell (2026), https://doi.org/10.1016/j.cell.2026.07.043

We provide several lines of evidence supporting the protective role of cMAF in AD. A recent GWAS identified a SNP (rs450674) near the *MAF* 3′ linked to reduced AD risk.[60] We show that this SNP lies within a transcriptionally active regulatory region in perivascular macrophages and is associated with increased cMAF and IGF1 expression. Moreover, cMAF and IGF1 are upregulated in perivascular macrophages in AD and positively correlate with amyloid pathology. Importantly, this response is blunted in *APOE4* carriers, who are more vulnerable to CAA and vascular damage.[59] Consistently, perivascular macrophages in *APOE4* knockin mice downregulate angiocrine molecules, including IGF1, indicating that the *APOE* genotype directly affects their functions. Indeed, a recent report shows that perivascular macrophages promote vascular damage in the presence of *APOE4*.[82] Vascular cells are profoundly affected in AD,[52,83] yet how this contributes to neurodegeneration remains an open question.[84] It also remains unclear what drives cMAF upregulation during disease. One candidate molecule is the blood-derived complement C3, which induces cMAF in macrophages,[85] and hence could link BBB leakage and the protective cMAF response. Notably, cMAF mutations cause the Down-like neurodevelopmental disorder *Aymé-Gripp* syndrome,[86] raising the question of whether cerebrovascular impairment contributes to this condition.

In conclusion, our findings identify cMAF as a central regulator of a conserved perivascular macrophage program that safeguards CNS vascular function and fluid dynamics. Thus, the cMAF pathway emerges as a potential therapeutic target to enhance neurovascular resilience in AD.

Limitations of the study

Because cMAF deletion induces detectable changes in MG, their contribution to the observed vascular phenotype cannot be formally excluded. Ultrastructural analysis of the perivascular compartment is needed to resolve structural alterations within the neurovascular unit. Our cerebrovascular analyses are limited to the hypercapnia paradigm; whether cMAF influences responses to other stimuli remains to be tested. Finally, the impact of the *rs450674* and *APOE* variants on BAMs versus MG, including potential sex-dependent effects, requires further investigation.

RESOURCE AVAILABILITY

Lead contact

Requests for further information and resources should be directed to and will be fulfilled by the lead contact, Marco Colonna (mcolonna@mgh.harvard.edu).

Materials availability

The mouse lines used in this study are publicly available through The Jackson Laboratory, with the exception of the $Maf^{flox/flox}$ strain, which was provided by Dr. Jun Yan (University of Louisville School of Medicine) under a materials transfer agreement (MTA).

Data and code availability

Sequencing data generated in this study have been deposited at the Gene Expression Omnibus (GEO) under accession number GEO: GSE298940 and are publicly available as of the date of publication. Key scripts used for data analyses can be found at https://github.com/juliabelk/brioschi_2023.

ACKNOWLEDGMENTS

This study is supported by the following grants: NIH R01-AI158579, R01-AG051485, R01-AG081631, P01-AG078106, and R21-AG085133 (M. Colonna); Carol and Gene Ludwig Family Foundation (M. Colonna); the Fred and Ginger Haberle Charitable Fund at the East Texas Communities Foundation (M. Colonna); The Alzheimer Association AARG-24-1292984 (S.B.) and AARF-23-1026231 (S.E.S.); HHMI Hanna Gray Fellowship (J.A.B.); NIH T32-HL007081 (D.D.L.); European Research Council ERC-CoG 101088887 and Italian Telethon Foundation SR-Tiget grant award F04 (R.O.); NIH R01-CA278941 (J.Y.); AIRC IG-23179 (W.V.); and Swiss National Science Foundation SNSF 211033 and 234543 (P.F.R.). We thank E. Lantelme (Flow Cytometry Core), W. Beatty (Imaging Core), and R. Mellor and A. Burkhalter (Histology and Innovation Service Center) at Washington University in St. Louis for technical assistance. We thank R. Cho (Cell Signaling), as well as R. Roth and K. Choi (Washington University in St. Louis) for sharing protocols and materials, and X. Hu (University of Louisville) for sharing the $Maf^{flox/flox}$ mice. Sequencing operations were performed at the McDonnell Genome Institute (Washington University in St. Louis). Illustrations were generated in BioRender.com.

AUTHOR CONTRIBUTIONS

Conceptualization: S.B. and M. Colonna; experiments/analyses: S.B., J.A.B., S.E.S., Y.W., Zhuoying Wang, Z.F., L.v.O., J.L.E., R.S., J.W., S.D., M.G., F.LT., A.J.E., K.M.N., J.S., D.D.L., M.B., A.J.F., Y.C., Zuoxu Wang, S.P., P.F.R., A.U.A., H.Q.L., I.S., M. Cella, and A.T.N.; resources/methodologies: S.G., C.M.H., J.P., J.Y., H.Y.C., G.J.R., W.V., M.M., R.O., D.G., C.C., S.H., and J.K.; manuscript writing/editing: S.B., J.A.B., S.E.S., R.O., and M. Colonna; funding: M. Colonna. All authors approved the study before submission.

DECLARATION OF INTERESTS

M. Colonna is a member of the scientific advisory boards of Vigil, BioClec, Cartesian, and Halyard; receives research support from Vigil and Ono Pharmaceutical; consults for Cell Signaling Technology; and has patents pending on TREM2 and LILRB4. J.K. is a co-founder of Rho Bio and has patents and provisional applications related to the findings described here.

STAR★METHODS

Detailed methods are provided in the online version of this paper and include the following:

- KEY RESOURCES TABLE
- EXPERIMENTAL MODEL AND STUDY PARTICIPANT DETAILS
  - Mouse models
  - Human brain samples
  - Primary cell cultures (bone marrow derived macrophages, BMDM)
  - Primary cell cultures (endothelial cells)
- METHOD DETAILS
  - Sample preparation for flow cytometry and sorting
  - Cerebrospinal fluid circulation and glymphatic flow
  - NHS-Biotin injection for BBB permeability analysis
  - Immunofluorescence staining
  - Confocal microscope
  - Brain tissue clearing and imaging
  - Immunohistochemistry and immunofluorescence staining of healthy human brains
  - Immunofluorescence staining of AD brains
  - RNA-scope HiPlex Assay
  - Multi-parametric photoacoustic microscopy
  - Parabiosis
  - Western blot of brain endothelial cells
  - CRISPR-Cas9 gene editing in BMDMs
  - Real-Time quantitative PCR
  - Bulk RNA-seq of BMDMs with CRISPR-Cas9 gene editing (library preparation)
  - Bulk RNA-seq of primary endothelial cells (library preparation)

- 10x Genomics single-cell ATAC sequencing (library preparation)
- 10x Genomics single-cell RNA sequencing of brain macrophages (library preparation)
- 10x Genomics single-cell RNA sequencing of brain vascular cells (library preparation)
- c-MAF ChIP-seq in BMDMs (library preparation)
- c-MAF CUT&RUN in microglia and BAMs (library preparation)

- QUANTIFICATION AND STATISTICAL ANALYSIS
  - Bulk RNA-seq of BMDMs (analysis)
  - Bulk RNA-seq of primary endothelial cells (analysis)
  - 10x Genomics single-cell ATAC sequencing (analysis)
  - Mouse single-cell RNA sequencing data (analysis)
  - c-MAF and SMAD4 ChIP-seq (analysis)
  - cMAF CUT&RUN in microglia and BAMs (analysis)
  - Human single-nuclei RNA sequencing data (analysis)
  - Genetic analysis of the *MAF* polymorphism
  - Statistics

SUPPLEMENTAL INFORMATION

Supplemental information can be found online at https://doi.org/10.1016/j.cell.2026.07.043.

Received: September 10, 2025
Revised: June 18, 2026
Accepted: July 29, 2026

REFERENCES

1. Wake, H., Moorhouse, A.J., Jinno, S., Kohsaka, S., and Nabekura, J. (2009). Resting microglia directly monitor the functional state of synapses in vivo and determine the fate of ischemic terminals. J. Neurosci. *29*, 3974–3980. https://doi.org/10.1523/jneurosci.4363-08.2009.
2. Paolicelli, R.C., Bolasco, G., Pagani, F., Maggi, L., Scianni, M., Panzanelli, P., Giustetto, M., Ferreira, T.A., Guiducci, E., Dumas, L., et al. (2011). Synaptic pruning by microglia is necessary for normal brain development. Science *333*, 1456–1458. https://doi.org/10.1126/science.1202529.
3. Schafer, D.P., Lehrman, E.K., Kautzman, A.G., Koyama, R., Mardinly, A.R., Yamasaki, R., Ransohoff, R.M., Greenberg, M.E., Barres, B.A., and Stevens, B. (2012). Microglia sculpt postnatal neural circuits in an activity and complement-dependent manner. Neuron *74*, 691–705. https://doi.org/10.1016/j.neuron.2012.03.026.
4. Zhan, Y., Paolicelli, R.C., Sforazzini, F., Weinhard, L., Bolasco, G., Pagani, F., Vyssotski, A.L., Bifone, A., Gozzi, A., Ragozzino, D., et al. (2014). Deficient neuron-microglia signaling results in impaired functional brain connectivity and social behavior. Nat. Neurosci. *17*, 400–406. https://doi.org/10.1038/nn.3641.
5. Squarzoni, P., Oller, G., Hoeffel, G., Pont-Lezica, L., Rostaing, P., Low, D., Bessis, A., Ginhoux, F., and Garel, S. (2014). Microglia modulate wiring of the embryonic forebrain. Cell Rep. *8*, 1271–1279. https://doi.org/10.1016/j.celrep.2014.07.042.
6. Cserép, C., Pósfai, B., Lénárt, N., Fekete, R., László, Z.I., Lele, Z., Orsolits, B., Molnár, G., Heindl, S., Schwarcz, A.D., et al. (2020). Microglia monitor and protect neuronal function through specialized somatic purinergic junctions. Science *367*, 528–537. https://doi.org/10.1126/science.aax6752.
7. Badimon, A., Strasburger, H.J., Ayata, P., Chen, X., Nair, A., Ikegami, A., Hwang, P., Chan, A.T., Graves, S.M., Uweru, J.O., et al. (2020). Negative feedback control of neuronal activity by microglia. Nature *586*, 417–423. https://doi.org/10.1038/s41586-020-2777-8.
8. McNamara, N.B., Munro, D.A.D., Bestard-Cuche, N., Uyeda, A., Bogie, J.F.J., Hoffmann, A., Holloway, R.K., Molina-Gonzalez, I., Askew, K.E., Mitchell, S., et al. (2023). Microglia regulate central nervous system myelin growth and integrity. Nature *613*, 120–129. https://doi.org/10.1038/s41586-022-05534-y.
9. Escoubas, C.C., Dorman, L.C., Nguyen, P.T., Lagares-Linares, C., Nakajo, H., Anderson, S.R., Barron, J.J., Wade, S.D., Cuevas, B., Vainchtein, I.D., et al. (2024). Type-I-interferon-responsive microglia shape cortical development and behavior. Cell *187*, 1936–1954.e24. https://doi.org/10.1016/j.cell.2024.02.020.
10. Lawrence, A.R., Canzi, A., Bridlance, C., Olivié, N., Lansonneur, C., Catale, C., Pizzamiglio, L., Kloeckner, B., Silvin, A., Munro, D.A.D., et al. (2024). Microglia maintain structural integrity during fetal brain morphogenesis. Cell *187*, 962–980.e19. https://doi.org/10.1016/j.cell.2024.01.012.
11. Mrdjen, D., Pavlovic, A., Hartmann, F.J., Schreiner, B., Utz, S.G., Leung, B.P., Lelios, I., Heppner, F.L., Kipnis, J., Merkler, D., et al. (2018). High-Dimensional Single-Cell Mapping of Central Nervous System Immune Cells Reveals Distinct Myeloid Subsets in Health, Aging, and Disease. Immunity *48*, 380–395.e6. https://doi.org/10.1016/j.immuni.2018.01.011.
12. Jordão, M.J.C., Sankowski, R., Brendecke, S.M., Sagar, L., Locatelli, G., Tai, Y.H., Tay, T.L., Schramm, E., Armbruster, S., Hagemeyer, N., et al. (2019). Single-cell profiling identifies myeloid cell subsets with distinct fates during neuroinflammation. Science *363*, eaat7554. https://doi.org/10.1126/science.aat7554.
13. Penati, S., Brioschi, S., Cai, Z., Han, C.Z., and Colonna, M. (2025). Mechanisms and environmental factors shaping the ecosystem of brain macrophages. Front. Immunol. *16*, 1539988. https://doi.org/10.3389/fimmu.2025.1539988.
14. De Vlaminck, K., Van Hove, H., Kancheva, D., Scheyltjens, I., Pombo Antunes, A.R., Bastos, J., Vara-Perez, M., Ali, L., Mampay, M., Deneyer, L., et al. (2022). Differential plasticity and fate of brain-resident and recruited macrophages during the onset and resolution of neuroinflammation. Immunity *55*, 2085–2102.e9. https://doi.org/10.1016/j.immuni.2022.09.005.
15. Rebejac, J., Eme-Scolan, E., Arnaud Paroutaud, L., Kharbouche, S., Teleman, M., Spinelli, L., Gallo, E., Roussel-Queval, A., Zarubica, A., Sansoni, A., et al. (2022). Meningeal macrophages protect against viral neuroinfection. Immunity *55*, 2103–2117.e10. https://doi.org/10.1016/j.immuni.2022.10.005.
16. Xu, H., Lotfy, P., Gelb, S., Pragana, A., Hehnly, C., Byer, L.I.J., Shipley, F.B., Zawadzki, M.E., Cui, J., Deng, L., et al. (2024). The choroid plexus synergizes with immune cells during neuroinflammation. Cell *187*, 4946–4963.e17. https://doi.org/10.1016/j.cell.2024.07.002.
17. Faraco, G., Sugiyama, Y., Lane, D., Garcia-Bonilla, L., Chang, H., Santisteban, M.M., Racchumi, G., Murphy, M., Van Rooijen, N., Anrather, J., et al. (2016). Perivascular macrophages mediate the neurovascular and cognitive dysfunction associated with hypertension. J. Clin. Investig. *126*, 4674–4689. https://doi.org/10.1172/JCI86950.
18. Santisteban, M.M., Schaeffer, S., Anfray, A., Faraco, G., Brea, D., Wang, G., Sobanko, M.J., Sciortino, R., Racchumi, G., Waisman, A., et al. (2024). Meningeal interleukin-17-producing T cells mediate cognitive impairment in a mouse model of salt-sensitive hypertension. Nat. Neurosci. *27*, 63–77. https://doi.org/10.1038/s41593-023-01497-z.
19. Park, L., Uekawa, K., Garcia-Bonilla, L., Koizumi, K., Murphy, M., Pistik, R., Younkin, L., Younkin, S., Zhou, P., Carlson, G., et al. (2017). Brain Perivascular Macrophages Initiate the Neurovascular Dysfunction of Alzheimer Aβ Peptides. Circ. Res. *121*, 258–269. https://doi.org/10.1161/CIRCRESAHA.117.311054.
20. Taylor, X., Noristani, H.N., Fitzgerald, G.J., Oluoch, H., Babb, N., McGathey, T., Carter, L., Hole, J.T., Lacor, P.N., DeMattos, R.B., et al. (2024). Amyloid-β (Aβ) immunotherapy induced microhemorrhages are linked to vascular inflammation and cerebrovascular damage in a mouse model of Alzheimer's disease. Mol. Neurodegener. *19*, 77. https://doi.org/10.1186/s13024-024-00758-0.
21. Taylor, X., Clark, I.M., Fitzgerald, G.J., Oluoch, H., Hole, J.T., DeMattos, R.B., Wang, Y., and Pan, F. (2023). Amyloid-β (Aβ) immunotherapy induced microhemorrhages are associated with activated perivascular

macrophages and peripheral monocyte recruitment in Alzheimer's disease mice. Mol. Neurodegener. *18*, 59. https://doi.org/10.1186/s13024-023-00649-w.

22. Brioschi, S., Belk, J.A., Peng, V., Molgora, M., Rodrigues, P.F., Nguyen, K.M., Wang, S., Du, S., Wang, W.-L., Grajales-Reyes, G.E., et al. (2023). A Cre-deleter specific for embryo-derived brain macrophages reveals distinct features of microglia and border macrophages. Immunity *56*, 1027–1045.e8. https://doi.org/10.1016/j.immuni.2023.01.028.

23. Van Hove, H., Martens, L., Scheyltjens, I., De Vlaminck, K., Pombo Antunes, A.R., De Prijck, S., Vandamme, N., De Schepper, S., Van Isterdael, G., Scott, C.L., et al. (2019). A single-cell atlas of mouse brain macrophages reveals unique transcriptional identities shaped by ontogeny and tissue environment. Nat. Neurosci. *22*, 1021–1035. https://doi.org/10.1038/s41593-019-0393-4.

24. Dick, S.A., Wong, A., Hamidzada, H., Nejat, S., Nechanitzky, R., Vohra, S., Mueller, B., Zaman, R., Kantores, C., Aronoff, L., et al. (2022). Three tissue resident macrophage subsets coexist across organs with conserved origins and life cycles. Sci. Immunol. *7*, eabf7777. https://doi.org/10.1126/sciimmunol.abf7777.

25. Silvin, A., Uderhardt, S., Piot, C., Da Mesquita, S., Yang, K., Geirsdottir, L., Mulder, K., Eyal, D., Liu, Z., Bridlance, C., et al. (2022). Dual ontogeny of disease-associated microglia and disease inflammatory macrophages in aging and neurodegeneration. Immunity *55*, 1448–1465.e6. https://doi.org/10.1016/j.immuni.2022.07.004.

26. Amann, L., Fell, A., Monaco, G., Sankowski, R., Wu, H.Z.Q., Jordão, M.J.C., Borst, K., Fliegauf, M., Masuda, T., Ardura-Fabregat, A., et al. (2024). Extrasinusoidal macrophages are a distinct subset of immunologically active dural macrophages. Sci. Immunol. *9*, eadh1129. https://doi.org/10.1126/sciimmunol.adh1129.

27. Goldmann, T., Wieghofer, P., Jordão, M.J.C., Prutek, F., Hagemeyer, N., Frenzel, K., Amann, L., Staszewski, O., Kierdorf, K., Krueger, M., et al. (2016). Origin, fate and dynamics of macrophages at central nervous system interfaces. Nat. Immunol. *17*, 797–805. https://doi.org/10.1038/ni.3423.

28. Utz, S.G., See, P., Mildenberger, W., Thion, M.S., Silvin, A., Lutz, M., Ingelfinger, F., Rayan, N.A., Lelios, I., Buttgereit, A., et al. (2020). Early Fate Defines Microglia and Non-parenchymal Brain Macrophage Development. Cell *181*, 557–573.e18. https://doi.org/10.1016/j.cell.2020.03.021.

29. Masuda, T., Amann, L., Monaco, G., Sankowski, R., Staszewski, O., Krueger, M., Del Gaudio, F., He, L., Paterson, N., Nent, E., et al. (2022). Specification of CNS macrophage subsets occurs postnatally in defined niches. Nature *604*, 740–748. https://doi.org/10.1038/s41586-022-04596-2.

30. Bastos, J., O'Brien, C., Vara-Pérez, M., Mampay, M., van Olst, L., Barry-Carroll, L., Kancheva, D., Leduc, S., Lievens, A.L., Ali, L., et al. (2025). Monocytes can efficiently replace all brain macrophages and fetal liver monocytes can generate bona fide SALL1+ microglia. Immunity *58*, 1269–1288.e12. https://doi.org/10.1016/j.immuni.2025.04.006.

31. Du, S., Nguyen, K.M., Ulezko Antonova, A., Fachi, J.L., Rodrigues, P.F., Verdiani, A., Molgora, M., Smirnov, I., Herz, J., Mamuladze, T., et al. (2026). Diversity and immune dynamics of choroid plexus macrophages are shaped by distinct developmental origins. Nat. Neurosci. *29*, 717–731. https://doi.org/10.1038/s41593-025-02158-z.

32. Fliegauf, M., Levard, D., Cardamone, F., Frosch, M., Kuhn, S., Sankowski, R., Provinciali, M., Dumas, A.A., Dalmau Gasull, A., Aktories, P., et al. (2026). Distinct origins and niches determine the cellular responsiveness of CNS macrophages after repopulation. Nat. Immunol. *27*, 961–974. https://doi.org/10.1038/s41590-026-02457-y.

33. Butovsky, O., Jedrychowski, M.P., Moore, C.S., Cialic, R., Lanser, A.J., Gabriely, G., Koeglsperger, T., Dake, B., Wu, P.M., Doykan, C.E., et al. (2014). Identification of a unique TGF-β-dependent molecular and functional signature in microglia. Nat. Neurosci. *17*, 131–143. https://doi.org/10.1038/nn.3599.

34. Fixsen, B.R., Han, C.Z., Zhou, Y., Spann, N.J., Saisan, P., Shen, Z., Balak, C., Sakai, M., Cobo, I., Holtman, I.R., et al. (2023). SALL1 enforces microglia-specific DNA binding and function of SMADs to establish microglia identity. Nat. Immunol. *24*, 1188–1199. https://doi.org/10.1038/s41590-023-01528-8.

35. Brioschi, S., Han, C.Z., and Colonna, M. (2025). Drivers and shapers of macrophages specification in the developing brain. Curr. Opin. Immunol. *94*, 102558. https://doi.org/10.1016/J.COI.2025.102558.

36. Serrano-Pozo, A., Das, S., and Hyman, B.T. (2021). APOE and Alzheimer's disease: advances in genetics, pathophysiology, and therapeutic approaches. Lancet Neurol. *20*, 68–80. https://doi.org/10.1016/S1474-4422(20)30412-9.

37. Tanzi, R.E. (2012). The genetics of Alzheimer disease. Cold Spring Harb. Perspect. Med. *2*, a006296. https://doi.org/10.1101/cshperspect.a006296.

38. Saeki, K., Pan, R., Lee, E., Kurotaki, D., and Ozato, K. (2024). IRF8 defines the epigenetic landscape in postnatal microglia, thereby directing their transcriptome programs. Nat. Immunol. *25*, 1928–1942. https://doi.org/10.1038/s41590-024-01962-2.

39. Yamasaki, A., Imanishi, I., Tanaka, K., Ohkawa, Y., Tsuda, M., and Masuda, T. (2024). IRF8 and MAFB drive distinct transcriptional machineries in different resident macrophages of the central nervous system. Commun. Biol. *7*, 896. https://doi.org/10.1038/s42003-024-06607-6.

40. Aziz, A., Soucie, E., Sarrazin, S., and Sieweke, M.H. (2009). MafB/c-Maf deficiency enables self-renewal of differentiated functional macrophages. Science *326*, 867–871. https://doi.org/10.1126/science.1176056.

41. Soucie, E.L., Weng, Z., Geirsdóttir, L., Molawi, K., Maurizio, J., Fenouil, R., Mossadegh-Keller, N., Gimenez, G., Vanhille, L., Beniazza, M., et al. (2016). Lineage-specific enhancers activate self-renewal genes in macrophages and embryonic stem cells. Science *351*, aad5510. https://doi.org/10.1126/science.aad5510.

42. Liu, M., Tong, Z., Ding, C., Luo, F., Wu, S., Wu, C., Albeituni, S., He, L., Hu, X., Tieri, D., et al. (2020). Transcription factor c-Maf is a checkpoint that programs macrophages in lung cancer. J. Clin. Invest. *130*, 2081–2096. https://doi.org/10.1172/JCI131335.

43. Lee, D.D., Telfer, K.A., Davis, D.L., Smyth, L.C.D., Ravindran, R., Czepielewski, R.S., Huckstep, C.G., Du, S., Kurashima, K., Jain, A.K., et al. (2025). ADAPT-3D:accelerated deep adaptable processing of tissue for 3-dimensional fluorescence tissue imaging for research and clinical settings. Sci. Rep. *15*, 31841. https://doi.org/10.1038/s41598-025-16766-z.

44. Buttgereit, A., Lelios, I., Yu, X., Vrohlings, M., Krakoski, N.R., Gautier, E.L., Nishinakamura, R., Becher, B., and Greter, M. (2016). Sall1 is a transcriptional regulator defining microglia identity and function. Nat. Immunol. *17*, 1397–1406. https://doi.org/10.1038/ni.3585.

45. Drieu, A., Du, S., Storck, S.E., Rustenhoven, J., Papadopoulos, Z., Dykstra, T., Zhong, F., Kim, K., Blackburn, S., Mamuladze, T., et al. (2022). Parenchymal border macrophages regulate the flow dynamics of the cerebrospinal fluid. Nature *611*, 585–593. https://doi.org/10.1038/s41586-022-05397-3.

46. McKinsey, G.L., Lizama, C.O., Keown-Lang, A.E., Niu, A., Santander, N., Larpthaveesarp, A., Chee, E., Gonzalez, F.F., and Arnold, T.D. (2020). A new genetic strategy for targeting microglia in development and disease. eLife *9*, e54590. https://doi.org/10.7554/eLife.54590.

47. Santisteban, M.M., Ahn, S.J., Lane, D., Faraco, G., Garcia-Bonilla, L., Racchumi, G., Poon, C., Schaeffer, S., Segarra, S.G., Körbelin, J., et al. (2020). Endothelium-Macrophage Crosstalk Mediates Blood-Brain Barrier Dysfunction in Hypertension. Hypertension *76*, 795–807. https://doi.org/10.1161/hypertensionaha.120.15581.

48. Iliff, J.J., Wang, M., Zeppenfeld, D.M., Venkataraman, A., Plog, B.A., Liao, Y., Deane, R., and Nedergaard, M. (2013). Cerebral arterial pulsation drives paravascular CSF-Interstitial fluid exchange in the murine brain. J. Neurosci. *33*, 18190–18199. https://doi.org/10.1523/jneurosci.1592-13.2013.

49. Mestre, H., Tithof, J., Du, T., Song, W., Peng, W., Sweeney, A.M., Olveda, G., Thomas, J.H., Nedergaard, M., and Kelley, D.H. (2018). Flow of cerebrospinal fluid is driven by arterial pulsations and is reduced in hypertension. Nat. Commun. *9*, 4878. https://doi.org/10.1038/s41467-018-07318-3.

50. Zhou, Y., Song, W.M., Andhey, P.S., Swain, A., Levy, T., Miller, K.R., Poliani, P.L., Cominelli, M., Grover, S., Gilfillan, S., et al. (2020). Human and mouse single-nucleus transcriptomics reveal TREM2-dependent and TREM2-independent cellular responses in Alzheimer's disease. Nat. Med. *26*, 131–142. https://doi.org/10.1038/s41591-019-0695-9.

51. Zhou, Y., Tada, M., Cai, Z., Andhey, P.S., Swain, A., Miller, K.R., Gilfillan, S., Artyomov, M.N., Takao, M., Kakita, A., et al. (2023). Human early-onset dementia caused by DAP12 deficiency reveals a unique signature of dysregulated microglia. Nat. Immunol. *24*, 545–557. https://doi.org/10.1038/s41590-022-01403-y.

52. Yang, A.C., Vest, R.T., Kern, F., Lee, D.P., Agam, M., Maat, C.A., Losada, P.M., Chen, M.B., Schaum, N., Khoury, N., et al. (2022). A human brain vascular atlas reveals diverse mediators of Alzheimer's risk. Nature *603*, 885–892. https://doi.org/10.1038/s41586-021-04369-3.

53. Siletti, K., Hodge, R., Mossi Albiach, A., Lee, K.W., Ding, S.L., Hu, L., Lönnerberg, P., Bakken, T., Casper, T., Clark, M., et al. (2023). Transcriptomic diversity of cell types across the adult human brain. Science *382*, eadd7046. https://doi.org/10.1126/science.add7046.

54. Winkler, E.A., Kim, C.N., Ross, J.M., Garcia, J.H., Gil, E., Oh, I., Chen, L.Q., Wu, D., Catapano, J.S., Raygor, K., et al. (2022). A single-cell atlas of the normal and malformed human brain vasculature. Science *375*, eabi7377. https://doi.org/10.1126/science.abi7377.

55. Wälchli, T., Ghobrial, M., Schwab, M., Takada, S., Zhong, H., Suntharalingham, S., Vetiska, S., Gonzalez, D.R., Wu, R., Rehrauer, H., et al. (2024). Single-cell atlas of the human brain vasculature across development, adulthood and disease. Nature *632*, 603–613. https://doi.org/10.1038/s41586-024-07493-y.

56. Rosenzweig, N., Kleemann, K.L., Rust, T., Carpenter, M., Grucci, M., Aronchik, M., Brouwer, N., Valenbreder, I., Cooper-Hohn, J., Iyer, M., et al. (2024). Sex-dependent APOE4 neutrophil–microglia interactions drive cognitive impairment in Alzheimer's disease. Nat. Med. *30*, 2990–3003. https://doi.org/10.1038/s41591-024-03122-3.

57. Semerena, E., Nencioni, A., and Masternak, K. (2023). Extracellular nicotinamide phosphoribosyltransferase: role in disease pathophysiology and as a biomarker. Front. Immunol. *14*, 1268756. https://doi.org/10.3389/fimmu.2023.1268756.

58. Reas, E.T., Solders, S.K., Tsiknia, A., Triebswetter, C., Shen, Q., Rivera, C.S., Andrews, M.J., Alderson-Myers, A., and Brewer, J.B. (2024). APOE ε4-related blood–brain barrier breakdown is associated with microstructural abnormalities. Alzheimers Dement. *20*, 8615–8624. https://doi.org/10.1002/alz.14302.

59. Montagne, A., Nation, D.A., Sagare, A.P., Barisano, G., Sweeney, M.D., Chakhoyan, A., Pachicano, M., Joe, E., Nelson, A.R., D'Orazio, L.M., et al. (2020). APOE4 leads to blood–brain barrier dysfunction predicting cognitive decline. Nature *581*, 71–76. https://doi.org/10.1038/s41586-020-2247-3.

60. Bellenguez, C., Küçükali, F., Jansen, I.E., Kleineidam, L., Moreno-Grau, S., Amin, N., Naj, A.C., Campos-Martin, R., Grenier-Boley, B., Andrade, V., et al. (2022). New insights into the genetic etiology of Alzheimer's disease and related dementias. Nat. Genet. *54*, 412–436. https://doi.org/10.1038/s41588-022-01024-z.

61. Dugan, A.J., Nelson, P.T., Katsumata, Y., Shade, L.M.P., Teylan, M.A., Boehme, K.L., Mukherjee, S., Kauwe, J.S.K., Hohman, T.J., Schneider, J.A., et al. (2022). Association between WWOX/MAF variants and dementia-related neuropathologic endophenotypes. Neurobiol. Aging *111*, 95–106. https://doi.org/10.1016/j.neurobiolaging.2021.10.011.

62. Fujita, M., Gao, Z., Zeng, L., McCabe, C., White, C.C., Ng, B., Green, G.S., Rozenblatt-Rosen, O., Phillips, D., Amir-Zilberstein, L., et al. (2024). Cell subtype-specific effects of genetic variation in the Alzheimer's disease brain. Nat. Genet. *56*, 605–614. https://doi.org/10.1038/s41588-024-01685-y.

63. Nott, A., Holtman, I.R., Coufal, N.G., Schlachetzki, J.C.M., Yu, M., Hu, R., Han, C.Z., Pena, M., Xiao, J., Wu, Y., et al. (2019). Brain cell type-specific enhancer-promoter interactome maps and disease-risk association. Science *366*, 1134–1139. https://doi.org/10.1126/science.aay0793.

64. Reid, M.M., Menon, S., Liu, H., Zhou, H., Hu, Z., Frerich, S., Ding, B., Oveisgharan, S., Zhang, Z., Nelson, S., et al. (2025). Human brain vascular multi-omics elucidates disease-risk associations. Neuron *113*, 3143–3161.e5. https://doi.org/10.1016/j.neuron.2025.07.001.

65. Van Hove, H., Glück, C., Mildenberger, W., Petrova, E., Maheshwari, U., Häne, P., Kreiner, V., Bijnen, M., Mussak, C., Utz, S.G., et al. (2025). Interleukin-34-dependent perivascular macrophages promote vascular function in the brain. Immunity *58*, 1289–1305.e8. https://doi.org/10.1016/j.immuni.2025.04.003.

66. Seo, S.H., Hwang, S.Y., Hwang, S., Han, S., Park, H., Lee, Y.S., Rho, S.B., and Kwon, Y. (2022). Hypoxia-induced ELF3 promotes tumor angiogenesis through IGF1/IGF1R. EMBO Rep. *23*, e52977. https://doi.org/10.15252/embr.202152977.

67. Hayes, C.A., Valcarcel-Ares, M.N., and Ashpole, N.M. (2021). Preclinical and clinical evidence of IGF-1 as a prognostic marker and acute intervention with ischemic stroke. J. Cereb. Blood Flow Metab. *41*, 2475–2491. https://doi.org/10.1177/0271678X211000894.

68. Tarantini, S., Nyúl-Tóth, Á., Yabluchanskiy, A., Csipo, T., Mukli, P., Balasubramanian, P., Ungvari, A., Toth, P., Benyo, Z., Sonntag, W.E., et al. (2021). Endothelial deficiency of insulin-like growth factor-1 receptor (IGF1R) impairs neurovascular coupling responses in mice, mimicking aspects of the brain aging phenotype. GeroScience *43*, 2387–2394. https://doi.org/10.1007/s11357-021-00405-2.

69. Miller, L.R., Bickel, M.A., Vance, M.L., Vaden, H., Nagykaldi, D., Nyul-Toth, A., Bullen, E.C., Gautam, T., Tarantini, S., Yabluchanskiy, A., et al. (2024). Vascular smooth muscle cell-specific Igf1r deficiency exacerbates the development of hypertension-induced cerebral microhemorrhages and gait defects. GeroScience *46*, 3481–3501. https://doi.org/10.1007/s11357-024-01090-7.

70. Zaman, R., Hamidzada, H., Kantores, C., Wong, A., Dick, S.A., Wang, Y., Momen, A., Aronoff, L., Lin, J., Razani, B., et al. (2021). Selective loss of resident macrophage-derived insulin-like growth factor-1 abolishes adaptive cardiac growth to stress. Immunity *54*, 2057–2071.e6. https://doi.org/10.1016/j.immuni.2021.07.006.

71. Chen, J., Du, S., Cheng, W., Amrute, J.M., Kim, M.W., Ohara, R.A., Han, J., Jo, S., Kim, L., Wang, Z., et al. (2026). Transcription factor Maf promotes expression of repressor Zeb2 to drive microglia development in primitive hematopoiesis. Immunity *59*, 48–59.e5. https://doi.org/10.1016/j.immuni.2025.11.022.

72. Chakarov, S., Lim, H.Y., Tan, L., Lim, S.Y., See, P., Lum, J., Zhang, X.M., Foo, S., Nakamizo, S., Duan, K., et al. (2019). Two distinct interstitial macrophage populations coexist across tissues in specific subtissular niches. Science *363*, eaau0964. https://doi.org/10.1126/science.aau0964.

73. Lim, H.Y., Lim, S.Y., Tan, C.K., Thiam, C.H., Goh, C.C., Carbajo, D., Chew, S.H.S., See, P., Chakarov, S., Wang, X.N., et al. (2018). Hyaluronan Receptor LYVE-1-Expressing Macrophages Maintain Arterial Tone through Hyaluronan-Mediated Regulation of Smooth Muscle Cell Collagen. Immunity *49*, 326–341.e7. https://doi.org/10.1016/j.immuni.2018.06.008.

74. Viola, M.F., Chavero-Pieres, M., Modave, E., Delfini, M., Stakenborg, N., Estévez, M.C., Fabre, N., Appeltans, I., Martens, T., Vandereyken, K., et al. (2023). Dedicated macrophages organize and maintain the enteric nervous system. Nature *618*, 818–826. https://doi.org/10.1038/s41586-023-06200-7.

75. Siret, C., van Lessen, M., Bavais, J., Jeong, H.W., Reddy Samawar, S.K., Kapupara, K., Wang, S., Simic, M., de Fabritus, L., Tchoghandjian, A., et al. (2022). Deciphering the heterogeneity of the Lyve1+ perivascular

macrophages in the mouse brain. Nat. Commun. *13*, 7366. https://doi.org/10.1038/s41467-022-35166-9.

76. Kalucka, J., de Rooij, L.P.M.H., Goveia, J., Rohlenova, K., Dumas, S.J., Meta, E., Conchinha, N.V., Taverna, F., Teuwen, L.A., Veys, K., et al. (2020). Single-Cell Transcriptome Atlas of Murine Endothelial Cells. Cell *180*, 764–779.e20. https://doi.org/10.1016/j.cell.2020.01.015.

77. Moura Silva, H.M., Kitoko, J.Z., Queiroz, C.P., Kroehling, L., Matheis, F., Yang, K.L., Reis, B.S., Ren-Fielding, C., Littman, D.R., Bozza, M.T., et al. (2021). c-MAF–dependent perivascular macrophages regulate diet-induced metabolic syndrome. Sci. Immunol. *6*, eabg7506. https://doi.org/10.1126/sciimmunol.abg7506.

78. Happonen, K.E., Burrola, P.G., and Lemke, G. (2023). Regulation of brain endothelial cell physiology by the TAM receptor tyrosine kinase Mer. Commun. Biol. *6*, 916. https://doi.org/10.1038/s42003-023-05287-y.

79. Su, E.J., Fredriksson, L., Geyer, M., Folestad, E., Cale, J., Andrae, J., Gao, Y., Pietras, K., Mann, K., Yepes, M., et al. (2008). Activation of PDGF-CC by tissue plasminogen activator impairs blood-brain barrier integrity during ischemic stroke. Nat. Med. *14*, 731–737. https://doi.org/10.1038/nm1787.

80. Fredriksson, L., Nilsson, I., Su, E.J., Andrae, J., Ding, H., Betsholtz, C., Eriksson, U., and Lawrence, D.A. (2012). Platelet-derived growth factor C deficiency in C57BL/6 mice leads to abnormal cerebral vascularization, loss of neuroependymal integrity, and ventricular abnormalities. Am. J. Pathol. *180*, 1136–1144. https://doi.org/10.1016/j.ajpath.2011.12.006.

81. Sankowski, R., Böttcher, C., Masuda, T., Geirsdottir, L., Sagar, S., Sindram, E., Seredenina, T., Muhs, A., Scheiwe, C., Shah, M.J., et al. (2019). Mapping microglia states in the human brain through the integration of high-dimensional techniques. Nat. Neurosci. *22*, 2098–2110. https://doi.org/10.1038/s41593-019-0532-y.

82. Anfray, A., Schaeffer, S., Hattori, Y., Santisteban, M.M., Casey, N., Wang, G., Strickland, M., Zhou, P., Holtzman, D.M., Anrather, J., et al. (2024). A cell-autonomous role for border-associated macrophages in ApoE4 neurovascular dysfunction and susceptibility to white matter injury. Nat. Neurosci. *27*, 2138–2151. https://doi.org/10.1038/s41593-024-01757-6.

83. Sun, N., Akay, L.A., Murdock, M.H., Park, Y., Galiana-Melendez, F., Bubnys, A., Galani, K., Mathys, H., Jiang, X., Ng, A.P., et al. (2023). Single-nucleus multiregion transcriptomic analysis of brain vasculature in Alzheimer's disease. Nat. Neurosci. *26*, 970–982. https://doi.org/10.1038/s41593-023-01334-3.

84. Profaci, C.P., Munji, R.N., Pulido, R.S., and Daneman, R. (2020). The blood–brain barrier in health and disease: Important unanswered questions. J. Exp. Med. *217*, e20190062. https://doi.org/10.1084/jem.20190062.

85. Mendiola, A.S., Yan, Z., Dixit, K., Johnson, J.R., Bouhaddou, M., Meyer-Franke, A., Shin, M.G., Yong, Y., Agrawal, A., MacDonald, E., et al. (2023). Defining blood-induced microglia functions in neurodegeneration through multiomic profiling. Nat. Immunol. *24*, 1173–1187. https://doi.org/10.1038/s41590-023-01522-0.

86. Niceta, M., Stellacci, E., Gripp, K.W., Zampino, G., Kousi, M., Anselmi, M., Traversa, A., Ciolfi, A., Stabley, D., Bruselles, A., et al. (2015). Mutations impairing GSK3-mediated MAF phosphorylation cause cataract, deafness, intellectual disability, seizures, and a down syndrome-like facies. Am. J. Hum. Genet. *96*, 816–825. https://doi.org/10.1016/j.ajhg.2015.03.001.

87. Tiedt, R., Schomber, T., Hao-Shen, H., and Skoda, R.C. (2007). Pf4-Cre transgenic mice allow the generation of lineage-restricted gene knockouts for studying megakaryocyte and platelet function in vivo. Blood *109*, 1503–1506. https://doi.org/10.1182/blood-2006-04-020362.

88. Liu, J.L., Grinberg, A., Westphal, H., Sauer, B., Accili, D., Karas, M., and LeRoith, D. (1998). Insulin-Like Growth Factor-I Affects Perinatal Lethality and Postnatal Development in a Gene Dosage-Dependent Manner: Manipulation Using the Cre/loxP System in Transgenic Mice. Mol. Endocrinol. *12*, 1452–1462. https://doi.org/10.1210/mend.12.9.0162.

89. Foley, K.E., Hewes, A.A., Garceau, D.T., Kotredes, K.P., Carter, G.W., Sasner, M., and Howell, G.R. (2022). The APOEε3/ε4 Genotype Drives Distinct Gene Signatures in the Cortex of Young Mice. Front. Aging Neurosci. *14*, 838436. https://doi.org/10.3389/fnagi.2022.838436.

90. Wang, J.M., Chen, A.F., and Zhang, K. (2016). Isolation and primary culture of mouse aortic endothelial cells. J. Vis. Exp. 52965. https://doi.org/10.3791/52965.

91. Da Mesquita, S., Louveau, A., Vaccari, A., Smirnov, I., Cornelison, R.C., Kingsmore, K.M., Contarino, C., Onengut-Gumuscu, S., Farber, E., Raper, D., et al. (2018). Functional aspects of meningeal lymphatics in ageing and Alzheimer's disease. Nature *560*, 185–191. https://doi.org/10.1038/s41586-018-0368-8.

92. Schneider, C.A., Rasband, W.S., and Eliceiri, K.W. (2012). NIH Image to ImageJ: 25 years of image analysis. Nat. Methods *9*, 671–675. https://doi.org/10.1038/nmeth.2089.

93. Ning, B., Kennedy, M.J., Dixon, A.J., Sun, N., Cao, R., Soetikno, B.T., Chen, R., Zhou, Q., Kirk Shung, K., Hossack, J.A., et al. (2015). Simultaneous photoacoustic microscopy of microvascular anatomy, oxygen saturation, and blood flow. Opt. Lett. *40*, 910–913. https://doi.org/10.1364/ol.40.000910.

94. Cao, R., Li, J., Ning, B., Sun, N., Wang, T., Zuo, Z., and Hu, S. (2017). Functional and oxygen-metabolic photoacoustic microscopy of the awake mouse brain. Neuroimage *150*, 77–87. https://doi.org/10.1016/j.neuroimage.2017.01.049.

95. Drew, P.J., Shih, A.Y., Driscoll, J.D., Knutsen, P.M., Blinder, P., Davalos, D., Akassoglou, K., Tsai, P.S., and Kleinfeld, D. (2010). Chronic optical access through a polished and reinforced thinned skull. Nat. Methods *7*, 981–984. https://doi.org/10.1038/nmeth.1530.

96. Cao, R., Tran, A., Li, J., Xu, Z., Sun, N., Zuo, Z., and Hu, S. (2021). Hemodynamic and oxygen-metabolic responses of the awake mouse brain to hypercapnia revealed by multi-parametric photoacoustic microscopy. J. Cereb. Blood Flow Metab. *41*, 2628–2639. https://doi.org/10.1177/0271678X211010352.

97. Wang, T., Sun, N., Cao, R., Ning, B., Chen, R., Zhou, Q., and Hu, S. (2016). Multiparametric photoacoustic microscopy of the mouse brain with 300-kHz A-line rate. Neurophotonics *3*, 045006. https://doi.org/10.1117/1.nph.3.4.045006.

98. Chen, S.-L., Xie, Z., Carson, P.L., Wang, X., and Guo, L.J. (2011). In vivo flow speed measurement of capillaries by photoacoustic correlation spectroscopy. Opt. Lett. *36*, 4017–4019. https://doi.org/10.1364/ol.36.004017.

99. Labun, K., Montague, T.G., Krause, M., Torres Cleuren, Y.N., Tjeldnes, H., and Valen, E. (2019). CHOPCHOP v3: Expanding the CRISPR web toolbox beyond genome editing. Nucleic Acids Res. *47*, W171–W174. https://doi.org/10.1093/nar/gkz365.

100. Picelli, S., Faridani, O.R., Björklund, A.K., Winberg, G., Sagasser, S., and Sandberg, R. (2014). Full-length RNA-seq from single cells using Smart-seq2. Nat. Protoc. *9*, 171–181. https://doi.org/10.1038/nprot.2014.006.

101. Dobin, A., Davis, C.A., Schlesinger, F., Drenkow, J., Zaleski, C., Jha, S., Batut, P., Chaisson, M., and Gingeras, T.R. (2013). STAR: Ultrafast universal RNA-seq aligner. Bioinformatics *29*, 15–21. https://doi.org/10.1093/bioinformatics/bts635.

102. Skene, P.J., Henikoff, J.G., and Henikoff, S. (2018). Targeted in situ genome-wide profiling with high efficiency for low cell numbers. Nat. Protoc. *13*, 1006–1019. https://doi.org/10.1038/nprot.2018.015.

103. Meers, M.P., Bryson, T.D., Henikoff, J.G., and Henikoff, S. (2019). Improved cut&run chromatin profiling tools. eLife *8*, e46314. https://doi.org/10.7554/eLife.46314.

104. Liao, Y., Smyth, G.K., and Shi, W. (2019). The R package Rsubread is easier, faster, cheaper and better for alignment and quantification of RNA sequencing reads. Nucleic Acids Res. *47*, e47. https://doi.org/10.1093/nar/gkz114.

105. Robinson, M.D., and Oshlack, A. (2010). A scaling normalization method for differential expression analysis of RNA-seq data. Genome Biol. *11*, R25. https://doi.org/10.1186/gb-2010-11-3-r25.

106. Chen, S., Zhou, Y., Chen, Y., and Gu, J. (2018). Fastp: An ultra-fast all-in-one FASTQ preprocessor. Bioinformatics *34*, i884–i890. https://doi.org/10.1093/bioinformatics/bty560.

107. Kim, D., Paggi, J.M., Park, C., Bennett, C., and Salzberg, S.L. (2019). Graph-based genome alignment and genotyping with HISAT2 and HISAT-genotype. Nat. Biotechnol. *37*, 907–915. https://doi.org/10.1038/s41587-019-0201-4.

108. Hao, Y., Hao, S., Andersen-Nissen, E., Mauck, W.M., 3rd, Zheng, S., Butler, A., Lee, M.J., Wilk, A.J., Darby, C., Zager, M., et al. (2021). Integrated analysis of multimodal single-cell data. Cell *184*, 3573–3587.e29. https://doi.org/10.1016/j.cell.2021.04.048.

109. Subramanian, A., Tamayo, P., Mootha, V.K., Mukherjee, S., Ebert, B.L., Gillette, M.A., Paulovich, A., Pomeroy, S.L., Golub, T.R., Lander, E.S., et al. (2005). Gene set enrichment analysis: A knowledge-based approach for interpreting genome-wide expression profiles. Proc. Natl. Acad. Sci. USA *102*, 15545–15550. https://doi.org/10.1073/pnas.0506580102.

110. Jin, S., Guerrero-Juarez, C.F., Zhang, L., Chang, I., Ramos, R., Kuan, C.-H., Myung, P., Plikus, M.V., and Nie, Q. (2021). Inference and analysis of cell-cell communication using CellChat. Nat. Commun. *12*, 1088. https://doi.org/10.1038/s41467-021-21246-9.

111. Browaeys, R., Saelens, W., and Saeys, Y. (2020). NicheNet: modeling intercellular communication by linking ligands to target genes. Nat. Methods *17*, 159–162. https://doi.org/10.1038/s41592-019-0667-5.

112. Ostuni, R., Piccolo, V., Barozzi, I., Polletti, S., Termanini, A., Bonifacio, S., Curina, A., Prosperini, E., Ghisletti, S., and Natoli, G. (2013). Latent enhancers activated by stimulation in differentiated cells. Cell *152*, 157–171. https://doi.org/10.1016/j.cell.2012.12.018.

113. Freitas, K.A., Belk, J.A., Sotillo, E., Quinn, P.J., Ramello, M.C., Malipatlolla, M., Daniel, B., Sandor, K., Klysz, D., Bjelajac, J., et al. (2022). Enhanced T cell effector activity by targeting the Mediator kinase module. Science *378*, eabn5647. https://doi.org/10.1126/science.abn5647.

114. Zhang, Y., Liu, T., Meyer, C.A., Eeckhoute, J., Johnson, D.S., Bernstein, B.E., Nusbaum, C., Myers, R.M., Brown, M., Li, W., et al. (2008). Model-based analysis of ChIP-Seq (MACS). Genome Biol. *9*, R137. https://doi.org/10.1186/gb-2008-9-9-r137.

115. Heinz, S., Benner, C., Spann, N., Bertolino, E., Lin, Y.C., Laslo, P., Cheng, J.X., Murre, C., Singh, H., and Glass, C.K. (2010). Simple Combinations of Lineage-Determining Transcription Factors Prime cis-Regulatory Elements Required for Macrophage and B Cell Identities. Mol. Cell *38*, 576–589. https://doi.org/10.1016/j.molcel.2010.05.004.

116. Giambartolomei, C., Vukcevic, D., Schadt, E.E., Franke, L., Hingorani, A.D., Wallace, C., and Plagnol, V. (2014). Bayesian Test for Colocalisation between Pairs of Genetic Association Studies Using Summary Statistics. PLoS Genet. *10*, e1004383. https://doi.org/10.1371/journal.pgen.1004383.

117. de Klein, N., Tsai, E.A., Vochteloo, M., Baird, D., Huang, Y., Chen, C.Y., van Dam, S., Oelen, R., Deelen, P., Bakker, O.B., et al. (2023). Brain expression quantitative trait locus and network analyses reveal downstream effects and putative drivers for brain-related diseases. Nat. Genet. *55*, 377–388. https://doi.org/10.1038/s41588-023-01300-6.

118. Hemani, G., Zheng, J., Elsworth, B., Wade, K.H., Haberland, V., Baird, D., Laurin, C., Burgess, S., Bowden, J., Langdon, R., et al. (2018). The MR-base platform supports systematic causal inference across the human phenome. eLife *7*, e34408. https://doi.org/10.7554/eLife.34408.

119. Minniti, J., Checler, F., Duplan, E., and Alves da Costa, C. (2025). TFinder: A Python Web Tool for Predicting Transcription Factor Binding Sites. J. Mol. Biol. *437*, 168921. https://doi.org/10.1016/j.jmb.2024.168921.

120. Li, D., Hsu, S., Purushotham, D., Sears, R.L., and Wang, T. (2019). WashU Epigenome Browser update 2019. Nucleic Acids Res. *47*, W158–W165. https://doi.org/10.1093/nar/gkz348.

Please cite this article in press as: Brioschi et al., Brain perivascular macrophages regulate endothelial cell function via a cMAF-dependent transcriptional program in mouse and human, Cell (2026), https://doi.org/10.1016/j.cell.2026.07.043

STAR★METHODS

KEY RESOURCES TABLE

REAGENT or RESOURCE	SOURCE	IDENTIFIER
Antibodies		
anti-mouse CD115 (CSF-1R) Brilliant Violet 421	BioLegend	Cat# 135513; RRID:AB_2562667
anti-mouse CD163 PE	Thermo Fisher Scientific	Cat# 12-1631-82; RRID:AB_2716924
anti-mouse CD206 (MMR) PE/Cyanine7	BioLegend	Cat# 141720; RRID:AB_2562248
anti-mouse CD31 (PECAM-1) PE	BioLegend	Cat# 160204; RRID:AB_2876567
anti-mouse CD31 Alexa Fluor 647	BioLegend	Cat# 102416; RRID:AB_493410
anti-mouse CD335 (NKp46) FITC	BioLegend	Cat# 137606; RRID:AB_2298210
anti-mouse CD43 FITC	BioLegend	Cat# 143204; RRID:AB_10960745
anti-mouse CD45 Alexa Fluor 647	BioLegend	Cat# 103124; RRID:AB_493533
anti-mouse CD45 APC-eFluor 780	Thermo Fisher Scientific	Cat# 47-0451-82; RRID:AB_1548781
anti-mouse CD45 PE	BioLegend	Cat# 103106; RRID:AB_312971
anti-mouse CD45.2 PE	BioLegend	Cat# 109807; RRID:AB_313444
anti-mouse CX3CR1 APC	BioLegend	Cat# 149008; RRID:AB_2564492
anti-mouse F4/80 PE	BioLegend	Cat# 123110; RRID:AB_893486
anti-mouse I-A/I-E Brilliant Violet 650	BioLegend	Cat# 107641; RRID:AB_2565975
anti-mouse Ly-6C APC/Cyanine7	BioLegend	Cat# 128026; RRID:AB_10640120
anti-mouse Ly-6C FITC	BioLegend	Cat# 128006; RRID:AB_1186135
anti-mouse Ly-6G APC	BioLegend	Cat# 127614; RRID:AB_2227348
anti-mouse Ly-6G FITC	BioLegend	Cat# 127606; RRID:AB_1236494
anti-mouse MERTK Brilliant Violet 711	BioLegend	Cat# 151515; RRID:AB_2876505
anti-mouse P2RY12 PE/Cyanine7	BioLegend	Cat# 848025; RRID:AB_3106144
anti-mouse SIGLEC-H Biotin	Thermo Fisher Scientific	Cat# 14-0333-82; RRID:AB_1107009
anti-mouse TMEM119 PE	Thermo Fisher Scientific	Cat# 12-6119-82; RRID:AB_2848262
anti-mouse/human CD11b APC	BioLegend	Cat# 101212; RRID:AB_312795
anti-mouse/human CD11b APC/Cyanine7	BioLegend	Cat# 101226; RRID:AB_830642
anti-mouse/human CD11b BB515	BD Biosciences	Cat# 564454; RRID:AB_2665392
anti-mouse/human CD11b Brilliant Violet 421	BioLegend	Cat# 101235; RRID:AB_10897942
anti-mouse/human CD11b PE/Cyanine7	BioLegend	Cat# 101216; RRID:AB_312799
anti-mouse/human CD44 FITC	BioLegend	Cat# 103022; RRID:AB_493685
anti-mouse TotalSeq-B0301 Hashtag 1	BioLegend	Cat# 155831; RRID:AB_2814067
anti-mouse TotalSeq-B0302 Hashtag 2	BioLegend	Cat# 155833; RRID:AB_2814068
anti-human CD163, mouse	Thermo Fisher Scientific	Cat# MA5-11458; RRID:AB_10982556
anti-human CD163, rabbit	Abcam	Cat# ab182422; RRID:AB_2753196
anti-human CD34, mouse	Leica Biosystems	Cat# NCL-END; RRID:AB_442089
anti-human c-MAF Alexa Fluor 647, rabbit	Abcam	Cat# ab225416; RRID:AB_2868542
anti-human Collagen IV, rabbit	Abcam	Cat# ab214417; RRID:AB_2801511
anti-human HLA-DP/DR/DQ, mouse	Santa Cruz Biotechnology	Cat# sc-130013; RRID:AB_2012533
anti-human β-Amyloid Alexa Fluor 488, rabbit	Cell Signaling Technology	Cat# 51374; RRID:AB_2799392
anti-mouse CD206, rabbit	Cell Signaling Technology	Cat# 24595; RRID:AB_2892682
anti-mouse CD206, rat	BioLegend	Cat# 141702; RRID:AB_10900233
anti-mouse Collagen IV, rabbit	Abcam	Cat# ab6586; RRID:AB_305584
anti-mouse F4/80, rat	Cell Signaling Technology	Cat# 71299; RRID:AB_2938669
anti-mouse I-A/I-E, rat	BioLegend	Cat# 107602; RRID:AB_313317
anti-mouse IBA1, rabbit	Cell Signaling Technology	Cat# 17198; RRID:AB_2820254

(*Continued on next page*)

Please cite this article in press as: Brioschi et al., Brain perivascular macrophages regulate endothelial cell function via a cMAF-dependent transcriptional program in mouse and human, Cell (2026), https://doi.org/10.1016/j.cell.2026.07.043

Continued

REAGENT or RESOURCE	SOURCE	IDENTIFIER
anti-mouse LYVE-1, rabbit	Cell Signaling Technology	Cat# 67538; RRID:AB_3750510
anti-mouse Podocalyxin, goat	R&D Systems	Cat# AF1556; RRID:AB_354858
anti-mouse TMEM119, rabbit	Cell Signaling Technology	Cat# 90840; RRID:AB_2928137
anti-rabbit IgG (H+L) Alexa Fluor 647, donkey	Thermo Fisher Scientific	Cat# A-31573; RRID:AB_2536183
anti-rat IgG (H+L) Alexa Fluor 488, goat	Thermo Fisher Scientific	Cat# A-11006; RRID:AB_2534074
anti-goat IgG (H+L) Alexa Fluor 488, donkey	Thermo Fisher Scientific	Cat# A-11055; RRID:AB_2534102
anti-Rat IgG (H+L) Alexa Fluor 750, goat	Thermo Fisher Scientific	Cat# SA000096; RRID:AB_2943057
anti-mouse c-MAF, rabbit	Abcam	Cat# ab77071; RRID:AB_1951643
anti-mouse c-MAF, rabbit	Abcam	Cat# ab77071; RRID:AB_1951643
anti-mouse IGF-I Receptor, rabbit	Cell Signaling Technology	Cat# 9750; RRID:AB_10950969
anti-mouse phospho-IGF-I Receptor-β (Tyr1135), rabbit	Cell Signaling Technology	Cat# 3918; RRID:AB_10548764
anti-mouse phospho-IGF-I Receptor-β (Tyr980), rabbit	Cell Signaling Technology	Cat# 4568; RRID:AB_2122279
anti-mouse Vinculin, mouse	Millipore	Cat# 05-386; RRID:AB_11212640
anti-mouse β-Actin, rabbit	Cell Signaling Technology	Cat# 8457; RRID:AB_10950489
anti-mouse IgG HRP, goat	Thermo Fisher Scientific	Cat# 62-6520; RRID:AB_2533947
anti-rabbit IgG HRP, goat	Cell Signaling Technology	Cat# 7074; RRID:AB_2099233
Chemicals, peptides, and recombinant proteins		
Complete Endothelial Cell Medium Kit	Cell Biologics	Cat# M1168
DAPI	Millipore Sigma	Cat# D9542
Dextran 10kDa Alexa Fluor 488	Thermo Fisher Scientific	Cat# D22910
EZ-Link Sulfo-NHS-LC-Biotin	Thermo Fisher Scientific	Cat# 21335
LIVE/DEAD Fixable Aqua Dead Cell Stain Kit	Thermo Fisher Scientific	Cat# L34957
Mini-PROTEAN TGX gels	Bio-Rad	Cat# 456-1094
Novolink Polymer	Leica Biosystem	Cat# RE7280-CE
Ovalbumin Alexa Fluor 647	Thermo Fisher Scientific	Cat# O34784
Protein A/G-MNase	Epicypher	Cat# 15-1016
Recombinant Mouse Gas6	R&D Systems	Cat# 8310-GS
Recombinant Mouse IGF-I	PeproTech	Cat# 250-19-50UG
Restore Western Blot Stripping Buffer	Thermo Fisher Scientific	Cat# 21059
RNasin Ribonuclease Inhibitor	Promega	Cat# N2111
Streptavidin Alexa Fluor 750	Thermo Fisher Scientific	Cat# S21384
Streptavidin Brilliant Violet 421	Biolegend	Cat# 405225
SuperSignal West Pico PLUS Chemiluminescent Substrate	Thermo Fisher Scientific	Cat# 34577
Tomato-Lectin DyLight 488	Vector Laboratories	Cat# DL-1174-1
Tomato-Lectin DyLight 649	Vector Laboratories	Cat# DL-1178-1
Tyramide Alexa Fluor 488	Thermo Fisher Scientific	Cat# B40953
Tyramide CF555	Biotium	Cat# 96021
Tyramide CF647	Biotium	Cat# 96022
Tyramide CF754	Biotium	Cat# 96090
UltraPure BSA	Thermo Fisher Scientific	Cat# AM2616
Critical commercial assays		
RNAscope HiPlex Assay V2	Advanced Cell Diagnostics	Cat# 324419
Hybridization probes targeting Igf1r	Bio-Techne	Cat# 417561_T2
Hybridization probes targeting Igf1	Bio-Techne	Cat# 443901_T3
RNeasy Micro Kit	Qiagen	Cat# 74004
Nuclear Extract Kit	Active Motif	Cat# 40010

(*Continued on next page*)

Please cite this article in press as: Brioschi et al., Brain perivascular macrophages regulate endothelial cell function via a cMAF-dependent transcriptional program in mouse and human, Cell (2026), https://doi.org/10.1016/j.cell.2026.07.043

Continued

REAGENT or RESOURCE	SOURCE	IDENTIFIER
Chromium Next GEM Single Cell 3′ HT Reagent Kits v3.1	10x Genomics	Cat# CG000416
Chromium GEM-X Single Cell 3′ Reagent Kits v4	10x Genomics	Cat# CG000731
GentleMACS Octo Dissociator with Heaters	Miltenyi Biotec	Cat# 130-134-029
Deposited data		
GEO - GSE298940	This paper	N/A
GEO - GSE213020	Brioschi et al.[22]	N/A
GEO - GSE226092	Fixsen et al.[34]	N/A
GEO - GSE190015	Zhou et al.[51]	N/A
GEO - GSE163577	Yang et al.[52]	N/A
GEO - GSE260461	Rosenzweig et al.[56]	N/A
GEO - GSE256493	Wälchli et al.[55]	N/A
Synapse:syn21670836	Zhou et al.[50]	N/A
Synapse:syn31512863	Fujita et al.[62]	N/A
https://cellxgene.cziscience.com/collections/283d65eb-dd53-496d-adb7-7570c7caa443	Siletti et al.[53]	N/A
https://cells.ucsc.edu/?ds=adult-brain-vasc	Winkler et al.[54]	N/A
https://multivineseq.shinyapps.io/shiny	Reid et al.[64]	N/A
https://genome.ucsc.edu/s/nottalexi/glassLab_BrainCellTypes_hg19	Nott et al.[63]	N/A
Experimental models: Organisms/strains		
C57BL/6J	The Jackson laboratory	RRID:IMSR_JAX:000664
C57BL/6J-Crybb1em1(icre)Cln/J	Colonna Laboratory at WashU	RRID:IMSR_JAX:038436
Maf-flox/flox	Yan Laboratory at University of Louisville	N/A
C57BL/6-Tg(Pf4-icre)Q3Rsko/J	The Jackson laboratory	RRID:IMSR_JAX:008535
B6.129(FVB)-Igf1tm1Dlr/J	The Jackson laboratory	RRID:IMSR_JAX:016831
B6.Cg-Apoeem2(APOE)Adiuj/J*	The Jackson laboratory	RRID:IMSR_JAX:029018
*B6(SJL)-Apoetm1.1(APOE*4)Adiuj/J*	The Jackson laboratory	RRID:IMSR_JAX:027894
Oligonucleotides		
gRNA-1 (*Maf*): TGCGGCCGTCTCATCGCCGG	This paper	N/A
gRNA-2 (*Maf*): CCGGCGATGAGACGGCCGCA	This paper	N/A
gRNA-3 (*Mafb*): CCAGTACAGGTCCTCGAGAT	This paper	N/A
gRNA-4 (*Mafb*): ATCTCGAGGACCTGTACTGG	This paper	N/A
gRNA-5 (control): GGGGTAGGCCTAATTACGGA	This paper	N/A
Software and algorithms		
Imaris v8	Bitplane	RRID:SCR_007370
ImageJ	https://imagej.net/	RRID:SCR_003070
FlowJo v10	BD Biosciences	RRID:SCR_008520
Prism v10	GraphPad	RRID:SCR_002798
CellRanger v8	10x Genomics	RRID:SCR_023221
Seurat v4	https://satijalab.org	RRID:SCR_016341
R Project	https://www.r-project.org/	RRID:SCR_001905
Gene Set Enrichment Analysis (GSEA) v4	https://www.gsea-msigdb.org	RRID:SCR_003199
Metascape	https://metascape.org	RRID:SCR_016620
CellChat v2	https://github.com/sqjin/CellChat	RRID:SCR_021946
NicheNet	https://github.com/saeyslab/nichenetr	RRID:SCR_023158
pySCENIC	https://pyscenic.readthedocs.io/en	RRID:SCR_025802
HOMER	http://homer.ucsd.edu	RRID:SCR_010881
JASPAR	http://jaspar.genereg.net	RRID:SCR_003030
Integrative Genomics Viewer (IGV)	http://www.broadinstitute.org/igv	RRID:SCR_011793

(*Continued on next page*)

Please cite this article in press as: Brioschi et al., Brain perivascular macrophages regulate endothelial cell function via a cMAF-dependent transcriptional program in mouse and human, Cell (2026), https://doi.org/10.1016/j.cell.2026.07.043

Continued

REAGENT or RESOURCE	SOURCE	IDENTIFIER
UCSC Genome Browser	https://genome.ucsc.edu	RRID:SCR_005780
WashU Epigenome Browser	https://epigenomegateway.wustl.edu	RRID:SCR_006208
TwoSampleMR	https://github.com/MRCIEU/TwoSampleMR	RRID:SCR_019010
Coloc	https://github.com/chr1swallace/coloc	RRID:SCR_026041
Picard	http://broadinstitute.github.io/picard	RRID:SCR_006525
Fastp	https://github.com/OpenGene/fastp	RRID:SCR_016962
HISAT2	http://ccb.jhu.edu/software/hisat2/index.shtml	RRID:SCR_015530

EXPERIMENTAL MODEL AND STUDY PARTICIPANT DETAILS

Mouse models

All the animals used in this study were of *C57BL/6J* background and housed under specific pathogen-free conditions at the Washington University School of Medicine animal facility. The *Maf*$^{flox/flox}$ strain[42] was generated and provided by Dr. Jun Yan (University of Louisville School of Medicine) and carries *LoxP* sites flanking *Maf* exon 1. These mice were intercrossed with the *Crybb1-iCre* line[22] generated in the Marco Colonna laboratory (JAX:038436) or with *Pf4-iCre* mice[87] (JAX:008535). *Igf1*$^{flox/flox}$ mice[88] (JAX:016831) were intercrossed with the *Crybb1-iCre* line. These studies included both male and female mice, with both sexes equally distributed across experimental groups. Mice with conditional deletion of *Maf* or *Igf1* did not exhibit appreciable sex-dependent differences in the phenotypes examined. *APOE3* and *APOE4* knock-in female mice[89] (JAX:029018 and JAX:027894) were purchased from Jackson laboratory and co-housed until analysis. As only female mice were used for this strain, sex-dependent effects could not be assessed. The age of the mice at the time of analysis is reported in the figure legends. All experiments involving laboratory animals were performed with the approval of the Institutional Animal Care and Use Committee at Washington University in St. Louis.

Human brain samples

Autopsy brain specimens were obtained from the Mayo Clinic Alzheimer's Disease Research Center (ADRC) brain bank based on neuropathologic diagnoses with appropriate IRB approval (Mayo Clinic IRB 21-001463). Cases were selected and reviewed for AD neuropathologic change (ADNC), including Thal phase, Braak Stage, and CERAD score (Table S1). Grading for cerebral amyloid angiopathy was performed according to NACC criteria by a board-certified neuropathologist (0=none, 1=mild, 2=moderate, 3=severe). Ultimately, twenty-three cases were selected based upon an admixture CAA score and ADNC level, with relative balance of and consideration for age, sex, and *APOE* genotype. No significant differences were observed between male and female donors in the histological analyses of perivascular macrophages.

Primary cell cultures (bone marrow derived macrophages, BMDM)

C57BL/6J bone marrow cells were collected from femurs and tibias crushed in a mortar, filtered through a 70 μm strainer in 50 ml PBS and centrifuged 450 x g for 5 minutes. Cell pellets underwent RBC lysis, before being filtered and centrifuged as before. For BMDM differentiation, cells were cultured in IMDM medium supplemented with 20% FBS, 10% L929-conditioned medium containing M-CSF, 2mM L-glutamine, 5mM 2-mercaptoethanol and antibiotics (penicillin G 100 U/ml and streptomycin sulfate 100 U/ml). After 6 days of culture, BMDMs were collected.

Primary cell cultures (endothelial cells)

Primary aortic endothelial cell cultures were prepared as previously described, with minor modifications.[90] Briefly, 3-month-old C57BL/6 mice were anesthetized with a ketamine/xylazine injection and perfused via the left ventricle with 1ml of room-temperature PBS containing heparin (1,000 U/ml), immediately followed by perfusion with 5ml of ice-cold PBS to remove residual blood cells. The thoracic aorta was dissected using micro-dissection tools and transferred to a Petri dish containing ice-cold PBS. Residual adipose tissue was carefully removed with surgical forceps, and the aorta was cut into 3-4 segments of approximately 1 cm each. Segments were then opened longitudinally using micro scissors and placed lumen-side down in a 6-well plate pre-coated with Matrigel (Corning). The aorta segments were immediately incubated at 37°C with 5% CO2 in 200μl of Endothelial Cell Medium (Cell Biologics, M1168), prepared according to the manufacturer's instructions. After 4 hours, 2ml of additional medium was added to each well. After 4-5 days, the sections were carefully removed from the Matrigel, and adherent endothelial cells were left expanding for an additional 4-5 days. Cells were then dissociated from the Matrigel using Cell Recovery Solution (Corning), re-plated in a 24-well plate coated with 0.1% gelatin and expanded for 2 days, as described above.

Primary brain endothelial cells (BEC) were prepared from 6-week-old C57BL/6 mice as described in the "sample preparation for flow cytometry and sorting" section. Brain cell pellets were stained with CD45-AlexaFluor 647 (1:200), CD31-PE (1:100), and

Please cite this article in press as: Brioschi et al., Brain perivascular macrophages regulate endothelial cell function via a cMAF-dependent transcriptional program in mouse and human, Cell (2026), https://doi.org/10.1016/j.cell.2026.07.043

Ly6C-APCCy7 (1:200) for 30 minutes on ice (antibody details on the key resources table). DAPI was used for live/dead cells discrimination. The DAPI$^-$CD45$^-$CD31$^+$Ly6C$^+$ population was sorted on FACS Aria-III (BD Bioscience) using a 100 μm nozzle. Approximately 600,000 cells per sample were sorted (two brains were pooled for each sample). BECs were collected into Endothelial Cell Medium (Cell Biologics, M1168), plated onto a Matrigel-coated 24-well plate and expanded for 12 days in Endothelial Cell Medium. Matrigel was removed using Cell Recovery Solution (Corning) prior to RNA extraction.

On the day of the experiment, aortic endothelial cells or BEC were incubated in serum-free medium for 2 hours prior to stimulation with recombinant mouse GAS6 (250 ng/mL; R&D Systems) and recombinant mouse IGF1 (200 ng/mL; PeproTech), or PBS as a control. After 6 hours stimulation, the medium was removed, and wells were washed with PBS. Cells were lysed in 450μl of lysis buffer for RNA extraction. The lysate was mixed by pipetting and briefly shaken for 1 minute at room temperature. Lysates were collected, and RNA was purified using the RNeasy Micro Kit (Qiagen), following the manufacturer's protocol. Purified RNA was stored at −80°C until analysis.

METHOD DETAILS

Sample preparation for flow cytometry and sorting

Unless otherwise specified, the entire sample preparation was carried out on ice or at 4°C. Mice received a lethal dose of the Ketamine/Xylazine cocktail by intraperitoneal (ip.) injection. After the loss of the paw-pinch reflex, mice were transcardially perfused with 20 ml of ice-cold phosphate-buffered saline (PBS, Corning). Cortices were dissected and transferred into a dounce homogenizer with cold Dulbecco's Modified Eagle Medium (DMEM, Gibco) supplemented with 0.5% Bovine Serum Albumin (BSA, Rockland) and 2.5 mM EDTA (Corning). After homogenization the cell suspension was filtered through a 70μm strainer and pellets were resuspended in 30% isotonic percoll (GE Healthcare). Myelin was depleted by centrifugation at 800g for 20 minutes. The cell pellets were then stained for flow cytometry analysis or sorting.

For flow cytometry analyses, single-cell suspensions underwent live/dead staining (LIVE/DEAD Fixable Aqua, Thermo Fisher) at a 1:1000 dilution in PBS for 30 minutes, followed by Fc-receptor blocking (clone 2.4G2, made in-house from HB-197 hybridoma cells). Surface staining was performed for 30 minutes to 1 hour (antibody details on the key resources table). Flow cytometry analysis was conducted on Symphony A3 (BD Bioscience). Raw data were analyzed with FlowJo v10. To sort brain macrophages in adult mice, cells were stained with CD45-PE (1:200), CD11b-APC (1:100), and lineage exclusion mix (Ly6C-FITC 1:200, Ly6G-FITC 1:200, CD43-FITC 1:100, CD44-FITC 1:100, NKp46-FITC 1:100) for 30 minutes. To sort brain macrophages in P0 pups, cells were stained with CD45-AlexaFluor-674 (1:100), CD11b-APCCy7 (1:100), F4/80-PE (1:50), CD206-PECy7 (1:50), MHCII-BV650 (1:400) and lineage exclusion mix (Ly6C-FITC 1:200, Ly6G-FITC 1:200, CD43-FITC 1:100, NKp46-FITC 1:100) for 30 minutes. For live/dead discrimination, a 1 mg/ml of DAPI (4′,6-diamidino-2-phenylindole, Sigma) at 1:5000 final dilution was added to the sample immediately prior to sorting. Sorting was performed on FACS Aria-III (BD Bioscience) using a default 85μm nozzle, and macrophages were collected into a 1.5ml Eppendorf tube containing PBS + 0.4% UltraPure BSA (Thermo Fisher) + 1U/μl of Recombinant RNasin Ribonuclease Inhibitor (Promega).

To sort brain blood vessels, cortices were homogenized with GentleMACS tissue dissociator (Mylteni Biotech) in prewarmed DMEM supplemented with 2% Bovine Calf Serum (BCS, HyClone), 25μg/ml Liberase DL, 100μg/ml Dispase, 0.5mg/ml Papain, 10μg/ml DNase-I (all enzymes from Sigma) for 30 minutes at 37°C. After homogenization the cell suspension was filtered through a 70 μm strainer and myelin depletion was performed in 30% isotonic percoll at 800g for 20 minutes at 4°C. Cell pellets were stained with Fc block, CD45-PE (1:200), CD31-AlexaFluor-647 (1:100), and Ly6C-APCCy7 (1:200) for 30 minutes on ice (antibody details on the key resources table). DAPI was used for live/dead staining as described above. The CD45$^-$DAPI$^-$ double-negative population was sorted on FACS Aria-III (BD Bioscience) using a 100μm nozzle. Cells were collected into a 1.5ml Eppendorf tube containing PBS + 0.4% UltraPure BSA (Thermo Fisher) + 1U/μl of Recombinant RNasin Ribonuclease Inhibitor (Promega). With this isolation protocol, we confirmed that the CD31$^+$Ly6C$^+$ cells (endothelial) account for approximately 70% of the total CD45$^-$DAPI$^-$ population.

Cerebrospinal fluid circulation and glymphatic flow

Mice were anesthetized by ip. injection of 100 mg/kg ketamine and 10 mg/kg xylazine. The fur was shaved from the neck and head and the mice were immobilized in a stereotaxic device. Skin and muscles on the posterior side of the neck were incised to expose the cisterna magna. A 3μl tracer solution containing 1.5μl OVA-AlexaFlur-647 (4 mg/ml stock, Thermo Fisher) and 1.5μl Dextran-AlexaFluor-488 10kDa (1 mg/ml stock, Thermo Fisher) diluted in aCSF were injected intra-cisterna magna (i.c.m) using a 33-gauge Hamilton syringe at approximately 3μl/minute. The syringe was left in place for 1 minute after injection to prevent backflow. CSF flow analysis was performed as previously described.[45] Briefly, the temporal skull bone was surgically exposed, and intravital imaging of the MCA was performed under a stereomicroscope (Leica, M205 FA) at 4 frames/minute for one hour. Mice were then perfused with ice-cold PBS prior tissue collection. Brain and deep cervical lymph nodes (dCLN) were harvested and fixed in 4% PFA for post-mortem analyses. Imaging of brain and dCLN cryosections sections was performed using a VS200-S6 slide scanner (Olympus) with a 10×/NA0.4 objective.

Intra-striatal injection was performed as previously described.[45,91] Briefly, mice were anesthetized, shaved and fixed on a stereotaxic device as described above. A craniectomy was performed with a surgical drill above the injection site and a 1μl tracer solution containing 0.5μl OVA-AlexaFluor-647 (4 mg/ml) and 0.5μl Dextran-AlexaFluor-488 10kDa (1 mg/ml stock) diluted in aCSF was

injected at the following Bregma coordinates: AP: +1.5 mm; ML: –1.5 mm; depth: +2.5 mm). Stereotaxic injection was performed at 1μl/minute with a 1.14mm outer diameter glass capillary (World Precision Instruments) mounted on a Nanoliter 2020 injector (World Precision Instruments). Mice were perfused with ice-cold PBS one hour after injection and brains were fixed in 4% PFA. Fluorescent images were acquired using a Zeiss Observer Z1 inverted microscope with a plan-Neofluar 20×/NA0.5 objective (Zeiss), equipped with a Colibri 7 LED light source (Zeiss) and an ORCA-ER digital camera (Hamamatsu Photonics).

NHS-Biotin injection for BBB permeability analysis

Mice were anaesthetized by isoflurane inhalation and injected retro-orbitally with 5 mg of EZ-Link Sulfo-NHS-LC-Biotin (Thermo Fisher) freshly dissolved in PBS. Five minutes later, mice were perfused with ice-cold PBS, and brains were harvested and fixed in 4% PFA for downstream analyses. Fixed brain sections were stained with Alexa Fluor™ 750-conjugated Streptavidin (Thermo Fisher, 1:500) for 2 hours at room temperature and thoroughly washed prior to mounting. Images were acquired using a VS200-S6 slide scanner (Olympus) with a 10×/NA0.4 objective.

Immunofluorescence staining

When blood vessels were imaged, mice anesthetized with Ketamine/Xylazine cocktail received a retroorbital injection of 100μl of fluorophore conjugated Tomato-Lectin (Vector Laboratories) approximately 5 minutes prior to PBS perfusion. Perfused brains were fixed in 4% PFA overnight at 4°C, dehydrated in 30% sucrose (Sigma) solution for at least 48 hours, embedded in OCT medium and frozen at -20°C before being cut into 60 or 100 μm-thick sections at the cryostat (Leica). For antibody staining, 60 μm-thick brain cryosections were blocked for 2 hours at room temperature in PBS with 5% BSA and 0.5% Triton X-100 (Sigma). Primary antibody staining was performed in free-floating in staining buffer (PBS with 1% BSA and 0.5% Triton X-100) for 48 hours at 4°C. Secondary staining with fluorochrome-conjugated antibodies and DAPI (Sigma, 1:4000 dilution from a 1 mg/ml stock solution) was carried out at room temperature for 2 hours (antibody details on the key resources table). For lymphatic and glymphatic flow analyses, 100 μm-thick brain cryosections (free floating) and 30 μm-thick dCLN cryosections (pre-mounted on slides) were counterstained stained with DAPI for 15 minutes at room temperature. Immunostained samples were washed 1x10 minutes in PBS + 0.05% Tween 20 (Fluka) and 2x10 minutes in PBS only at room temperature before being mounted on Superfrost glass slides (Thermo Fisher) and embedded in Prolong Glass anti-fade mounting media (Thermo Fisher) and covered with 1.5H high-precision cover glasses (Marienfeld-Superior).

Confocal microscope

Confocal imaging was performed using a Zeiss LSM880 Airyscan inverted confocal microscope, equipped with a 10X/NA0.6 air objective, a 20X/NA0.8 air objective, a 40×/NA1.4 oil-immersion objective and a 63×/NA1.4 oil-immersion objective and operated by ZEN Black software (ZEISS Efficient Navigation, Zeiss). Z-stack images were acquired with a at a resolution of 2048×2048 pixels. Maximal projections were rendered in Imaris V8.3 (Bitplane, Zurich, Switzerland).

Brain tissue clearing and imaging

Accelerated Deep Adaptable Processing of Tissue for 3-Dimensional Fluorescence Tissue Imaging (ADAPT-3D) was used to achieve optical transparency and immunolabeling of mouse brains as previously described.[43] Briefly, mice were intravenously injected with 100μl of Tomato-Lectin-Dylight488 (Vector Laboratories) and perfused with 20ml ice-cold PBS 5 minutes later. Brains were harvested and immersed in ADAPT-3D fixative overnight followed by decolorization and delipidation of both residual heme and lipids for 3 days. Immunofluorescent antibody staining was performed for CD206 (Cell Signaling, 1:100) and MHCII (Biolegend, 1:200) in blocking solution for an additional 3 days under mild shaking. Secondary staining with fluorochrome-conjugated antibody was performed overnight. Finally, tissues were equilibrated in a 1:1 solution of ADAPT-3D Refractive Index Matching Solution (RIM) for 1 hour before immersion in ADAPT-3D RIM. Brains were mounted on Attofluor Cell Chambers filled with ADAPT-3D RIM. Images were acquired using a seven-laser inverted Leica SP8 microscope, with full spectral hybrid detectors using a 10X NA0.3 objective lens. All image collection was performed using Leica LAS X software, and analysis was performed using Imaris (Bitplane) v10 software.

Immunohistochemistry and immunofluorescence staining of healthy human brains

Immunohistochemistry and immunofluorescence were performed on 2μm-thick formalin-fixed paraffin embedded (FFPE) sections of human frontal cortex, obtained postmortem from N=4 otherwise healthy subjects without clinical evidence of neuroinflammatory conditions (archives of ASST Spedali Civili di Brescia). Endogenous peroxidase was blocked by incubation with methanol (Honeywell) and hydrogen peroxide (AppliChem) 0.03% for 20 minutes during rehydration. Upon antigen retrieval in water bath with EDTA buffer at pH 8.00, immunostaining was performed using primary antibodies against cMAF (clone EPR16484, Abcam), CD163 (clone 10D6, Thermo Fisher) and CD34 (clone QBEnd/10, Leica) for 1 hour at room temperature. Immunohistochemistry reactions were revealed using Novolink Polymer (Leica) followed by diaminobenzidine (DAB, Dako). Second and third immune reaction were visualized using Mach 4 MR-AP (Biocare Medical) followed by Vector Blue (Vector, SK-5300) and StayRed/AP (Abcam). Finally, the slides were counterstained with Meyer's Haematoxylin (Bio-Optica).

For immunofluorescence staining, FFPE sections were incubated in blocking solutions containing 5% BSA in TBS with 1% Tween-20. Primary staining was performed for 1 hour at room temperature using CD163, cMAF, CD34 and HLA DP/DR/DQ (clone PdV5.2,

Please cite this article in press as: Brioschi et al., Brain perivascular macrophages regulate endothelial cell function via a cMAF-dependent transcriptional program in mouse and human, Cell (2026), https://doi.org/10.1016/j.cell.2026.07.043

Santa Cruz Biotechnology) primary antibodies. Secondary staining was performed using Novolink Polymer (Leica) followed by tyramide fluorophore AF488 (Thermo Fisher), CF555, CF647 and CF754 (Biotium). Nuclei were counterstained with DAPI. Sections were digitized using Axioscan7 (Zeiss) equipped with Hamamatsu Orca Flash 4 at 20x magnification using a Colibri 7 LED light source with different excitation modules (385nm, 475nm, 567nm and 761nm).

Immunofluorescence staining of AD brains

Sections from dorsolateral prefrontal cortex were sampled and processed in a routine fashion and in accordance with Mayo ADRC protocol. Formalin-fixed, paraffin-embedded sections were sectioned at 6μm and underwent a deparaffinization and rehydration using a xylene/decreasing ethanol series. Microwave antigen retrieval was performed (10mM tris base with 1mM EDTA and 0.05% Tween20) for 15 min at 99°C and underwent cooling for an additional 30 min. Slides were blocked with 4% FBS in TBS and incubated with primary antibody (rabbit anti-cMAF Abcam, and mouse anti-CD163 Leica) overnight at 4°C. Sections were then incubated with fluorophore-conjugated secondary antibodies 2 hours at room temperature, followed by staining with a 0.0125% Thioflavin-S (Sigma-Aldrich) ethanol solution. Finally, slides were mounted with ProLong Gold Antifade media with DAPI (Invitrogen). Images were acquired using a Revolution EchoScope fluorescence microscope.

For analysis, n=10 leptomeningeal and cortical vessels were selected at random per subject (20X objective, Echoscope), and number of perivascular macrophages co-expressing CD163 and cMAF were counted per vessel. For statistical analysis, average number of $cMAF^{+}$ perivascular macrophages per subject was calculated and plotted as a function of CAA severity.

RNA-scope HiPlex Assay

Four to five weeks old Bl6 mice were perfused in cold PBS, brains were snap frozen in OCT on dry ice and stored at –80°C. Hybridization of *Igf1r* and *Igf1* mRNA was performed using the RNAscope HiPlex Assay V2 method. Briefly, on the day of experiment 20μm-thick sections were mounted onto Superfrost Plus glass slides and dried at –20°C for 1 hour. Sections were fixed in 4% PFA for 60 minutes at room temperature, followed by dehydration in gradients of ethanol (50%>70%>100%). Sections were air dried for 5 minutes prior to incubation with Protease IV for 30 minutes at RT. Probes hybridization was performed for 2h at 40°C targeting *Igf1r* and *Igf1* (Bio-Techne) mRNA followed by amplification using RNAscope HiPlex Amp reagents for 3x30 minutes at 40°C. Probes detection was performed with HiPlex Fluoro T2 (Dylight 550) and T3 (Dylight 650) reagents for 15 minutes at 40°C. Sections were stored in 5xSSC buffer at 4°C until immunofluorescent staining. Sections were blocked and permeabilized (PBS with 2% BSA, 5% donkey serum and 0.2% Triton X-100), followed by staining with goat anti-Podocalyxin (R&D Systems, 1:200) and rat anti-CD206 (BioLegend, 1:100) antibodies for 24 hours at 4°C. Secondary staining with fluorophore-conjugated antibodies and DAPI was performed for 2 hours at RT. Images were acquired using a Stellaris TCS SP8 confocal microscope (Lecia). Row image files were analyzed in ImageJ.[92]

Multi-parametric photoacoustic microscopy

Multi-parametric photoacoustic microscopy (PAM)[93,94] was used for label-free, *in vivo* imaging of cerebral vascular structure and blood flow speed. Prior to imaging, skull thinning was performed under anesthesia (1.5% isoflurane) to enhance image resolution and contrast while minimizing perturbation to brain activity.[94–96] Following skull exposure and fascia removal, the skull over the region of interest was thinned using a surgical hand drill. To prevent overheating and maintain clarity of the thinned-skull window, saline was repeatedly applied throughout the procedure. Mice were allowed to recover for ~30 minutes before being transferred to the PAM system for imaging. Right before imaging, ultrasound gel was applied to the thinned-skull window to ensure acoustic coupling. Subcutaneous electrodes were inserted into the limbs and connected to the PowerLab system (26T, ADInstruments) for heart rate monitoring. Electrocardiogram (ECG) signals were processed and displayed in real time using LabChart 8 Pro (ADInstruments). The body temperature was maintained at 37°C with a temperature-controlled heating pad throughout surgery and imaging. During imaging, mice remained under anesthesia (1% isoflurane). Two imaging sessions were conducted through the thinned-skull window: (1) a baseline session with medical air inhalation and (2) a hypercapnia challenge session using a gas mixture of 90% medical air and 10% CO_2, as previously described.[45,96] The hypercapnia session started 5 minutes after initiating gas delivery to allow for equilibration. PAM data were analyzed in MATLAB. Maximum amplitudes of photoacoustic signals were projected to generate 2D vascular structure images. Blood flow parameters were quantified using a previously reported correlation analysis-based method.[93,97,98] Briefly, PAM data output includes the vessel diameter (D), and the blood flow speed along the central axis of the vessel (V). Cerebral blood flow (CBF) was calculated as:

$$CBF = \frac{\pi D^2 V}{8W}$$

where W is the tissue weight, and π corresponds to ~3.14. The tissue weight was estimated by assuming an average cortical thickness of 1.2 mm and a tissue density of 1.05 g/ml. To quantify the relative change in CBF between baseline and hypercapnia conditions, we computed the CBF change ratio (CBF_CR) as:

$$CBF\_CR = \left(\frac{\pi D^2_{Hypercapnia} V_{Hypercapnia}}{8W_{Hypercapnia}}\right) \Big/ \left(\frac{\pi D^2_{Baseline} V_{Baseline}}{8W_{Baseline}}\right)$$

Please cite this article in press as: Brioschi et al., Brain perivascular macrophages regulate endothelial cell function via a cMAF-dependent transcriptional program in mouse and human, Cell (2026), https://doi.org/10.1016/j.cell.2026.07.043

Because the same region of interest was analyzed under both conditions, $W_{hypercapnia}$ and $W_{baseline}$ were assumed to be identical. This allows the expression to be simplified to:

$$CBF\_CR = \frac{D^2_{Hypercapnia} V_{Hypercapnia}}{D^2_{Baseline} V_{Baseline}}$$

Flow speeds in the same vascular regions were compared between the two conditions, and the mean CBF percentage change was calculated for arteries and veins.

Parabiosis

Mice were anesthetized by ip. injection of ketamine (100 mg/kg) and xylazine (10 mg/kg). Adequate anesthesia was confirmed prior to surgery. The lateral flanks of each mouse were shaved and aseptically prepared using povidone-iodine followed by 70% ethanol. Corresponding longitudinal skin incisions were made extending from the olecranon to the knee joint. The underlying subcutaneous tissue was bluntly dissected to mobilize approximately 0.5 cm of free skin along the incision margins. To minimize tension on the skin closure, the forelimbs and hindlimbs of each pair were joined by suturing the olecranon and knee joints together using absorbable 5-0 Vicryl sutures. The adjacent dermal edges were then aligned and closed with 5-0 nylon sutures. Postoperatively, mice received sustained-release buprenorphine (1 mg/kg) for analgesia and enrofloxacin (Baytril; 2.5 mg/kg) for antimicrobial prophylaxis. Parabiotic mice were housed one pair per cage, provided with softened food placed on the cage floor, and monitored daily for signs of pain, distress, wound dehiscence, or impaired mobility.

After 6 weeks of shared circulation, parabionts were anesthetized with ip. injection of ketamine/xylazine cocktail, and blood was collected from the heart prior to transcardial perfusion with PBS. Brains were subsequently harvested and fixed in 4% PFA overnight at 4°C for downstream imaging analyses.

Western blot of brain endothelial cells

N=3 *Maf*$^{f/f}$*: Cre* and N=3 *Maf*$^{f/f}$ littermate mice (3-months-old) were administered with 100µl Tomato-Lectin Daylight-649 via retroorbital iv. injection under anesthesia, and PBS perfused 5min later. Brain endothelial cells (BEC) were prepared as described in the "sample preparation for flow cytometry and sorting" section, with minor modifications. To avoid the inclusion of immunoglobulin heavy and light chains into the protein extract, antibody staining was omitted. BEC were sorted as DAPI$^-$Tomato-Lectin$^+$ population and approximately one million cells per sample (pool of three brains) were sorted in endothelial cells media (see EC culture method) supplemented with phosphatase inhibitor (Active Motif). Sorted cells were washed three times in cold PBS, followed by cell lysis in 1X lysis buffer with 1mM PMSF (Cell Signaling Technology) for 30 minutes on ice with intermittent vortexing. Cell lysate was spun at 12,000g for 15 minutes and supernatant was collected for estimation of protein concentration and downstream protein denaturation in 4X SDS loading buffer.

Equal amounts of protein were loaded on 4-20% Mini-PROTEAN TGX gels (Bio-Rad), run in tris-glycine SDS buffer and transferred to PVDF (Polyvinylidene Difluoride) membrane in tris-glycine buffer. After transfer, membrane was washed in Tris-buffer saline containing 0.01% Tween-20 (TBS-T) and blocked in 5% BSA. Membrane was then incubated overnight with primary antibody under gentle rocking at +4°C followed by 3 washes with TBS-T and incubation with HRP-conjugated secondary antibody for 2 hours at room temperature. Membrane was washed 3 times and western blot was developed using Chemiluminescent substrate (Thermo Fisher) in a Bio-Rad ChemiDoc MP imaging system. To stain more target proteins, the membrane was incubated in stripping buffer (Thermo Fisher) and underwent the same staining protocol described above. The following antibodies from Cell Signaling Technology were used: anti-Phospho-IGF1 Receptor-β Tyr980, anti-Phospho-IGF1 Receptor-β Tyr1135, anti-IGF1 Receptor-β total protein, anti-β-Actin, anti-Rabbit-HRP.

CRISPR-Cas9 gene editing in BMDMs

Single guide RNAs (sgRNAs) were designed using CHOPCHOP[99] and generated using GeneArt Precision gRNA Synthesis kit following manufacturer's instructions (gRNA sequence in the key resources table). Ribonucleoprotein (RNP) complexes of Cas9-sgRNAs were obtained by incubating 5µg of Cas9 (Thermo Fisher) with 6 µg sgRNA for 15 minutes at room temperature. Bone marrow cells (5x10^5, day 0 of differentiation) were resuspended in P3 solution (Primary Cell 4D-Nucleofector kit), mixed with RNP complex and electroporated using ED-113 program of the 4D-Nucleofector System (Lonza). Control BMDMs were electroporated with scrambled gRNA + Cas9. The culture medium of BMDMs was replaced 24 hours after nucleofection. After 6 days of culture, gene-edited BMDMs were collected for analysis.

Gene-editing efficiency was assessed via Non-Homologous End Joining (NHEJ) at targeted sites. Briefly, genomic DNA was purified using QIAamp DNA Micro kit and targeted regions were amplified by PCR. Amplification products were purified with AMPure XP beads, quantified by NanoDrop 8000 and mixed 1:1 with PCR product from wild-type cells. Annealed PCR products (500 ng) were digested with T7 Endonuclease for 30 minutes at 37°C and subjected to capillary electrophoresis using D1000 TapeStation kit (Agilent 4200 TapeStation). NHEJ frequency was calculated as percentage of cleavage of the PCR product (% NHEJ = 100 x (1 – (1 – Fraction cleaved) x 1/2)).

Maf deletion efficiency was further confirmed in western blot. Briefly, cells were lysed with a buffer containing 10 mM Tris-HCl pH 8, 1 mM EDTA pH 8, 140 mM NaCl, 1% Triton X-100, 0.1% SDS, 0.1% deoxycholate and protease/phosphatase inhibitors. Protein

Please cite this article in press as: Brioschi et al., Brain perivascular macrophages regulate endothelial cell function via a cMAF-dependent transcriptional program in mouse and human, Cell (2026), https://doi.org/10.1016/j.cell.2026.07.043

extracts underwent electrophoresis and immunoblotting with rabbit anti-cMAF (Abcam, 1:1,000) and Mouse anti-Vinculin (Merck Millipore 1:1,000), followed by secondary staining with goat anti-rabbit-HRP and goat anti-mouse-HRP (Thermo Fisher).

Real-Time quantitative PCR

Total RNA was extracted using ReliaPrep RNA Cell Miniprep System and quantified using NanoDrop 8000. Single-stranded cDNA was synthesized using ImProm-II Reverse Transcription System and SuperScript IV Vilo Master Mix starting from 500 ng total RNA. Analysis of *Mrc1* expression was performed using Fast SYBR Green Master Mix on a ViiA7 Real-Time PCR System (primer pairs on the key resources table).

Bulk RNA-seq of BMDMs with CRISPR-Cas9 gene editing (library preparation)

Total RNA from wild-type and *Maf-Mafb* dKO BMDMs was purified using the ReliaPrep RNA Cell Miniprep System (Promega) and RNA-Seq libraries were generated using the Smart-seq2 method.[100] Briefly, 5ng of RNA were retrotranscribed, cDNA was PCR-amplified for 15 cycles and purified with AMPure XP beads. After purification, the concentration was determined using Qubit 3.0 and size distribution was assessed using Agilent 4200 TapeStation system. Then, the tagmentation reaction was performed starting from 0.5 ng of cDNA for 30 minutes at 55°C followed by PCR amplification for 12 cycles. Libraries were then purified with AMPure XP beads, quantified using Qubit 3.0, assessed for fragment size distribution on an Agilent 4200 TapeStation system. Sequencing was performed on an Illumina NovaSeq6000 (1x75bp reads) following manufacturer's instruction.

Bulk RNA-seq of primary endothelial cells (library preparation)

Bulk RNA-seq was performed by the Genome Technology Access Center (GTAC) at the McDonnell Genome Institute (Washington University in St. Louis). Total RNA integrity was determined using Agilent Bioanalyzer. Sequenced samples had an RNA integrity number (RIN) between 9.8 and 10. Library preparation was performed with 10-5ng of total RNA per sample. ds-cDNA was made using the low-input SMARTseq mRNA kit (Takarabio) according to manufacturer's protocol. cDNA was fragmented using a Covaris E220 sonicator using peak incident power 18, duty factor 20%, cycles per burst 50 for 120 seconds. cDNA was blunt ended, had an A base added to the 3' ends, and then had Illumina sequencing adapters ligated to the ends. Ligated fragments were then amplified for 15 cycles using primers incorporating unique dual index tags. Libraries were pooled and sequenced on an Illumina NovaSeqX Plus (2x150 sequencing recipe), targeting 50M reads per sample. Basecalls and demultiplexing were performed with Illumina's bcl2fastq software with a maximum of one mismatch in the indexing read.

10x Genomics single-cell ATAC sequencing (library preparation)

Generation of single-cell ATAC data was previously described.[22] Briefly, over 100,000 $CD45^{+}Ly6G^{-}$ brain immune cells were sorted and processed according to the Multiome 10x Genomics demonstrated protocol (CG000365). Nuclei were extracted using the ATAC cell lysis buffer (10mM Tris-HCl pH 7.4, 10mM NaCl, 3mM MgCl2, 0.1% Tween-20, 0.1% NP-40 Substitute, 0.01% Digitonin, 1% UltraPure BSA, 1mM DTT, and 1U/μl RNase inhibitor, diluted in nuclease-free water). After 3 minutes lysis, nuclei were washed three times in wash buffer (10mM Tris-HCl, 10mM NaCl, 3mM MgCl2, 0.1% Tween-20, 1% UltraPure BSA, 1mM DTT, and 1U/μl RNase inhibitor), before being resuspended in 5μl nuclei buffer (10x Genomics nuclei buffer, 1mM DTT and 1U/μl RNase inhibitor). 10x Genomics operations were performed on the Chromium 3v3.1 Next GEM using Single Cell Multiome ATAC + Gene Expression Reagent Bundle (PN-1000283). Barcoded transposed DNA was amplified for 7 cycles before being purified using SPRIselect beads. Single-cell ATAC libraries were pooled and sequenced on NovaSeq 6000 + S1 flow cell (Illumina) using the XP workflow and a 51x8x16x51 sequencing recipe targeting 250M reads per sample.

10x Genomics single-cell RNA sequencing of brain macrophages (library preparation)

Brain immune cells were isolated as described above in the respective section. Suspension of brain immune cells was stained with the TotalSeq-B anti-mouse Hashtag reagent (Biolegend, B0301 and B0302) at 1:200 dilution in Fc block prior to adding the staining mix with fluorophore conjugated antibodies. Anti-CD45.2-PE (Biolegend) was used for this experiment to avoid competition with the anti-CD45 hashtag. Brain macrophages from two mice per genotype (stained with either B0301 or B0302 reagents) were pooled in one collection tube during sorting. Sorted cells were washed in PBS and resuspended into PBS + 0.04% UltraPure BSA buffer at a concentration of approximately 1,000 cells/μl. Single-cell libraries were prepared using the Chromium Next GEM Single Cell 3′ HT (high throughput) v3.1 protocol in super-loading mode, targeting 40,000 cells/sample. Briefly, cDNA was prepared after the GEM generation and barcoding, followed by the GEM-RT reaction and bead cleanup steps. Purified cDNA was amplified for 11-13 cycles before being cleaned up using SPRIselect beads, and cDNA concentration was determined on the Bioanalyzer. GEX libraries were prepared as recommended by the Chromium Next GEM Single Cell 3′ HT Reagent Kits v3.1 (Dual Index) (CG000416) with appropriate modifications to the PCR cycles based on the calculated cDNA concentration. For sample preparation on the 10x Genomics platform, the Chromium Next GEM Single Cell 3' HT Kit v3.1 - 48 rxns (PN-1000348), Chromium Next GEM Chip M Single Cell Kit - 16 rxns (PN-1000371) and Dual Index Kit TT Set A, 96 rxns (PN-1000215) were used. The concentration of each library was accurately determined through qPCR utilizing the KAPA library Quantification Kit according to the manufacturer's protocol (KAPA Biosystems/Roche) to produce cluster counts appropriate for the Illumina NovaSeq X Plus instrument. Normalized libraries were sequenced on a NovaSeq X Plus Flow Cell using the 151x10x10x151 sequencing recipe according to manufacturer protocol. Read 1 was trimmed to

Please cite this article in press as: Brioschi et al., Brain perivascular macrophages regulate endothelial cell function via a cMAF-dependent transcriptional program in mouse and human, Cell (2026), https://doi.org/10.1016/j.cell.2026.07.043

the 10x Genomics recommendation of 28bp. A median sequencing depth of 50,000 reads/cell was targeted for each gene expression library.

10x Genomics single-cell RNA sequencing of brain vascular cells (library preparation)

Brain vascular cells were isolated as described above in the respective section from two mice per genotype. Sorted cells were washed in PBS and resuspended into PBS + 0.04% UltraPure BSA buffer at a concentration of approximately 1,000 cells/μl. Single-cell libraries were prepared using the Chromium GEM-X Single Cell 3′ v4 protocol, targeting 20,000 cells/sample. Briefly, cDNA was prepared after the GEM generation and barcoding, followed by the GEM-RT reaction and bead cleanup steps. Purified cDNA was amplified for 11-13 cycles before being cleaned up using SPRIselect beads, and cDNA concentration was determined on the Bioanalyzer. GEX libraries were prepared as recommended by the Chromium GEM-X - Single Cell 3′ Reagent Kits v4 (CG000731) with appropriate modifications to the PCR cycles based on the calculated cDNA concentration. For sample preparation on the 10x Genomics platform, the Chromium GEM-X Single Cell 3′ Kit v4 - 16 rxns (PN-1000691), Chromium GEM-X Single Cell 3' Chip Kit v4 - 4 chips (PN-1000690) and Dual Index Kit TT Set A, 96 rxns (PN-1000215) were used. The concentration of each library was accurately determined through qPCR utilizing the KAPA library Quantification Kit according to the manufacturer's protocol (KAPA Biosystems/Roche) to produce cluster counts appropriate for the Illumina NovaSeq X Plus instrument. Normalized libraries were sequenced on a NovaSeq X Plus Flow Cell using the 151x10x10x151 sequencing recipe according to manufacturer protocol. Read 1 was trimmed to the 10x Genomics recommendation of 28bp. A median sequencing depth of 50,000 reads/cell was targeted for each gene expression library.

c-MAF ChIP-seq in BMDMs (library preparation)

Upon differentiation, 10^8 BMDMs were fixed with 1% formaldehyde, and nuclear fractions isolated and lysed as described previously.[101] Fragmented chromatin was obtained using Covaris E220 focused-ultrasonicator and nuclear extracts were incubated overnight at 4°C with Dynabeads Protein G, previously coupled with 10μg of anti-cMAF antibody (Abcam, ab77071). DNA fragments were immunoprecipitated in a 96-well magnet, and de-crosslinked overnight at 65°C. DNA was then purified with AMPure XP beads and quantified with Qubit 3.0. ChIP DNA (5 ng) was used for library preparation with Illumina TruSeq ChIP Library Prep kit and sequenced on Illumina NovaSeq6000 (1x75bp reads).

c-MAF CUT&RUN in microglia and BAMs (library preparation)

CUT&RUN was performed as previously described.[102,103] Approximately 100,000 $CD206^+MHCII^-$ BAMs and microglia sorted from P0 Bl6 brains were resuspended in PBS at 1,000 cells/μl. Cell were bound to Concanavalin A-coated magnetic beads and permeabilized with Wash Buffer (20 mM HEPES pH 7.5, 150 mM NaCl, 0.5 mM spermidine, and one Roche Complete protein inhibitor tablet per 50 mL) containing 0.05% digitonin (Dig Wash). The cells were incubated with anti-cMAF antibody (Abcam, ab77071 at 1:25 dilution) or IgG negative control antibody (Antibodies-online ABIN101961) or H3K27me3 positive control antibody (Cell Signaling 9733S) overnight at 4°C. The slurry was then washed twice with Dig Wash buffer and incubated with Protein A/G-MNase (Epicypher, 15-1016) for 1 hour at 4°C, followed by two additional washes with Dig Wash. Tubes were placed on ice and incubated with Dig Wash containing 2 mM $CaCl_2$ to initiate MNase digestion of bound fragments. After 30 minutes incubation, 4X STOP buffer (80 mM EGTA, 0.05% Digitonin, 100 μg/mL RNase A) was added to stop the reaction, and fragments were released by incubation for 30 minutes at 37°C. The supernatant containing cleaved DNA fragments was transferred to a new tube and used directly as input for barcoded Illumina libraries, as previously described.[102] Libraries were pooled and sequenced on an Illumina NovaSeqX Plus targeting 150M reads.

QUANTIFICATION AND STATISTICAL ANALYSIS

Bulk RNA-seq of BMDMs (analysis)

Reads were aligned to the mm10 mouse reference genome using STAR aligner (v 2.5.3)[104]; the featureCounts function from Rsubread package (v 1.24.2)[105] was used to compute reads over RefSeq Mus musculus transcriptome (mm10), setting minMQS option to 255. Downstream analyses were performed in R (v 3.4.1) with edgeR R package (v. 3.20.7).[106] Read counts of expressed genes were normalized with the Trimmed Mean of M-values (TMM) method using calcNormFactors function. Dispersion was estimated with the estimateDisp function. Differential expression across different conditions was evaluated fitting a negative binomial generalized linear model on the dataset with glmQLFit function and then performing a quasi-likelihood (QL) F-test with glmQLFTest function. Reads per kilo base per million (RPKM) values were computed for each gene with rpkm function. Genes with RPKM > 1.5 in at least two samples in the datasets were retained. DEGs were identified using the following threshold: Log_2(fold-change) >1 or <−1 and P-value <0.01.

Bulk RNA-seq of primary endothelial cells (analysis)

Adapter trimming was performed using fastp (v0.20.1)[107] and reads were aligned to the GRCm39 reference genome using hisat2 (v2.1.0).[108] To count reads overlapping genes, featureCounts v2.0.6 was used, and the output was loaded into R (v4.2.2) for downstream analysis. To identify gene names and biotypes, biomaRt (v2.54.1) was used. The counts matrix was filtered to include only

Please cite this article in press as: Brioschi et al., Brain perivascular macrophages regulate endothelial cell function via a cMAF-dependent transcriptional program in mouse and human, Cell (2026), https://doi.org/10.1016/j.cell.2026.07.043

protein coding genes with a minimum average count of DESeq2=10 across samples. DESeq2 (v1.38.3) was used for differential gene analysis. Results were visualized using ggplot2 (v.3.4.1) and pheatmap (v1.0.12).

10x Genomics single-cell ATAC sequencing (analysis)

Single cell multi-ome data, including scATAC-seq, was previously collected.[22] Bigwig files were exported from ArchR (v1.0.3) using default settings for visualization in the Integrative Genomics Viewer (IGV) as described previously. Downstream analyses were performed in ArchR. Differential motifs and peaks between BAM subsets or microglia were identified using "getMarkerFeatures" and peak lists were visualized with the "markerHeatmap" utility. Footprinting analysis of the cMAF motif was performed using "getFootprints" and "plotFootprints" functions. Putative regulatory elements were linked to the *Maf* promoter using the "getCoAccessibility" and "plotBrowserTrack" tools. Coverages of bigwig files at specific peak lists were also visualized using the "plotHeatmap" function in deepTools (v3.5.4).

Mouse single-cell RNA sequencing data (analysis)

Fastq files from scRNA-seq data were trimmed and aligned to the GRCm39 reference genome (refdata-gex-GRCm39-2024-A available from 10X Genomics) using the "cellranger count" pipeline (v8.0.1). For the brain macrophage dataset, both Gene Expression and Antibody Capture of the TotalSeq-B antibodies were quantified for each sample by supplying a custom Feature Reference spreadsheet to the cellranger count utility. Counts matrices were then loaded into Seurat (v4.4.0) for data normalization, clustering, and visualization.[109] Data was normalized using "NormalizeData" with scale.factor=10,000. The top 2,000 variable features were identified using "FindVariableFeatures" with the "vst" method. For dimensionality reduction, "RunPCA", "FindNeighbors", "RunUMAP", and "FindClusters" were run using the resolution and dimensions specified below for each object.

Initial quality control for both the brain macrophage and endothelial cell datasets, cutoffs of nFeature_RNA $\geq$ 250 and percent.mt genes $\leq$ 20 were used. For the brain macrophage samples, which utilized TotalSeq-B hashtags, an additional filtering step was performed based on the hashtag signals. Cells with high-confidence detection of hashtag-1 and hashtag-2 were determined based on expression of at least 0.7 and 1.2, respectively, in the "ADT" normalized data slot. These cutoffs were determined based on manual gating of positive and negative cells. Double positive and double negative cells were excluded from downstream analysis. After quality filtering, 61,800 cells were used for downstream analysis in the total brain macrophages object (resolution=0.1, dims=1:6). BAMs were re-clustered separately using the same method described above. A minor cluster of residual contaminating microglia was manually excluded, thus yielding 496 cells for analysis (resolution=0.1, dims=1:6). For the vascular cells object, 84,570 cells were obtained after quality filtering (resolution=0.1, dims=1:10).

For Gene Set Enrichment Analysis (GSEA) of the arteries cluster, normalized gene expression for each individual sample was loaded on GSEA (v4.3.3)[110] and enrichment analysis was run on "the m2.all.v2024.1.Mm.symbols.gmt" database at default parameters, using gene_set permutation type and the Diff. of Classes metric for genes ranking. CellChat (v2.1.2) and NicheNet (v2.2.0) were used for cell-cell communication analysis.[111,112] First, the BAM and vascular cells Seurat objects were merged using the merge() function. CellChat analysis and visualizations were performed between indicated cell types to identify putative ligand-receptor interactions. For NicheNet analysis, BAM- specific ligands were determined by using the FindMarkers() function in Seurat with a min.pct=0.05 and adj.p $\leq$ 0.05 cutoffs. The top 100 markers for each cell type were filtered based on mouse "ligand_target_matrix" in NicheNet. The ligand-receptor network was determined between BAM-derived ligands and the putative receptors expressed in the arteries cluster. Finally, we used the "make_heatmap_ggplot" function in NicheNet for data visualization.

c-MAF and SMAD4 ChIP-seq (analysis)

SMAD4 ChIP-seq data was obtained from a previously published study GSE226092.[34] Data for both cMAF and SMAD4 ChIP-seq datasets was processed as previously described.[113] Briefly, adapter trimming was performed using fastp (v0.20.1),[107] reads were aligned to the mm10 reference genome using hisat2 (v2.1.0),[108] duplicates were removed using "Picard markDuplicates" (v2.18.29) (https://github.com/broadinstitute/picard), and then peaks were called using MACS2 (v2.2.9.1).[114] Deduplicated fragments were loaded into R, normalized by total fragment count, and exported as bigwig files for visualization in the Integrative Genomics Viewer (IGV). The HOMER "annotatePeaks.pl" (v5.1) utility was used to obtain the genomic annotation of each peak and the nearest gene of each peak.[115]

cMAF CUT&RUN in microglia and BAMs (analysis)

CUT&RUN data was processed identically to the ChIP-seq data with modifications only for peak calling. Peak calling was performed in MACS2 using modified parameters including the IgG sample as background, –keep-dup all, –nomodel, –nolambda, -q 0.001. Annotation of peaks in coding genes was performed using the HOMER annotatePeaks.pl utility. For correlation and heatmap analysis, peak counts in each sample were normalized to counts per million (CPM) prior to visualization. BigWig tracks were normalized to reads in TSS, identically to the ChIP-seq data, and visualized in IGV.

Human single-nuclei RNA sequencing data (analysis)

Gene expression matrices from three publicly available snRNA-seq studies on the human brain[51–53] were obtained from their respective genomic data repositories (accession numbers provided in the data availability statement). For *Siletti et al.*,[53] only the microglia

Please cite this article in press as: Brioschi et al., Brain perivascular macrophages regulate endothelial cell function via a cMAF-dependent transcriptional program in mouse and human, Cell (2026), https://doi.org/10.1016/j.cell.2026.07.043

supercluster was downloaded from the CELLxGENE archive. Quality control filtering was applied to retain nuclei meeting the following thresholds: <30,000 UMIs per cell; 1,000–4,000 detected genes per cell; mitochondrial genes <10%. Additionally, the snRNA-seq dataset from *Zhou et al.*[50] was obtained from the Seurat object provided by the authors, with quality control performed as in the original study. To minimize variability due to pathological conditions, only samples from healthy or control subjects were selected for downstream analyses.

The datasets were individually normalized using SCTransform, regressing out mitochondrial gene percentages. Integration was performed using the reciprocal PCA method in Seurat, accounting for cross-dataset heterogeneity and due to the dataset's size. 3,000 features were used for integration. The resulting integrated dataset was then subsetted to retain only macrophages, identified by the enrichment of myeloid marker genes, and re-integrated using Seurat's canonical correlation analysis method with 3,000 integration features. PCA was conducted on the integrated matrix, followed by nearest-neighbor graph construction, UMAP, and clustering. Clusters were annotated as Microglia or BAMs based on gene expression profiles, following manual exclusion of a contaminating T cell cluster.

For transcription factor activity analysis of the healthy human brain, the macrophage population was downsampled to a maximum of 4,000 cells per cluster to optimize computational efficiency. The log-normalized gene expression matrix was extracted, and genes not meeting the filtering thresholds (minimum of 6 UMI counts per sample, expression in at least 1% of cells, and inclusion in the RcisTarget database) were excluded. The filtered matrix was then converted into a.loom file, and SCENIC analysis was performed using the command-line interface of pySCENIC via the Docker image (aertslab/pyscenic_scanpy:0.12.1_1.9.1). The.loom output from pySCENIC was subsequently loaded into R and integrated back into the Seurat object for data visualization.

snRNA-seq data from AD patients were downloaded from *Rosenzweig et al.*[56] Clustering was performed as described in the analysis of the mouse datasets using the following parameters: resolution=0.1, dims=1:10. Myeloid cells were identified by *CSF1R* expression, while vascular cells were identified by expression of *FLT1, PECAM1*, *CD34*, and both populations were reculstered separately. Subjects with type-II diabetes were excluded to avoid confounding factors. Ligand-receptor analysis between CD163$^+$ BAMs and arteries or mural cells from controls subjects and AD individuals was performed in CellChat (v2.1.2) as described for the mouse section. However, to account for the lower sequencing depth of this dataset, trim=0.05 was used within the computeCommunProb function. Transcription factor activity analysis of CD163$^+$ BAMs comparing controls and AD was conducted in pySCENIC as described above.

Genetic analysis of the *MAF* polymorphism

Colocalization analysis was performed using the coloc.abf() function from the coloc (v. 5.2.3)[116] package in R (v. 4.4.0), to measure the shared regulation between AD risk[60] and *MAF* expression in post-mortem brain cortex samples from European individuals.[117] Variants within 1MB of rs450674 were harmonized to ensure consistent direction of effect and then input into coloc. Results were visualized with the locuscomparer (v. 1.0.0) package in R. To test potential causality of *MAF* expression on AD risk, Mendelian randomization (MR) analysis was conducted using the TwoSampleMR (v. 0.6.4) package[118] in R. Only SNPs with significant *MAF* eQTL ($P < 5x10^{-3}$) and not in linkage disequilibrium (LD) with each other ($R^2 < 0.001$) were selected for analysis, and MR was run using the inverse variance weighted method. Results were visualized with the mr_scatter_plot() function from the TwoSampleMR package. Local plots were created using the locuszoomr (0.3.5) package, with 1000 Genomes EUR used for the LD reference. Plots were created using ggplot2 (v. 3.5.2) and ggpubr (v. 0.6.1) in R. Genomic coordinates of the rs450674 SNP were plotted in the UCSC Genome Browser including Jaspar predicted TF binding sites and overlapped with publicly available H3K27Ac tracks from different brain cell types.[63] The Zscan29 binding affinity to the major and minor allele was calculated with TFinder.[119]

For analysis of human microglia and BAMs in subjects with the rs450674 SNP, a microglia single nuclei rds. object was downloaded from synapse (syn53693904). To resolve microglia and BAMs, brain myeloid cells were re-clustered in Seurat (dims=1:15 and resolution=0.3) after exclusion of a small population of monocytes present in the original dataset. Genotype information was obtained from whole genome sequencing data and added to the Seurat metadata for genotype-stratified analyses. scATAC-seq data from Reid et al.[64] were visualized using the WashU Epigenome Browser.[120]

Statistics

Statistical analysis was conducted using the GraphPad Prism 10.4 software package. A two-tailed Mann-Whitney U test was used to determine statistical differences between two individual groups. When the effect of two independent variables was analyzed, a two-way analysis of variance (ANOVA) with Sidak's multiple comparisons test was used. Quantifications shown in bargraphs and scatterplots display the mean values ± standard error of the mean (SEM), as well as the values of each individual sample. Statistical significance was set as a P-value < 0.05 (exact P-values are shown). Information regarding mouse age, sample size (n), statistical tests, definitions of averages and error bars, and the number of independent experiments is provided in the figure legends.